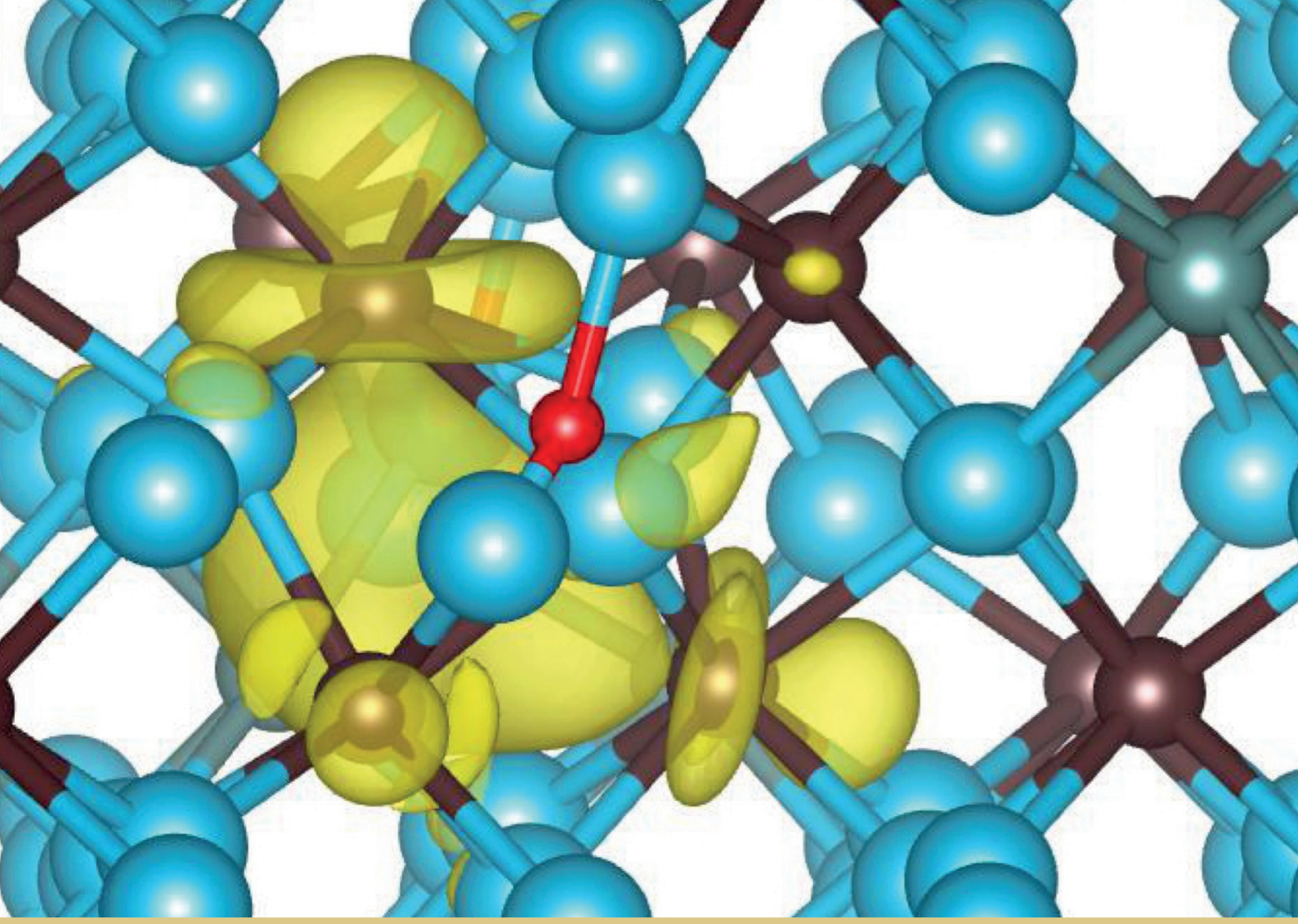

Ricardo Borda Lopes Vieira

HYDROGEN IN HIGH-K PERMITTIVITY OXIDES MODELLED BY THE MUON ANALOGUE

Tese de doutoramento em Física, no ramo de Física da Matéria Condensada orientada pelo Prof. Dr. Rui César do Espírito Santo Vilão e apresentada ao Departamento de Física da Faculdade de Ciências e Tecnologia da Universidade de Coimbra

Agosto de 2017

· U C ·

Universidade de Coimbra

UNIVERSIDADE DE COIMBRA

Hydrogen in high-κ permittivity oxides modelled by the muon analogue

Ricardo Borda Lopes Vieira

Supervisor: Prof. Dr. Rui César do Espirito Santo Vilão

Coimbra, 2017

This work was funded by the UE/FEDER, through *Programa Operacional Factores de Competitividade* - COMPETE and by National Funds through FCT - *Fundação ao para a Ciência e Tecnologia*, by Grant No. SFRH/BD/87343/2012.

"To Tânia

wife, counselor, companion, encourager"

Abstract

In this dissertation we present an investigation of the configurations of isolated hydrogen in oxides with high dielectric permittivity, using muonium as a light pseudo-isotope of hydrogen. The investigation of the muonium/hydrogen configurations in zirconium oxide (ZrO_2), also denominated zirconia, constitutes the core of this dissertation due to the fact that it is a prominent high-k candidates and its extremely interesting properties make it appealing for a wide-range of applications. We present our thorough investigation of the muonium/hydrogen configurations in ZrO_2, including the characterization of the neutral polaron donor state and of the neutral atom-like state, as well as the interplay between these two basic configurations. The neutral atom-like state is its also characterized yielding an isotropic hyperfine interaction in calcia-doped zirconia of $A_{iso} = 3.02(8)$ GHz, and an anisotropic hyperfine interaction in the nanograin yttria-doped zirconia of $A_{iso} = 2.1(1)$ GHz, $D = 0.13(2)$ GHz.

The characterization of the neutral configurations in ZrO_2 proved to be a demanding task because no direct signs of muonium are visible. Much was therefore learned from other oxides included in this investigation. In particular, the characterization of a polaron donor state in ZrO_2 benefitted immensely from the direct characterization of a similar state we found and characterized in rutile TiO_2. We therefore also introduce a study on TiO_2 where we show the polaron donor muonium state which is directly observed in this system. We also present an overview of selected similar oxides where we could observe the neutral atom-like state directly (for the first time in Lu_2O_3 and BeO), in support of our interpretation of the ZrO_2 data; these other systems were not investigated and modelled as thoroughly as ZrO_2 in this dissertation, and are bound to benefit from the modelling developed for ZrO_2. This is hinted at Chapter 5, where our conclusions are summarized and future perspectives are put forward.

Keywords: Hydrogen, High-κ permittivity oxides, Muonium, Muon Spectroscopy

Resumo

Nesta dissertação, apresentamos uma investigação das configurações de hidrogénio isolado em óxidos com permitividade dielétrica elevada, usando muonium como um pseudo-isótopo leve do hidrogénio. A investigação das configurações de muão / hidrogénio no óxido de zirconium (ZrO_2), também denominado zirconia, constitui o núcleo desta dissertação devido ao fato de ser um dos candidatos proeminentes de *high-*κ e às suas propriedades extremamente interessantes, que o tornam atrativo numa ampla gama de aplicações. Apresentamos uma minuciosa investigação das configurações de muão / hidrogénio em ZrO_2, incluindo a caracterização do estado neutro do dador de polar e do estado neutro do tipo *atom-like*, bem como a interação entre essas duas configurações básicas. O estado neutro do tipo *atom-like* é também caracterizado, produzindo uma interação hiperfina isotrópica de $A_{iso} = 3.02(8)$ GHz em ZrO_2 dopado com CaO, e uma interação hiperfina anisotrópica de $A_{iso} = 2.1(1)$ GHz, $D = 0.13(2)$ GHz em zirconia nanocristalina dopada com Y_2O_3. A caracterização das configurações neutras em ZrO_2 provou ser uma tarefa exigente porque nenhum sinal direto de muonium é visível. Muito, portanto, foi aprendido com outros óxidos incluídos nesta investigação. Em particular, a caracterização de um estado doador to tipo polarão em ZrO_2 beneficiou imensamente da caracterização direta de um estado similar que encontramos e caracterizamos em TiO_2 rutilo. Por isso, também apresentamos um estudo sobre TiO_2, onde mostramos o estado muonium do dador to tipo polarão que é observado diretamente neste sistema. Também apresentamos uma visão geral de uma selecção de óxidos similares, onde podemos observar diretamente o estado do átomo neutro, suportando a nossa interpretação dos dados de ZrO_2; esses outros sistemas não foram investigados e modelados tão exaustivamente como o ZrO_2 nesta dissertação, e beneficiarão dos modelos desenvolvidos para o ZrO_2. Este fato é dado a entender no Capítulo 5, onde as nossas conclusções são resumidas e apresentamos as perspectivas futuras.

Palavras Chave: Hidrogénio, Óxidos com permitividade dielétrica elevada, Muonio, Espectroscopia do muão positivo

Acknowledgements

It is a pleasure to thank the many people who made this thesis possible.

Foremost, I would like to express my sincere gratitude to my advisor Prof. Rui César do Espírito Santo Vilão for the continuous support of my doctoral study and research, for his patience, motivation, enthusiasm, and immense knowledge. His guidance helped me in all the time of research and writing of this thesis. I could not have imagined having a better advisor and mentor for my PhD study.

Besides my advisor, I would like to thank the rest of the CFisUC group with special emphasis to Prof. Dr. João Campos Gil, Prof. Dr. Helena Vieira Alberto, Prof. Dr José António Paixão and Prof. Paulo Gordo.

Thanks also go to Prof. Alois Weidinger, Dr. Apostolos Marinopoulos and Dr. James Lord, with whom I always had helpful discussions, and to the muon group from Texas Tech University that have also been wonderful collaborators.

The user support staff at ISIS, TRIUMF and PSI provided wonderful support and help with running experiments.

I appreciate the devotion given by my school teachers José Manuel and Teresa Duarte.

I thank my friends: Salomé, Jill, Estelina, Gafeira, Joana, Pedro Melo, Pedro, R. Martins, Susana, Tiago, Márcio and João Nuno for all the leisure and work time spent together.

To my wife Tânia I would like to say thank you for the patience and continuos love and devotion, much more then i deserved, in these stressful times of child caring while i was working on the thesis.

I would like to thank all my family especially my sons Gabriel and Josué, my brother, sister, brother in law, my parents Anibal, Bela, Lola and Paulo, and grandmothers Élia and Lídia for their patience and love.

And last of the of the utmost importance, I thank God for his continued presence. For having put all these people in my path, as well as many others not mentioned, and by the incessant support in the realization of this project.

Contents

List of Figures

List of Tables

Chapter 1

Introduction

1.1 Hydrogen in Oxides

Hydrogen is the most abundant chemical element in the Universe and one of the most abundant in the Earth's crust [1]. The abundance, size and presence in most of the precursor chemicals used for semiconductor growth makes hydrogen a likely impurity in any semiconductor. As an impurity, the presence of hydrogen can be a challenge in the construction of electronic devices where semiconductors are used. A number of different effects have been described and hydrogen is known to introduce levels in the band gap with the formation of different isolated atomic configurations, to form complex with other impurities and defects (both with defect passivation or activation). Formation of H_2 molecules and introduction of hydrogen-related extended defects is also known.

A particularly important example where the understanding of the effects of hydrogen impurities was essential for the development of an electronic device relates to the development of blue LEDs. Shuji Nakamura *et al.* showed that hydrogen was the source of passivation of Mg acceptors in p-type GaN. [2] This was an important breakthrough because GaN is mainly grown using metal organic chemical vapor deposition (MOCVD): in the growth process ammonia (NH_3) is used as the nitrogen source. Ammonia dissociates during growth and atomic hydrogen is introduced into the GaN crystal. In Mg doped GaN, the hydrogen atom forms a magnesium hydrogen complex (Mg-

H), thereby preventing Mg to act as an acceptor. [2] Thermal annealing of the GaN:Mg sample in a hydrogen-free (normally N_2) environment above approximately 400^oC permits hydrogen to diffuse out of the crystal, thereby breaking up the Mg-H complex. The formation of this complex was also confirmed by theoretical computations by Jörg Neugebauer and Chris Van de Walle where the calculations confirmed hydrogen passivation in Mg-doped GaN. [3]

High-κ dielectric oxides are currently under intense scrutiny in order to find adequate solutions for the insulator layer in the gates of MOSFET devices. Stabilized forms of zirconia (ZrO_2) are among the most prominent candidates [4]. Processing of these oxides, whereby hydrogen is often incorporated, is known to have a big impact in its electrical performance. Hydrogen is a strong candidate defect in order to explain the positive fixed charges in the ZrO_2 layer [5].

There are several techniques that are dedicated to the study of hydrogen such as impedance spectroscopy [6], infra-red spectroscopy [7], electron nuclear double resonance (ENDOR) [8], deep-level transient spectroscopy (DLTS) [9], quasielastic neutron scattering (QENS) [10], muon spin rotation spectroscopy (μSR) [11, 12, 13, 14]. Simulations of hydrogen defects in oxides are also made via DFT calculations [12, 15, 16, 17, 14, 18] and can be compared to the experimental results for better understanding of the hydrogen states.

Most of these techniques require a considerable concentration of hydrogen in the sample for there to be some hydrogen signal, so it is no surprise that to study hydrogen in some oxides hydrogen needs to be added during or after sample growth. This may cause structural diferences between samples with and without additional implanted hydrogen, causing the hydrogen defects to be different then those seen with the "natural" concentration of hydrogen.

However, when in high concentrations hydrogen is bound to interact with other impurities and defects, leading to the complex phenomena of passivation or activation of these other centers. A necessary first step towards the comprehension of the effect of hydrogen in the properties of materials is the characterization of the basic microscopic configurations of isolated hydrogen.

1.2 μSR Technique

The μSR technique does not need hydrogen implantation, it is based on a set of experimental techniques which use positive or negative muons as probes in condensed matter or gases.

μSR can as said above be done using positive or negative muons, however for all the studies presented in this work only positive muons (μ^+) and positive μSR techniques were used, which we will shortly refer to as muons and μSR, respectively.

In μSR studies, positive muons are viewed as light isotopes of hydrogen ion, and used as probes to study hydrogen effects. This is only possible because the proton and muon electronic properties are almost identical, as are also the muonium (electron bound to a muon) and hydrogen atom properties as confirmed in tables 1.1 [19] and 1.2 [19] below.

Table 1.1: *Muon and proton properties compared. The muon's mass is approximately 1/9 of the proton's mass m_p and its gyromagnetic ratio $\gamma_\mu = g_\mu \mu_\mu / h$ is larger than the proton's by approximately a factor of 3[19].*

	muon	**proton**
charge/e	+1	+1
spin/$\hbar$	1/2	1/2
mass/m_p	0.1126	1
Gyromagnetic ratio (MHz T^{-1})	135.54	42.58
Lifetime (μs)	2.19703	stable

1.2.1 Basic experimental setup

The μSR technique is based on the implantation of muons and posterior detection of the positrons resulting from the muon decay.

Table 1.2: *Muonium (Mu) and hydrogen (H) properties compared. The factor of 3 between the hyperfine parameter of ground state muonium and ground state protium basically arises from the corresponding relation between the nuclei magnetic moments, the electron density at the nucleus being basically the same: when scaling the hyperfine parameter of Mu by the nuclei magnetic moment relation we obtain 1402 MHz[19].*

	Mu	**H**
Reduced mass (m_e)	0.995187	0.999456
Binding energy in the ground state (eV)	13.54	13.60
Hyperfine parameter (MHz)	4463	1420.4
Atomic radius in the ground state (Å)	0.531736	0.529465

The muons are produced by high energy-protons (500MeV) that are directed to a carbon or beryllium target, where positive pions (π^+) are produced in the reaction:

$$p + p \rightarrow \pi^+ + p + n \tag{1.1}$$

The positive pions decay within 26ns to a positive muon and a muon neutrino (ν_μ).

$$\pi^+ \xrightarrow[26\,ns]{} \mu^+ + \nu_\mu \tag{1.2}$$

Since neutrinos always have their spins antiparallel to their linear momentum (negative helicity), the positive muons arising from pions decaying at rest in the target also have their spins antiparallel to their momentum. This allows to obtain a nearly 100% spin-polarized muon beam from pion decaying at the target.

Muons are radioactive particles, decaying *via* weak interaction with a mean life time of 2.2 μs, according to equation:

$$\mu^+ \xrightarrow[2.2\,\mu s]{} e^+ + \nu_e + \nu_\mu \tag{1.3}$$

where e^+ is the simble for the position particle and ν_e is the simble for the electron neutrino.

This decay is governed by the weak interaction and does not follow parity conservation. This shows up as an asymmetry in the positron emission direction. The probability dW for emission of a positron with energy in the interval $[E, E + dE]$, in the directions inside the cone with aperture angle between $[\theta, \theta + d\theta]$ (defined with respect to the direction of the muon's spin), is defined by the expression:

$$dW = \frac{G^2 m_\mu^5}{192\pi^3} (3 - 2\varepsilon) \varepsilon^2 [1 + A(\varepsilon) \cos\theta] \, d\varepsilon \, d\cos\theta \tag{1.4}$$

where $G/\sqrt{2} = 1.01 \times 10^{-5} m_p^{-2}$ expresses the Fermi coupling of the weak interaction (m_p is the proton's mass), $\varepsilon = E/E_{\max}$ is the energy of the positron normalized to the maximum energy and $A(\varepsilon)$ is a factor governing the asymmetry in the angular distribution of the decay positrons.

$$A(\varepsilon) = \frac{2\varepsilon - 1}{3 - 2\varepsilon} \tag{1.5}$$

The angular distribution of decay positrons is represented in Fig. 1.1 for some values of the asymmetry factor, as well as for the average asymmetry value, $\langle a \rangle$, for all energies $\left(\langle a \rangle = \frac{1}{3}\right)$.

These characteristics of the muon decay allow the monitoring of the muon spin direction, after implantation in a material, by measuring the time evolution of the asymmetry in the positron emission. Of course, a *sine qua non* condition for that is the presence of some degree of spin polarization of the ensemble of implanted muons (*i.e.*, a non-zero average component in some direction of the ensemble of muon spins).

In light of all these characteristics the spin-polarized muon is very useful as a condensed matter probe.

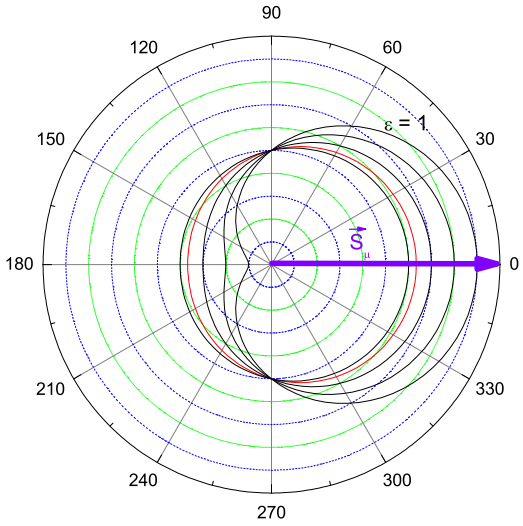

Figure 1.1: *Angular distribution of decay positrons with relation to the muon spin direction (at 0 degrees). We represent the cases of maximum positron energy, as well as the result of integration over all energies (red line).*

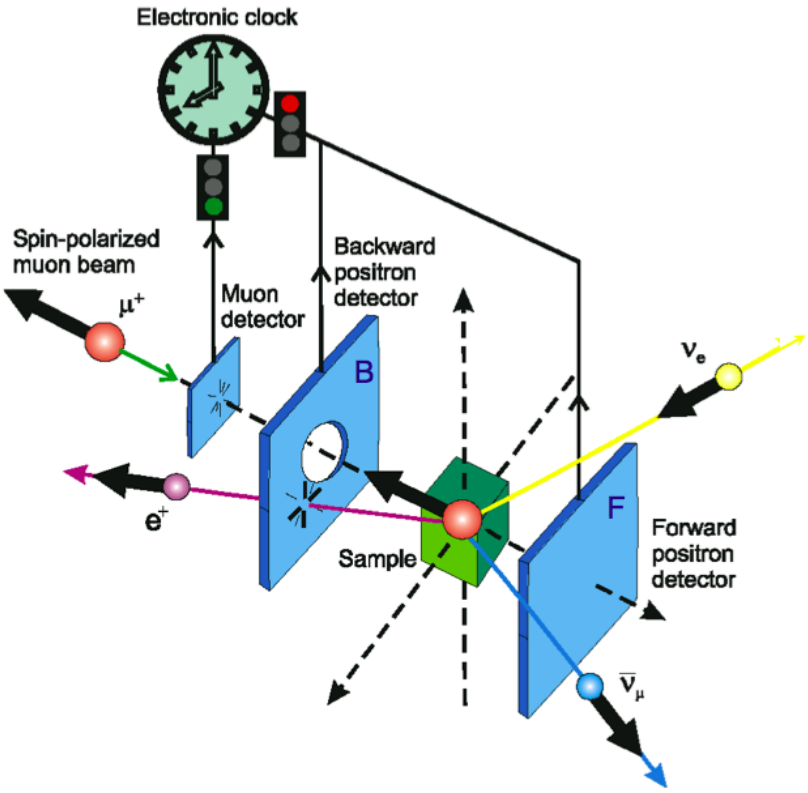

Figure 1.2: *Simple scheme on μSR experimental setup [20]*

In Fig. 1.2 we find the basic experimental setup for muon experiments. The spin-polarized muon beam is directed towards a sample of the material under scrutiny. A minimum of two positron detectors is adequately placed around the sample, usually in the forward (F) and backward (B) positions with respect to the incoming beam. The basic sample environment includes adequate instruments for temperature dependence studies (cryostats, furnaces). External magnetic fields may be applied to the sample region, as will be detailed in the following sections.

The number of counts N_D in detector D may be described by the expression:

$$N_D = B_D + N_0 \varepsilon_D \left[1 \pm A\, P_z\,(t)\right] \exp\left(-\frac{t}{\tau_\mu}\right) \tag{1.6}$$

where B_D is a factor describing the spurious (background) counts in the detector, which in principle are time-independent, N_0, multiplied by the number of detectors, corresponds to the number of real events at time zero, ε_D is the detection efficiency, relating not only to the detector intrinsic efficiency, but also to the geometrical disposition (for example, a detector placed farther away detects less positrons, thus decreasing ε, A is the intrinsic asymmetry of the detector arrangement. For detector B, the count rate is proportional to $(1 + A)$, in the case of fully polarized muons with polarization in the detector's symmetry axis; in the same circumstances, the count rate is proportional to $(1 - A)$ for detector F, $P_z\,(t)$ is the time evolution of the z component of the muon spin polarization (where the z axis is defined by the incoming beam direction) and τ_μ is the muon lifetime;

The main objective of these experiments is obtaining $P_z(t)$. This is usually done in two steps: by obtaining (i) the asymmetry $A\,P_z(t)$ in the experiment *proper* and (ii) the intrinsic detector asymmetry A in calibration measurements.

The intrinsic asymmetry A is in general less than the maximum theoretical value of 1/3 [21]. It is normaly determined by calibration measurements on a sample where the muon spin polarization is known. Silver is usually used for this purpose, because 100% of the muons implanted on this metal are known to form an easily identifiable non-relaxing diamagnetic fraction.

Low-transverse field (20 G) measurements on Ag are thus commonly used for these calibrations.

The experimental asymmetry is obtained through the difference between the number of counts in detectors F and B (after subtracting the background counts), normalized to the total number of counts (for more complex detector dispositions, simple generalizations apply):

$$A_{\text{exp}}(t) = \frac{[N_B(t) - B_B] - [N_F(t) - B_F]}{[N_B(t) - B_B] + [N_F(t) - B_F]} \tag{1.7}$$

However, due to different detector efficiencies, the expression 1.7 does not give us $A\,P_z(t)$ directly, but instead (after considering eq. 1.6):

$$A_{\text{exp}}(t) = \frac{(\alpha - 1) + (1 + \alpha)\,A\,P_z(t)}{(1 + \alpha) + (\alpha - 1)\,A\,P_z(t)} \tag{1.8}$$

where α is defined by:

$$\alpha = \frac{\varepsilon_B}{\varepsilon_F} \tag{1.9}$$

It is therefore necessary to correct the experimental asymmetry 1.7, which is usually done by computing:

$$A_{\text{corr}}(t) = \frac{N_B(t) - \alpha N_F(t)}{N_B(t) + \alpha N_F(t)} = A\,P_z(t) \tag{1.10}$$

The quantity α depends both on the intrinsic detection of the detectors and the geometrical details of the experimental setup, including positron absorption factors such as the sample thickness and the cryostat walls. α must therefore be determined for each case, usually together with the calibration measurements for the intrinsic (maximum) asymmetry A.

1.2.2 Muon spin rotation

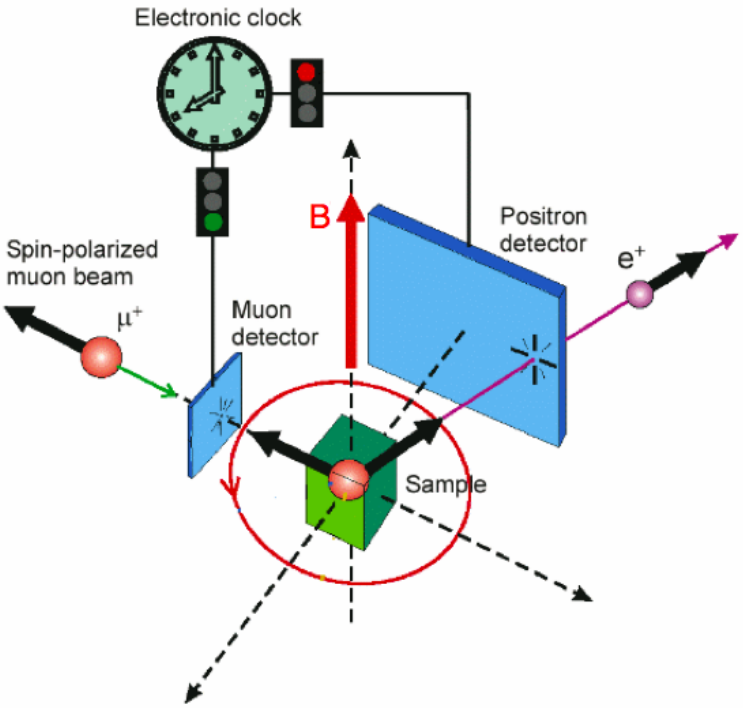

Figure 1.3: *Simple scheme of the muon spin rotation experimental setup [20]*

Figure 1.3 illustrates the simplest experimental geometry, which corresponds to the case where an external magnetic field B is applied perpendicularly to the initial muon spin polarization. With this configuration, and in the situation where the muon spin is subject only to the Zeeman interaction (the simplest situation) with the applied magnetic field, a simple precession of the spin occurs around B, with the Larmor frequency ν_L:

$$\nu_L = \gamma_\mu B \tag{1.11}$$

In this case, the polarization component in the initial direction z has a sinusoidal temporal evolution:

$$P_z(t) = P_{\max} \cos(2\pi\nu_L t + \phi) \tag{1.12}$$

where the phase ϕ depends on the definition of time zero $t = 0$, and is trivially associated with precession frequencies high enough (compared with the experimental resolution) for a non-negligible rotation of the polarization to occur between the initial cintilator and the sample. These trivial phase shifts present no temperature dependence and are simply proportional to the applied field. The existence of a temperature-dependent phase-shift is a clear sign of conversion between states, but those studies were not done in this work and so are beyond the scope of this thesis.

This subtechnique is based upon the characteristic precession frequencies of the muon spin in the presence of the hyperfine field, due to the hyperfine interaction between the muon spin and the electron spin. These precession frequencies of the muon present a distinctive behaviour with an applied magnetic field, as we move from the Zeeman *régime* where the hyperfine field dominates, to the Paschen-Back *régime* where the applied field is preponderant. Such studies, based upon the precession (or rotation) of the muon spin, are also designated muon spin rotation studies.

Despite the pure hyperfine frequency being observable in zero-field, the observation of the characteristic applied-field-dependence of the muonium precession frequencies requires that the applied field has a component perpendicular to the muon spin. Such spectroscopic studies are therefore best done in the transverse field geometry, where the external magnetic field is applied perpendicularly to the muon initial spin polarization

In Fig. 1.4 we show a particularly simple example, for calibration measurements on a silver sample. The individual time histograms for detectors F and B are shown, together with the corresponding asymmetry. The geometrical factor α can be extracted from these type of measurements as follows: the different detection efficiencies originating $\alpha \neq 1$ imply, in these TF measurements, that the experimental asymmetry oscilates with time around an average value different from zero. Fits to the time spectra are performed after correction of this offset by the fitting routine.

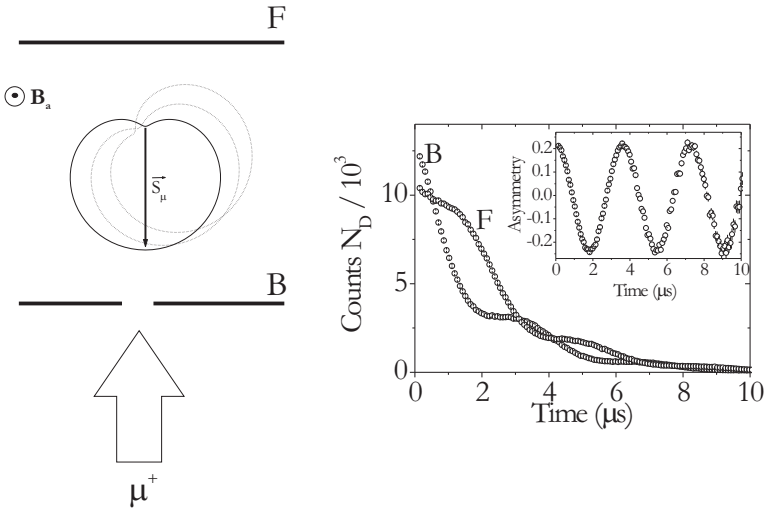

Figure 1.4: *The basic muon spin rotation experiment. In the left side we sketch the basic setup: spin-polarized positive muons are implanted into a sample, in a region subjected to a magnetic field B_a perpendicular to the initial muon spin, surrounded by two positron detectors in the forward (F) and backward (B) direction. The asymmetric probability for positron emission rotates with the muon spin and is drawn for three different times. The positrons are detected by detectors F and B, forming histograms like those shown in the right side. The corrected asymmetry $A_{\rm corr}(t) = (N_B - \alpha N_F)/(N_B + \alpha N_F)$ is shown as an inset.*

In muon spin rotation measurements, the presence of paramagnetic muonium is easily identified by its characteristics precession frequencies. A typical experimental test for the presence of paramagnetic muonium is done at low-field, where the characteristic $\nu_{12} = \nu_{23}$ precession (described in the next section) at 1.4×10^4 MHz/T is observed. An example is shown in figure 1.5.

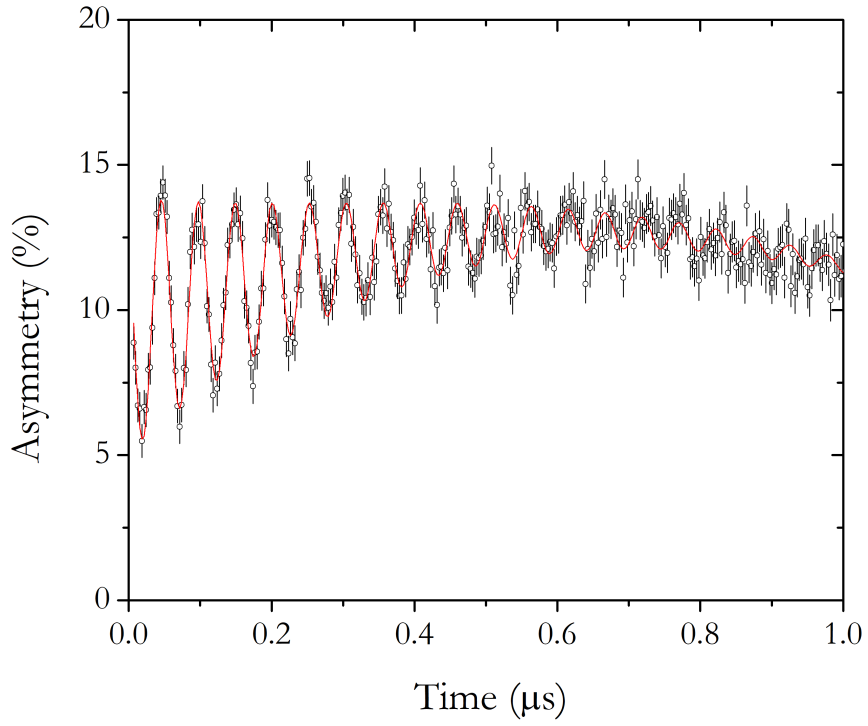

Figure 1.5: *Time spectrum of magnesium oxide at* $T = 280\ K$ *and transverse field* $B = 1.5\ mT$.

1.2.3 Muon spin relaxation

For relaxation studies longitudinal geometry is used (Fig. 1.2), by applying an external magnetic field parallel to initial polarization. In this case, the alterations to polarization arise from muon spin-flips in the presence of the magnetic field, by interactions with the lattice. As was discussed in section 1.2.6 such spin-flipping motivate a gradual loss of polarization, generally visible via a relaxation in asymmetry. The geometrical parameter α may eventually change with the magnitude of the applied field, in these measurements, due to the alteration of the positron trajectories, particularly for high-fields, where the charged particles trajectories may be significantly changed. In these cases, it may be necessary to perform a silver calibration in the entire field range.

As mentioned as well in section 1.2.6, and will be shown in the forthcoming chapters, such longitudinal field measurements also prove much useful for

the investigation of the strength of depolarizing mechanisms *via* quenching of the muon spin polarization.

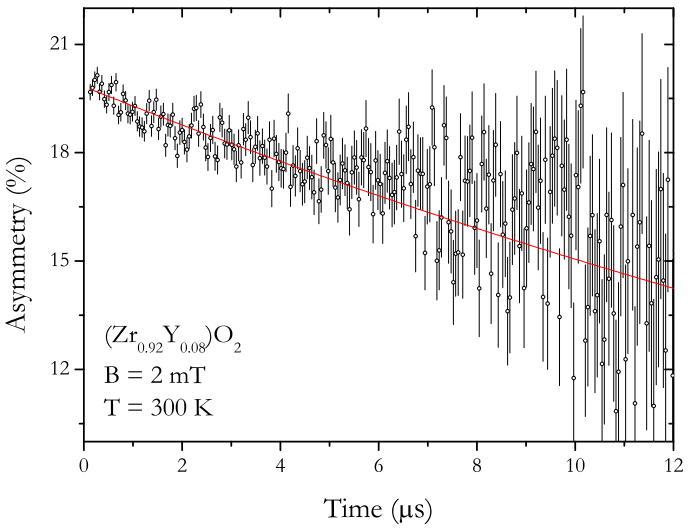

Figure 1.6: *Time spectrum of a yttria stabilized zirconia sample at* $T = 300\ K$*, subject to a longitudinal field of* $B = 20\ G$*.*

1.2.4 Muonium

When the muon enters the sample it interacts with its surroundings, especially with the spin of the electrons. If an electron bonds to the muon it creates a pseudo-atom that is commonly referred, as stated above, as muonium.

Intense research on the vacuum hyperfine structure of this exotic atom has been done in the past decades [22, 23, 24, 25, 26], serving as precise tests in quantum electrodynamics. However, when muonium is formed inside solids, its hyperfine structure is much affected by the local electronic structure, which makes it a rather sensitive probe.

In most cases two distinct configurations can be formed: isotropic muonium (also labelled normal), in the case where the electron wavefunction is still isotropic (i.e. spherically symmetric) and a bonded configuration (also labelled "anisotropic" or "anomalous" muonium) characterized by an axially

symmetric wave function.

Isotropic muonium

For $1s$ isotropic muonium, the relevant hyperfine hamiltonian (H_{HF} simply corresponds to the well-known Fermi contact interaction [27] between the muon spin $\mathbf{S}_\mu$ and the electron spin $\mathbf{S}_e$[19, 28]:

$$H_{HF} = hA\mathbf{S}_\mu \cdot \mathbf{S}_e \tag{1.13}$$

where A is the hyperfine interaction and h is the Plank constant.

Because μSR techniques are undertaken in the presence of an external applied magnetic field $\mathbf{B}$ the muon and electron Zeeman hamiltonian terms ($H_{\mu Z}$ and H_{eZ} respectively) should be added to the hamiltonian 1.13 yielding the systems hamiltonian to be:

$$H = H_{HF} + H_{\mu Z} and H_{eZ} \tag{1.14}$$

That can be written as:

$$H = hA\mathbf{S}_\mu \cdot \mathbf{S}_e - \mathcal{M}_\mu \cdot \mathbf{B} - \mathcal{M}_e \cdot \mathbf{B} \tag{1.15}$$

where the muon and electron magnetic moment operators $\mathcal{M}_\mu$ and $\mathcal{M}_e$ can be explicited in terms of the corresponding spin operators as:

$$\mathcal{M}_\mu = \frac{g_\mu \, \mu_\mu}{\hbar}\mathbf{S}_\mu \tag{1.16}$$

$$\mathcal{M}_e = -\frac{g_e \, \mu_B}{\hbar}\mathbf{S}_e \tag{1.17}$$

where the muon magneton μ_μ and the Bohr magneton μ_B are given, as usual, by:

$$\mu_\mu = \frac{e\hbar}{2m_\mu} \tag{1.18}$$

$$\mu_B = \frac{e\hbar}{2m_e} \tag{1.19}$$

where the hyperfine interaction A is simply proportional to the electron density at the muon $|\Psi_{1s}(r=0)|^2 = 1/\pi a_0^3$:

$$A = \frac{\mu_0}{4\pi}\frac{8}{3}\frac{g_\mu \mu_\mu g_e \mu_B}{a_0^3} = \frac{\mu_0}{4\pi}\frac{8\pi}{3} g_\mu \mu_\mu g_e \mu_B \, |\Psi_{1s}(r=0)|^2 \tag{1.20}$$

We assume that $\mathbf{B} = B\hat{\mathbf{k}}$, without loss of generality, leading us to:

$$H = hA\mathbf{S}_\mu \cdot \mathbf{S}_e - \frac{g_\mu \, \mu_\mu \, B}{\hbar}\hat{\mathbf{S}}_{\mu,z} + \frac{g_e \, \mu_B \, B}{\hbar}\hat{\mathbf{S}}_{e,z} = hA\mathbf{S}_\mu \cdot \mathbf{S}_e - \omega_\mu \hat{\mathbf{S}}_{\mu,z} + \omega_e \hat{\mathbf{S}}_{e,z} \tag{1.21}$$

where

$$\omega_e = 2\pi\gamma_e \, B \tag{1.22}$$

$$\omega_\mu = 2\pi\gamma_\mu \, B \tag{1.23}$$

and the muon and electron gyromagnetic ratios are, respectively,

$$\gamma_\mu = g_\mu \mu_\mu / h = 135.53 \, \mathrm{MHz/T} \tag{1.24}$$

$$\gamma_e = g_e \mu_B / h = 28024.21 \, \mathrm{MHz/T} \tag{1.25}$$

Hamiltonian 1.21 can be equivalently expressed as:

$$H = \frac{\hbar}{4}\omega_0 \sigma \cdot \tau - \frac{\hbar}{2}\omega_\mu \sigma_z + \frac{\hbar}{2}\omega_e \tau_z \tag{1.26}$$

where $\omega_0 = 2\pi A$, and σ and τ are the Pauli matrices.

If we assume an isotropic hyperfine interaction that is when the hyperfine interaction A is simply proportional to the electron density at the muon $|\Psi_{1s}(r=0)|^2 = 1/\pi a_0^3$:

$$A = \frac{\mu_0}{4\pi}\frac{8}{3}\frac{g_\mu \mu_\mu g_e \mu_B}{a_0^3} = \frac{\mu_0}{4\pi}\frac{8\pi}{3} g_\mu \mu_\mu g_e \mu_B \, |\Psi_{1s}(r=0)|^2 \tag{1.27}$$

this hamiltonian can be analytically solved (all the details are mentioned in [29, 19, 28], obaining the frequencies $\nu_{\mathrm{nm}} = (E_{\mathrm{n}} - E_{\mathrm{m}})/h$ that are summarized in Table 1.3. The $1-3$ and $2-4$ transitions correspond to forbidden transitions and are not observed [28].

Table 1.3: *Isotropic muonium precession amplitudes and frequencies.*

nm	$a_{\rm nm}$	$\nu_{\rm nm} = \lvert E_{\rm n} - E_{\rm m}\rvert / h$
12	$(\cos\zeta)^2/2$	$\left\lvert \frac{A}{2} + \frac{(\gamma_e-\gamma_\mu)\,B}{2} - \frac{(\gamma_e+\gamma_\mu)\sqrt{B^2+B_0^2}}{2} \right\rvert$
34	$(\cos\zeta)^2/2$	$\left\lvert \frac{A}{2} - \frac{(\gamma_e-\gamma_\mu)\,B}{2} + \frac{(\gamma_e+\gamma_\mu)\sqrt{B^2+B_0^2}}{2} \right\rvert$
14	$(\sin\zeta)^2/2$	$\left\lvert \frac{A}{2} + \frac{(\gamma_e-\gamma_\mu)\,B}{2} + \frac{(\gamma_e+\gamma_\mu)\sqrt{B^2+B_0^2}}{2} \right\rvert$
23	$(\sin\zeta)^2/2$	$\left\lvert -\frac{A}{2} + \frac{(\gamma_e-\gamma_\mu)\,B}{2} + \frac{(\gamma_e+\gamma_\mu)\sqrt{B^2+B_0^2}}{2} \right\rvert$

In Table 1.3 we defined B_0 ($B_0 = 0.1585$ T in vacuum) as:

$$B_0 = \frac{A}{\gamma_e + \gamma_\mu} \tag{1.28}$$

and the amplitudes of probability are:

$$\begin{aligned} \cos\zeta &= \left(\frac{1 + \frac{1}{2}\left(\frac{B_0}{B}\right)^2}{1 + \left(\frac{B_0}{B}\right)^2} \right)^{\frac{1}{2}} = \left(\frac{2x^2+1}{2(x^2+1)} \right)^{\frac{1}{2}} \\ \sin\zeta &= \left(\frac{\frac{1}{2}\left(\frac{B_0}{B}\right)^2}{1 + \left(\frac{B_0}{B}\right)^2} \right)^{\frac{1}{2}} = \left(\frac{1}{2(x^2+1)} \right)^{\frac{1}{2}} \end{aligned} \tag{1.29}$$

where x is the reduced field:

$$x = \frac{B}{B_0} \tag{1.30}$$

Again, much insight arises from inspection of the asymptotic limits[19]. In the low-field limit ($B << B_0$), one has

$$\nu_{12} \rightarrow \frac{(\gamma_e - \gamma_\mu)\, B}{2} \tag{1.31}$$
$$\nu_{14} \rightarrow A \tag{1.32}$$
$$\nu_{23} \rightarrow \frac{(\gamma_e - \gamma_\mu)\, B}{2} \tag{1.33}$$
$$\nu_{34} \rightarrow A \tag{1.34}$$

For usual vacuum-like values of the hyperfine interaction (the GHz range) ν_{14} and ν_{34} fall out of experimentally accessible range. Only the ν_{12} and ν_{23} of the muonium precession frequencies are therfore accessible experimentally: these frequencies coincide at low fields, and are here independent of the hyperfine interaction, simply corresponding to a gyromagnetic ratio of $1.4{\times}10^4$ MHz/T. Measurements at low fields are therefore most useful to identify the presence of muonium, but nothing can be extracted about the hyperfine interaction.

In the high-field limit, we have

$$\nu_{12} \rightarrow \gamma_\mu\, B - \frac{A}{2} \tag{1.35}$$
$$\nu_{14} \rightarrow \gamma_e\, B + \frac{A}{2} \tag{1.36}$$
$$\nu_{23} \rightarrow \gamma_e\, B - \frac{A}{2} \tag{1.37}$$
$$\nu_{34} \rightarrow \gamma_\mu\, B + \frac{A}{2} \tag{1.38}$$

In this case, the higher ν_{14} and ν_{23} frequencies are generally unobservable, and the lower ν_{12} and the ν_{34} frequencies are symmetrically placed around the diamagnetic line at $\gamma_\mu\, B$, the difference between them being a direct measurement of the hyperfine interaction A.

Figures 1.7, 1.8, and 1.9 illustrate the field-dependence of the energy levels, precession frequencies and precession amplitudes, respectively.

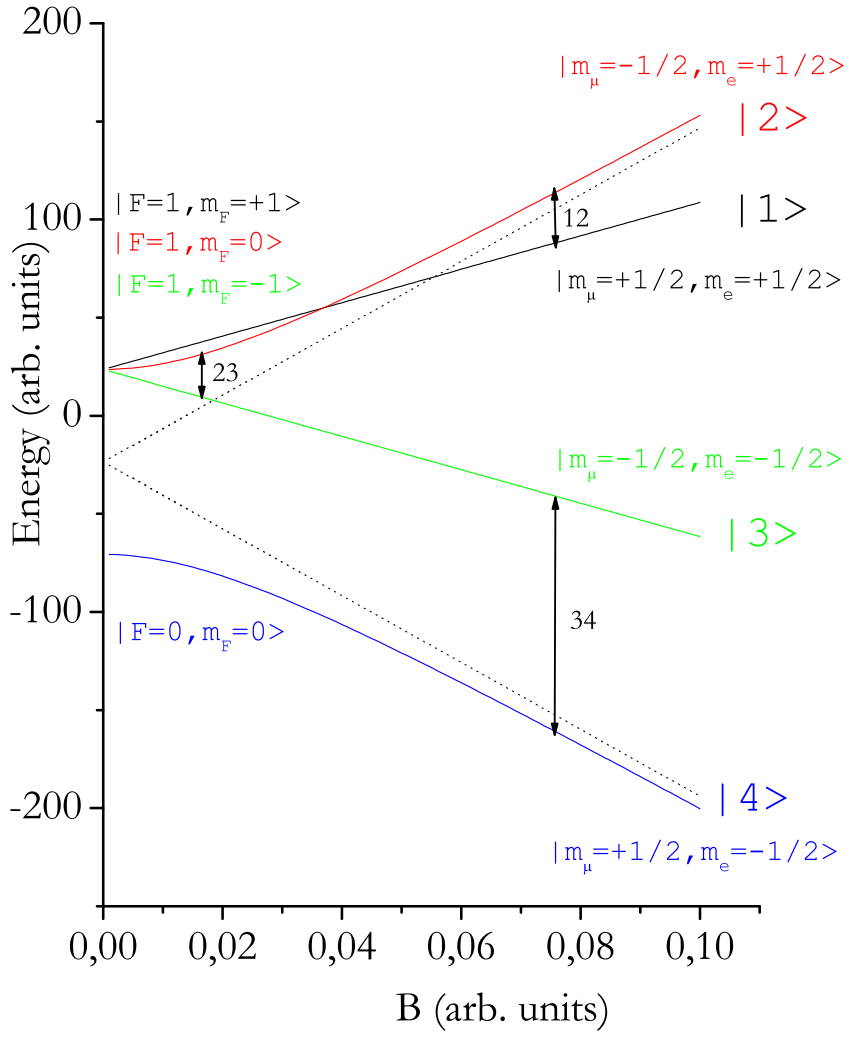

Figure 1.7: *Energy eigenvalues of the isotropic muonium hyperfine hamiltonian 1.15, as a function of the applied magnetic field B. This diagram is usually known as the Breit-Rabi diagram. A fictitious value of γ_e ($\gamma_e = 3\gamma_\mu$) was used, in order to display more clearly the essential features of this diagram. The asymptotes of the non-linear eigenenergies of the $|2\rangle$ and $|4\rangle$ eigenstates are drawn as well (dashed lines).*

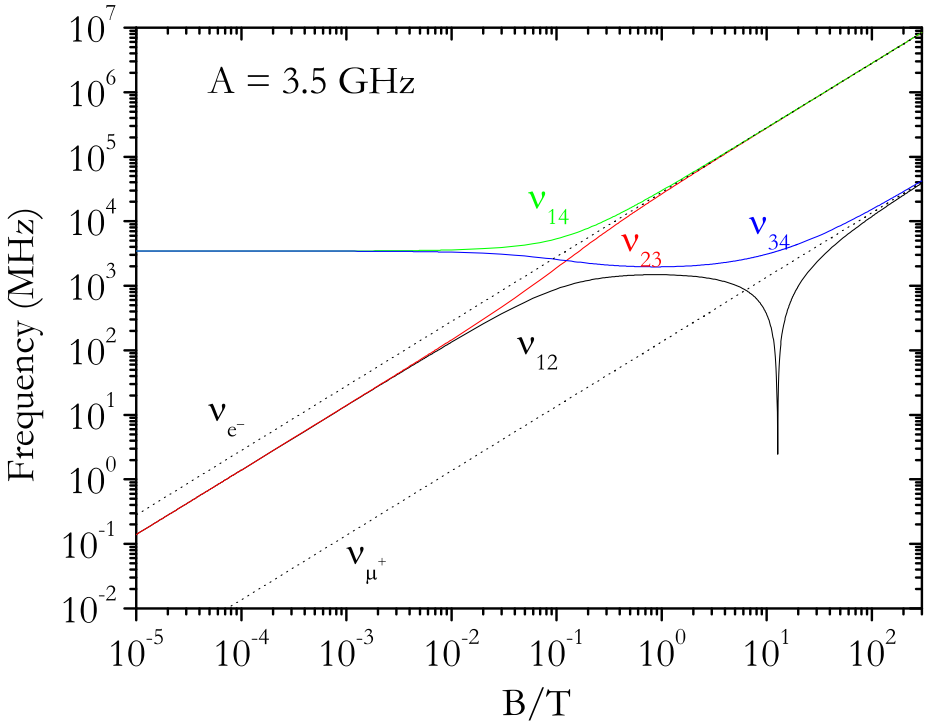

Figure 1.8: *Hyperfine transition frequencies for an isotropic muonium state with* $A = 3.5$ *GHz, as a function of the applied magnetic field* B*. The Larmor precession frequencies of the free muon and the free electron are drawn as dashed lines, clearly showing that for high fields the* ν_{14} *and the* ν_{23} *frequencies tend to* $\nu_e \pm A/2$ *and that the* ν_{12} *and the* ν_{34} *frequencies tend to* $\nu_\mu \pm A/2$*. The latter is preceded by the* $1-2$ *level crossing at 12.7 T.*

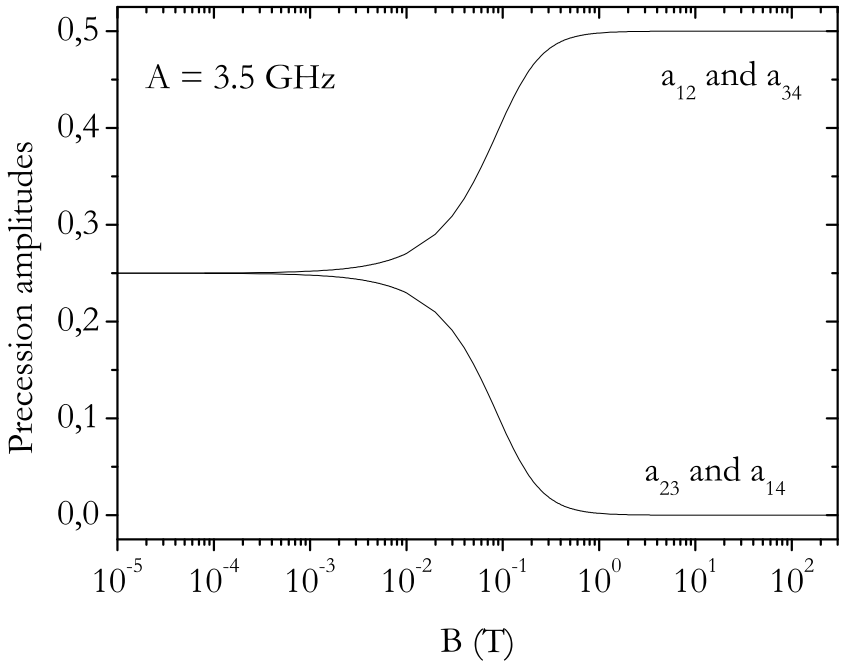

Figure 1.9: *Amplitude of the permitted hyperfine transitions for isotropic muonium with $A = 3.5$ GHz, as a function of the applied magnetic field B. The spectral weight is seen to be transferred at high fields from the $2-3$ and $1-4$ transitions to the $1-2$ and $3-4$ transitions.*

Anisotropic "anomalous" muonium

The above formalism may be easily extended to the case where the electronic wavefunction is not isotropic, or the g-factor itself is not isotropic.

In these cases the calculations are more complex and it is preferable to work in the reference frame where the electron g-tensor is diagonal. In this case the hyperfine tensor ($A(\theta,\phi)$) and the g-tensor ($g(\theta,\phi)$) can be written as:

$$A(\theta,\phi) = \frac{[\sum_{i=1}^{3}(\sum_{j=1}^{3} A_{ji} g_i h_i)^2]^{1/2}}{g(\theta,\phi)} \tag{1.39}$$

$$g(\theta,\phi) = [\sum_{i=1}^{3}(g_i h_i)^2]^{1/2} \tag{1.40}$$

where h_i are the direction cosines ($h_1 = cos(\phi)\cdot sin(\theta)$, $h_2 = sin(\phi)\cdot cos(\theta)$ and $h_3 = cos(\theta)$). The angles θ and ϕ are field orientation parameters in the g frame, where θ represents the angle between g_z and B_z and ϕ between g_x and B_z. A_{ij} is the orientation dependent value of the hyperfine coupling.

With these definitions of hyperfine tensor ($A(\theta, \phi)$) and the g-tensor ($g(\theta, \phi)$) we can obtain an expression for the frequency transitions ($\nu_\pm$) in the high field limit:

$$\nu_\pm = \left[\sum_{i=1}^{3} \left[\frac{m_s}{g\,(\theta, \phi)} \left(\sum_{j=1}^{3} g_j h_j A_{ij} \right) - h_i \nu_0 \right]^2 \right]^{\frac{1}{2}} \tag{1.41}$$

$$\nu_0 = g_\mu \beta_\mu B_0 / h \tag{1.42}$$

This means that using the μSR data we can obtain the hyperfine interaction tensor analysing the transition frequencies obtained by the muSR spectra.

1.2.5 Quenching of isotropic muonium polarization in a magnetic field

The existence of muonium dynamical processes pre– or post–thermalization may lead to significant depolarization of the muon spin. In such cases, it is usual to quench the muon polarization by application of an external magnetic field parallel to the initial muon spin. Such longitudinal field quenching experiments allow much insight into the strength of the depolarization mechanism. In these experiments, the polarization decay may be observed in the time spectrum as a polarization relaxation, thus providing access to the depolarization rates. Such longitudinal-field studies are therefore usually designated by muon-spin-relaxation studies.

The theoretical framework for isotropic muonium subject to no dynamical depolarization process is now presented, since it is the most fundamental front in these studies.

As seen before, in the process of muonium formation, the muon captures an electron, forming, in the spin sub-space $|m_\mu, m_e\rangle$, one of the initial states $|+,+\rangle$, $|+,-\rangle$, $|-,+\rangle$ or $|-,-\rangle$. In the absence of any applied field (i.e.,

in zero-field), the states $|+,+\rangle$ and $|-,-\rangle$ are eigenstates of the Breit-Rabi hamiltonian and therefore stationary, whereas the states $|-,+\rangle$ and $|+,-\rangle$ are superpositions of the $^1S_0$ and $^3S_1$, $m_F = 0$, $|2\rangle$ and $|4\rangle$ states. For typical values of A, these muonium atoms formed in the latter non stationary states will therefore oscillate with the hyperfine frequency between the $|2\rangle$ and $|4\rangle$ states and depolarize too quickly to be observed. Thus the observable polarization is only 50%. In the high-field Paschen-Back *régime*, the initial states will all correspond to eigenstates, and therefore the polarization will be preserved.

The characteristic variation of the polarization with an applied longitudinal field can therefore probe the formation of muonium. The correspondent time – and field – dependent polarization is found to be, for isotropic muonium [28]:

$$p(t) = a_{\parallel} + \frac{(\sin 2\zeta)^2}{2} \cos 2\pi\nu_{24} t \tag{1.43}$$

where

$$a_{\parallel} = (\cos 2\zeta)^2 + \frac{(\sin 2\zeta)^2}{2} \tag{1.44}$$

and the frequency ν_{24} is [28, 29],

$$\nu_{24} = (\gamma_\mu + \gamma_e)\sqrt{B^2 + B_0^2} \tag{1.45}$$

ν_{24} is in general too high to be experimentally visible and the corresponding parcel in equation 1.43 thus simply averages out to zero, yielding the polarization curve:

$$p = a_{\parallel} = \frac{1}{2} + \frac{x^2}{2\,(1+x^2)} \tag{1.46}$$

An example is shown in Fig.1.10 where $A = 3.5(1)$GHz is the fitted value of the hyperfine interaction we have a fraction of 40% of muonium present. For low fields, as discussed in the preceding section, half of the of that fraction, 20%, is lost, and at high fields the muonium states formed correspond to eigenvectores and are therefore stationary, the muon spin polarization being preserved. This curve is known as repolarization curve.

This method can constitute a very powerful tool to probe the formation of muonium, even in cases where muonium is subject to strong dynamical interactions that lead to the loss of muon spin polarization, thus preventing its direct spectroscopical identification. This loss in muon spin polarization is often designated "missing fraction".

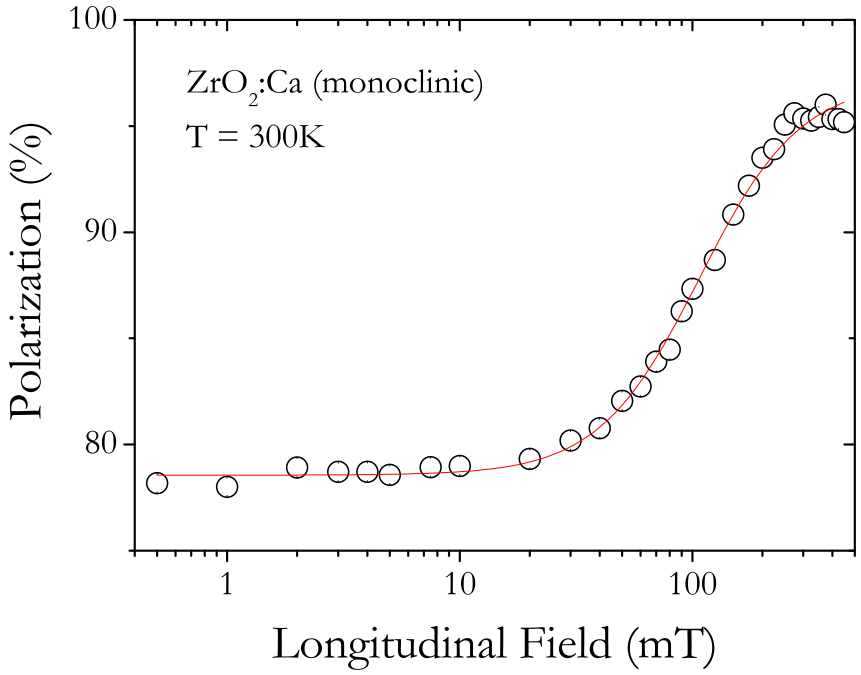

Figure 1.10: *Dependence of the muon spin polarization with the applied longitudinal magnetic field B, for calcia stabilized zircona at $T = 300\ K$ an isotropic muonium state with $A = 3.02(8)\,GHz$. The spin polarization is shown to vary from 78% at zero-field up to 96% at high-fields. This curve is therefore known as a repolarization curve. This curve will be discussed in Chapter 3.*

1.2.6 Muonium dynamics

When dynamical processes such as charge or spin–exchange exist, they can induce a depolarization of the muon spin. This simply arises due to the finite lifetime of the converting state, as can be seen from the following very simple argument. If a state 1 is converting to a state 2 with a rate $\lambda = 1/\tau$, where

τ is the lifetime of state 1:

$$Mu_1 \underset{\lambda}{\rightarrow} Mu_2 \tag{1.47}$$

then the polarization change dP_1 of state 1 in a time interval dt will be

$$dP_1 = -\lambda\, P_1\, dt \tag{1.48}$$

implying an exponential relaxation of the corresponding polarization

$$P_1(t) = P_1^0\, \exp(-\lambda\, t) \tag{1.49}$$

It is possible to have access to these conversion and/or inter-conversion processes if λ is inside the experimental frequency window, which appear *via* relaxation of the corresponding states' polarization. If λ is too high, then the entire polarization of the converting state is lost before it can be observed and a "missing fraction" in the polarization is detected. In such conversion cases, the precession frequency of the final state can nevertheless be observed and the existence of a prior conversion process can be inferred from the shifting of the precession phase.

The general form of the polarization of muonium subject to interconversion dynamical processes can then be written as a sum of exponentially relaxing phase-shifted precession frequencies [28]:

$$P(t) = \sum_{nm} a_{nm} \exp\left(-\lambda_{nm}\, t\right) \cos\left(2\pi\nu_{nm} t + \phi_{nm}\right) \tag{1.50}$$

Muonium dynamics has been the object of intensive theoretical treatment over the years [28]. We shall not discuss it extensively here since it does not constitute the essential objective of this work.

The investigation of its role in semiconductors and oxides has assumed increasing and vital importance since the discovery that this impurity can be the source of n-type conductivity in II-VI semiconducting compounds.[30, 31] This subject knew notable advances from the interplay of theoretical predictions from calculations based on density-functional theory (DFT) and muon-spin rotation (μSR) spectroscopy [16, 12, 32, 33]. From the experimental point of view, the use of muonium (the hydrogenic atom possessing

a positive muon as the nucleus: μ^+e^-) as a light pseudo-isotope of hydrogen has become standard in order to obtain information regarding the electronic states of hydrogen in materials.[34, 35]

1.3 Auxiliary techniques to μSR in this work

As mentioned above μSR is not the only technique to study hydrogen in oxide semiconductors and in most cases it is beneficial to use more then one technique to extrapolate a boarder picture of what hydrogen is really doing in the sample.

The present experimental study was complemented by *ab-initio* calculations based on density-function theory, done by Apostolos Marinopoulos [15, 17, 14] and Estelina da Silva [18], which will be used in order to strengthen the interpretation. We also compared our findings with those of the EPR-ENDOR technique made by Brant *et al.* [8]. For the sake of clarity only, we add a brief note on the fundamentals of DFT theory and EPR-ENDOR.

1.3.1 DFT

DFT is a many-body electronic structure calculation where the nuclei of the treated molecules or clusters are seen as fixed (Born-Oppenheimer approximation) [36], generating a static external potential V in which the electrons are moving. Then, a wavefunction satisfying the many-electron time-independent Schrödinger equation describes the stationary electronic state, were the hamiltonian can be written as:

$$H = \sum_{i=1}^{N} -\frac{1}{2}\nabla_i^2 + \sum_{i=1}^{N} v(\vec{r_i}) + \sum_{i<j}^{N} -\frac{1}{r_{ij}} = T + V_{pe} + V_{ee} \tag{1.51}$$

where T is the kinetic energy, V_{pe} is the potential energy from the external field due to positively charged nuclei, and V_{ee} is the electron-electron interaction energy.

In this theory the key variable is the particle density $n(\vec{r})$ which for a normalized wavefunction is given by:

$$n(\vec{r}) = N \int |\Psi(\vec{r_1}, ..., \vec{r_N})|^2 d\vec{r_2}, ..., d\vec{r_N} \tag{1.52}$$

From the Hohenberg-Kohn theorems we know that the energy is a density functional and can be solved by applying the Lagrangian method of undetermined multipliers.

A simple way to do that is to consider an energy functional, $E_s[n]$, that does not explicitly have an electron-electron interaction energy term:

$$E_s[n] = \langle \Psi_s[n] | T + V_s | \Psi_s[n] \rangle \tag{1.53}$$

where V_s is an external effective potential in which the particles are moving.

The second Hohenberg-Kohn theorem ensures that when the energy is written as a functional of some particular (positive) density, then its value is always larger than the ground state energy. This provides the necessary variational principle from which the Kohn-Sham equations are derived:

$$\frac{\delta E}{\delta n} = 0 \tag{1.54}$$

From this variational principle the effective Kohn-Sham potential can be derived:

$$V_s(\vec{r}) = V(\vec{r}) + \int \frac{e^2 n_s(\vec{r'})}{|\vec{r} - \vec{r'}|} d^3r' + V_{xc}[n_s(\vec{r})]. \tag{1.55}$$

The second term denotes the Hartree term describing the electron-electron Coulomb repulsion, while the last term is called the exchange-correlation potential, which includes all the many-particle interactions. The problem of solving the Kohn-Sham equation is then done in a self-consistent (i.e., iterative) way. Usually one starts with an initial guess for $n(\vec{r})$, then calculates the corresponding V_s and solves the Kohn-Sham equations. Then one calculates a new density and starts again. This procedure is then repeated until convergence is reached.

In order to make connection with the muSR data and analysis and also to quantify these findings through a measurable quantity the formation energies and the isotropic (Fermi-contact) and dipolar parts of the hyperfine tensor of the H^0 states were calculated.

Formation energies

In oxide semiconductors such as zinc oxide, tellurium oxide and yttrium oxide, where intensive research on isolated hydrogen has been done, two distinct configuration states have been identified: H^-at an interstitial position and, H^+ at a bonded position, together with the respective neutrals [37, 33, 11]. The use of positive muons to study these configurations has been very successful, in contrast with the difficulties found by techniques sensitive to protons themselves, due to the reactivity of hydrogen in oxide semiconductors.

The theoretical modelling of such states usually computes the formation energy ($E_{\text{form}}(H^q)$) of the various charged states (q) as a function of the electronic chemical potencial (Fermi level E_F). The expression for $E_{\text{form}}(H^q)$ is:

$$E_{\text{form}}(H^q) = E_{ctot}(H^q) - E_{\text{tot}}(\text{bulk}) - \mu_H + q(E_F + E_{\text{V}}) \tag{1.56}$$

where $E_{\text{tot}}(H^q)$ is the total energy of the supercell with hydrogen in the charge state q ($q = -1, 0$ or $+1$) and $E_{\text{tot}}(\text{bulk})$ the total energy of the bulk-crystal supercell. μ_H is the chemical potential of hydrogen and was taken here as half the energy of a hydrogen molecule at $T = 0$ K. E_{V} is the energy of the valence-band (VB) edge of the bulk the supercell and provides the reference energy for the values of E_F in the gap. This is illustrated in Fig. 1.11, where two basic possabilities are illustrated.

In this context it is practical to discuss about Anderson's U model [38]. U is a quantity defined by U = $\epsilon(0/-) + \epsilon(+/0)$, were ϵ(a/b) is the energy of the a/b level. In this scheme we can predict two possible outcomes: positive-U and negative-U. Positive-U corresponds to the expected relative position of the two levels, taking in to account that the energy to ionize a single occupied state is larger then the energy to ionize a doubly occupied state. By opposition negative-U implies that the energy to ionize a doubly occupied state is larger then the energy to ionize a single occupied state. This can happen only if the energy associated to the site change compensates the coulombic repulsion of the two electrons.

Using this model, simply by knowing the nature of U, we can determine if H^0 is thermodynamically stable. In Fig.1.11 [11] we see that in negative-U

(a) H^0 is unstable and in positive-U (b) H^0 is sable.

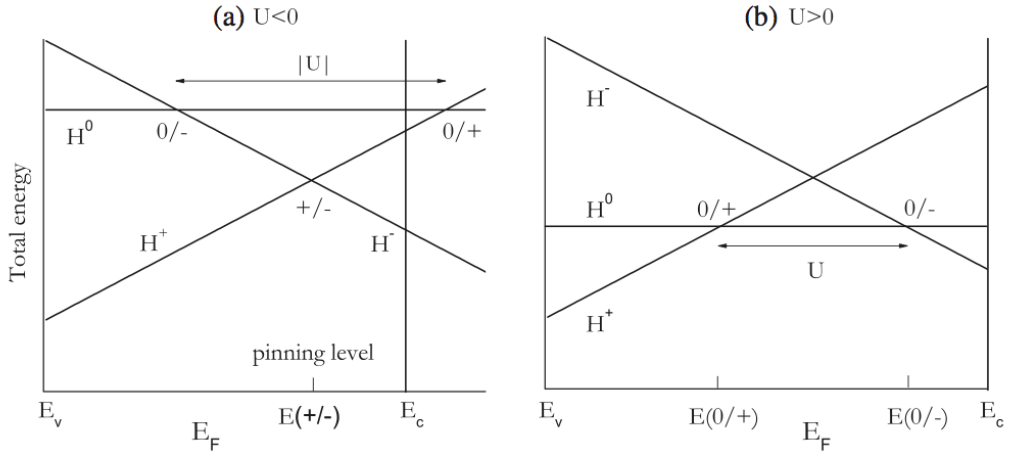

Figure 1.11: *Formation energies of a hydrogen defect centre as a function of Fermi level EF. The gradient with respect to EF is equal to the charge; Ev is the top of the valence band and Ec the bottom of the conduction band. (a) is drawn for negative U, and with the 0/+ donor level resonant with the conduction band. This leads to auto-ionization of the neutral state (shallow-donor behaviour) but the material will only be conductive under equilibrium conditions if the +/– pinning level is also band-resonant; here it is shown deep in the gap. (b) is drawn for positive U , leading to the opposite ordering of 0/+ and 0/– transition points, both shown deep in the gap[11].*

Hyperfine parameters

The Fermi-contact interaction,[39] A_{iso}, describes the interaction of the unpaired electron with the magnetic moments of the nuclei and can, therefore, provide a detailed insight on its localization character. The specific value of A_{iso} depends upon the magnitude of the spin density ρ_s ($\rho_s = \rho_\uparrow$ - $\rho_\downarrow$) at the site **R** of the nucleus as:[39]

$$A_{\text{iso}} = \frac{2\mu_0}{3} g_e \mu_e g_H \mu_H \rho_s(\mathbf{R}) \tag{1.57}$$

where μ_0 is the magnetic permeability of free space, g_e is the electronic g-factor, μ_e the Bohr magneton, g_H the nuclear gyromagnetic ratio for hy-

drogen and μ_H the nuclear magneton. The dipolar hyperfine constant D parameter is defined as:

$$D = \frac{\mu_0}{4\pi} g_e g_H \int_0^{\pi} \int_0^{\infty} \sin^2\theta \cos\theta \frac{1}{r} \frac{\partial \left(|\psi(r,\theta)|^2\right)}{\partial\theta} d\theta dr \tag{1.58}$$

where ψ is the electronic wavefunction and θ is the polar angle with the respect to the symmetry axis.

The A_{iso} and D values where determined for four different oxygen-bound H^0 configurations using the PBE functional and for one (the one possessing the lowest-formation energy) using the hybrid HSE06 functional.

The hyperfine coupling represents an interaction between the electron spin density $\sigma(\mathbf{r})$ with spin S, and nuclei J with nuclear spin I:

$$H = \sum_{i,j=1}^{3} S_i A_{ij} I_j$$

where i and j are the tensor components.

The hyperfine tensor, A_{ij} can be written as the sum of two interactions, a contact interaction (isotropic) and a classical interaction (anisotropic): [40]

$$A_{ij} = \frac{1}{2S} \gamma_J \gamma_e \hbar^2 \left[(A_{\text{iso}})_{ij} + (A_{\text{ani}})_{ij} \right]$$

γ_J is the nuclear Bohr magneton of nucleus J and γ_e the electron Bohr magneton.
The contact term, known as the Fermi-contact is defined as

$$(A_{\text{iso}})_{ij} = \frac{8\pi}{3} \delta_{ij} \int \delta(\mathbf{r} - \mathbf{R}) \sigma(\mathbf{r}) d\mathbf{r}$$

which is proportional to the magnitude of the electron spin density ($\sigma(\mathbf{r})$) at the position of the nucleus ($\mathbf{r}$-$\mathbf{R}$). δ_{ij} represents the usual Kronecker delta (unit matrix).

The classical dipole-dipole contribution is:

$$(A_{\text{ani}})_{ij} = \int \left[\frac{3(\mathbf{r} - \mathbf{R})_i (\mathbf{r} - \mathbf{R})_j}{|\mathbf{r} - \mathbf{R}|^5} - \frac{\delta_{ij}}{|\mathbf{r} - \mathbf{R}|^3} \right] \sigma(\mathbf{r}) d\mathbf{r}$$

As said above in DFT the electron spin density at the position of the nucleus is calculated so the hyperfine interaction can be then simply obtained using equations 1.59 and 1.59. A more complete overview regarding the numerical implementation can be found in Refs. [41, 42, 40].

1.3.2 EPR-ENDOR

ENDOR (Electron-Nuclear Double Resonance) is the detection of nuclear magnetic resonances (NMR) by observing their effect on an electron paramagnetic resonance (EPR) signal. In the specific case that we will compare with our data in chapter 2 the nuclear magnetic resonances detected are those relative to the hydrogen nuclei present in the sample. The NMR transitions are affected by application of a radiofrequency, as with NMR. In solid state nuclear magnetic resonance spectroscopy the selection of signals is determined by the radiofrequency being resonant with the Larmor frequency of a particular nucleus (hydrogen in our case). In ENDOR, one records a spectrum that exhibits resonances from all magnetically active nuclei (nuclear spins) that are coupled to the paramagnetic center (electron spin(s)) by the hyperfine interaction. The position of these resonances can vary immensely, depending on the nature of their interaction with the paramagnetic center. A given scan may exhibit ENDOR signals due only to the hydrogen nuclei coupled to the center, as these may appear at radiofrequencies well separated from other coupled nuclei, and experimental parameters may favor hydrogen NMR transitions as opposed to those of other nuclei. The theoretical principles behind the ENDOR technique are the same as those in sections 1.2.4 and 1.2.4 were the parameters relative to muons (such as the muon magneton) are changed to the hydrogen equivalents.

1.4 Outline of the thesis

This dissertation is devoted to the investigation of the configurations of isolated hydrogen in oxides with high dielectric permittivity, using muonium as a light pseudo-isotope of hydrogen. As mentioned in section 1.1, zirconium oxide is among the most prominent high-k candidates; additionally,

its extremely interesting properties make it appealing for a wide-range of applications. The investigation of the muonium/hydrogen configurations in ZrO_2 therefore constitutes the core of this dissertation. Both monoclinic ZrO_2 and cubic ZrO_2 (stabilized with Y_2O_3) had been briefly investigated before using μSR in the seminal work of Cox et al. in oxides [11]. A diamagnetic component had been identified, but little was known about the neutral paramagnetic configurations.

The characterization of the neutral configurations in ZrO_2 proved to be a demanding task because no direct signs of muonium are visible. Much was therefore learned from other oxides included in this investigation. In particular, the characterization of a polaron donor state in ZrO_2 benefitted immensely from the direct characterization of a similar state we found and characterized in rutile TiO_2. We therefore begin by presenting the TiO_2 data in Chapter 2 and the polaron donor muonium state which is directly observed in this system. We then present our thorough investigation of the muonium/hydrogen configurations in ZrO_2, in Chapter 3, including the characterization of the neutral polaron donor state and of the neutral atom-like state, as well as the interplay between these two basic configurations. The neutral atom-like state is also not visible directly in ZrO_2, but its characterization is not so challenging due to its more traditional behaviour. In Chapter 4 we nevertheless present an overview of selected similar oxides where we could observe this state directly (for the first time in Lu_2O_3 and BeO), in support of our interpretation of the ZrO_2 data; these other systems were not investigated and modelled as thoroughly as ZrO_2 in this dissertation, and are bound to benefit from the modelling developed in Chapter 3. This is hinted at Chapter 5, where our conclusions are summarized and future perspectives are put forward.

Chapter 2

Titanium oxide

2.1 Motivation

In this work the investigation of the hydogen/muon states in TiO_2 proceeded as a research line colateral to the corresponding work on ZrO_2. This proved however essencial to clarify the nature of the donor configuration, since this could be characterized in a direct way by pure spectroscopic methods, as well as compared with proton configuration measured by EPR/ENDOR.

The investigation of hydrogen defects in titanium dioxide (TiO_2) is a hot topic *per se*, due to the technological importance of this material. In fact,titanium dioxide is a most versatile material which is used in a wide range of applications, including heterogeneous catalysis and photocatalysis, gas sensing, hydrogen storage and electrochromic devices [43, 44]. TiO_2 is also currently being considered as an adequate candidate for the replacement of SiO_2 as gate oxide material in highly miniaturized transistors [45].

The hydrogen impurity is known for long to play a relevant role in the properties of rutile titanium dioxide. The increase of conductivity due to hydrogen has been established in the 1960′s [46, 47]. However, only recently a renewed interest has been devoted to the defect physics of hydrogen in rutile TiO_2: the effects of hydrogen on the conductivity of TiO_2 have been thoroughly investigated by macroscopic techniques [48] and hydrogen diffusion in rutile has been found to be enhanced by 9 orders of magnitude when stimulated by resonant infrared light [49]. The nature of the hydrogen donor

in TiO_2 is the matter of ongoing debate: in DFT-GGA calculations, shallow donor behaviour has been pointed out for the positive configuration, found at an oxygen bonded position [50]; in DFT-LSD+U calculations, a deep donor was suggested instead [51]. The interpretation of capacitance measurements has raised the possibility that the ionized donor does not form a O-H bond [52].

In 2011 Brant et al. [8] hydrogen defect was also studied by means of the EPR proton-ENDOR techniques. These authores found that the electron is mainly centered at the Ti atom reducing it from Ti^{4+} to Ti^{3+}. Hydrogen is bound to one of the six oxygen atoms surrounding Ti and the magnetic interaction between the proton and the electron is mainly dipolar. This gives a very specific hyperfine interaction and therefore permits a very sensitive comparison with μSR.

As described in chapter 1 muonium, a positive muon and an electron, is often used as a substitute of hydrogen in materials research. In particular in semiconductors and insulators, a large amount of information on the hydrogen behavior is deduced from this analogy. It is usually assumed that the information gained from μSR can be transferred with appropriate modifications to hydrogen. However, a proof of this assumption is seldom provided, mainly due to the lack of overlapping experiments. A particularly-interesting case is the intensively-studied field of the hydrogen doping character in a class of II-VI, III-V and oxide semiconductors [53, 54, 15, 55]. Here practically all calculations refer to hydrogen (more precisely, only the charge, not the possible motion of the positive center is considered) whereas most experimental information comes from muon measurements [11, 12, 16, 34, 56]. Overlapping data exist only for ZnO where proton-ENDOR data (Hoffmann)[57] can be compared directly with μSR results [33, 31]. A number of properties (e.g. ionization energy) are indeed similar for the two species. However, the measured hyperfine interaction, scaled with the magnetic moments, differs by almost a factor of ten for ZnO. This raised the question whether indeed the same configuration is measured in the two cases [58, 59]. A possibility is that the hydrogen center is slightly more complex then the muon, involving an additional impurity or defect [58, 59]. As stated before the findings of Brant et al. [8] by the EPR and ENDOR method in TiO_2, makes this material a

prime candidate for study case of this muonium/hydrogen transferability.

Titanium dioxide had, before this study, been object of μSR studies in the context of a research program centered in the effects of hydrogen in candidate high-k dielectrics [11]. There it was proposed as a candidate shallow donor state, ionizing around 10 K with a 8(4) meV ionization energy. However, this was based on the temperature dependence of the relaxation of the diamagnetic signal only, and it was not possible to observe the characteristic beats of the shallow like muonium lines in the time spectra and thus characterize the hyperfine interaction of this state. The observation of the shallow-donor like muonium lines is highly dependent on the concentration of impurities/defects in the sample and the characterization of the hyperfine parameters of the shallow-muonium like state in TiO_2 implies adequate samples with a reduced content of defects/impurities.

2.2 Experimental Detais

2.2.1 Ancillary measurements and sample preparation

In this work we only investigated the rutile phase of TiO_2 as shown in Fig. 2.1. This phase of TiO_2 is characterised by the symmetry group 136: P 42/mmm that implies that Ti has a symmetry 2a (mmm) in positions $(0,0,0)$ and $(\frac{1}{2},\frac{1}{2},\frac{1}{2})$ and O has a 4f (m2m) symmetry in positions $(x,x,0)$, $(-x,-x,0)$, $(-x+\frac{1}{2},x+\frac{1}{2},\frac{1}{2})$ and $(x+\frac{1}{2},-x+\frac{1}{2},\frac{1}{2})$, where $x = 0.3047$, $a = b = 4.5925(6)$ Å and $c = 2.9578(4)$ Å

For these studies a high purity single crystal of TiO_2 was acquired commercially (from Alfa Aesar). This crystal was characterised and oriented for the μSR measurements by means of X-ray diffraction, which confirmed that the sample was cut on a [110] plane. A high purity crystal is of course not sufficient to guarantee the observation of muonium like lines, so an Express proposal was submitted to the ISIS Facility in order to do a quick measurement at the base temperature of the Closed Cycle Refrigerator cryostat (T= 6 K), for a transverse field of B= 100 G. This was performed at the EMU instrument and, as seen in Fig. 2.2, apparent signs of satellite lines are visible however with possible existence of some kind of dynamics already

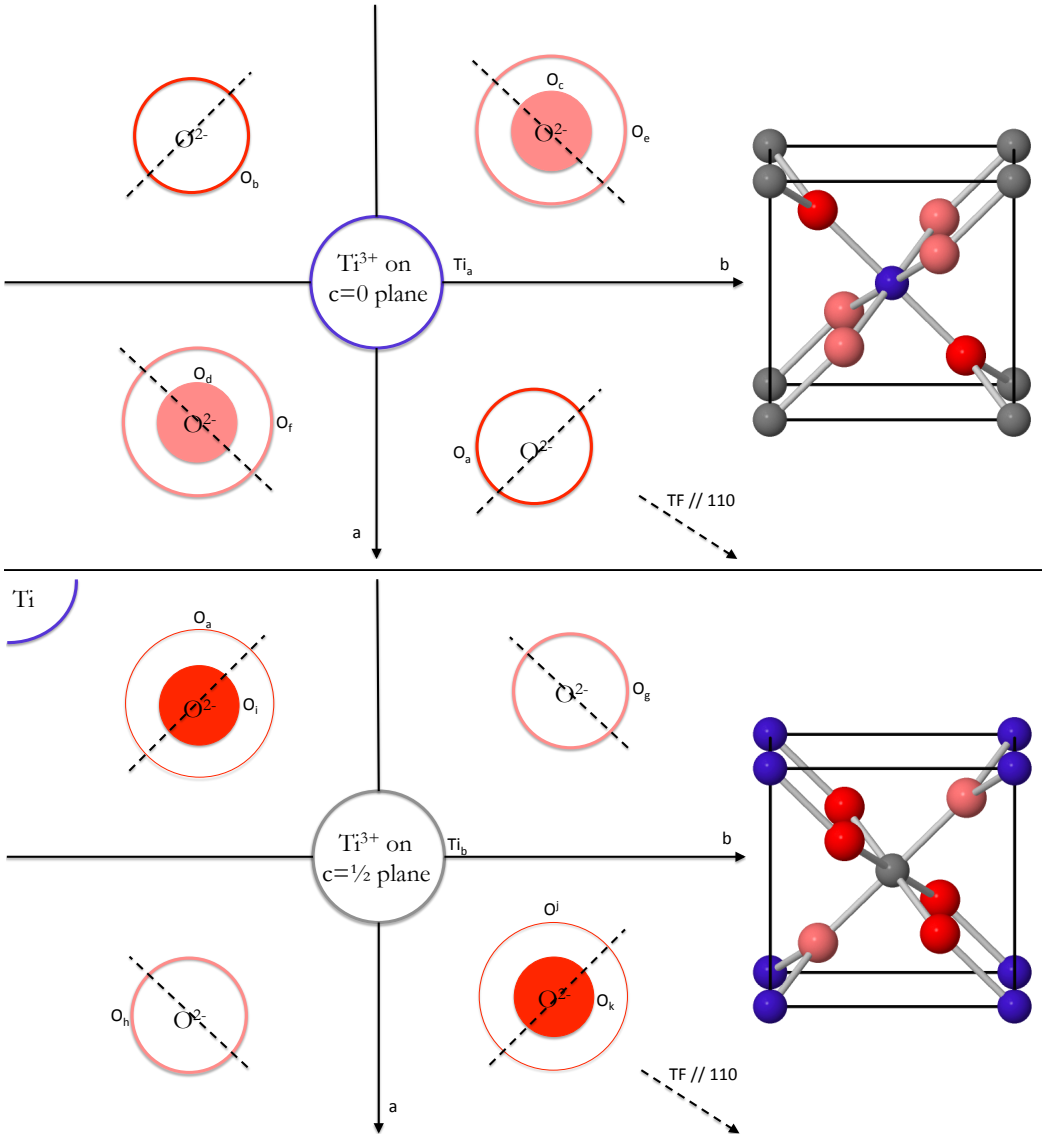

Figure 2.1: *Two dimensional sketch of the two magnetically inequivalent sublattices under a magnetic field parallel to the 110 direction. Red oxygens are in the same plane as the violet titanium atoms. Pink oxygens are in the same plane as grey titanium atoms but in a different plane to red oxygens and violet titanium atoms as shown in the three dimensional representation on the right. Dashed lines represent the orientation of the possible O-H bonds.*

present at this temperature.

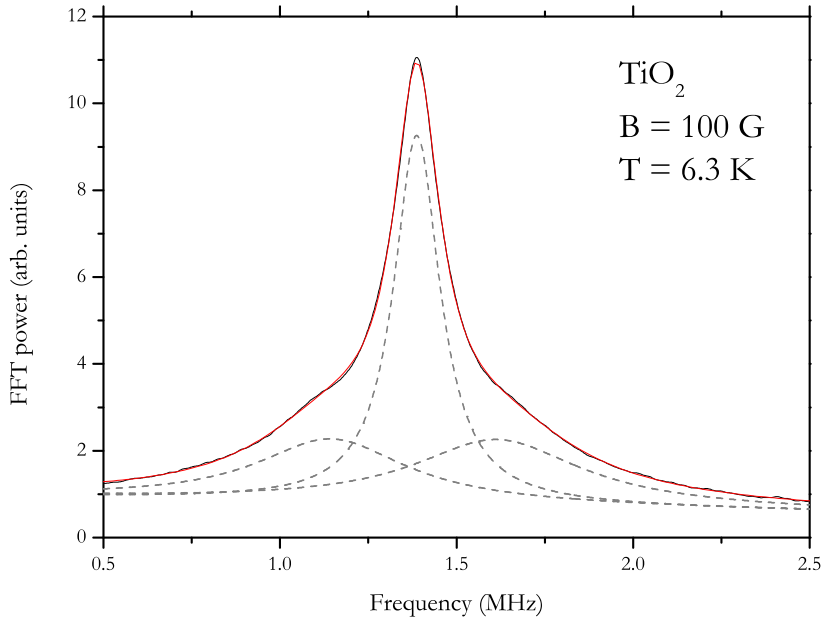

Figure 2.2: *Fourier transform of the data acquired from the Muon Express service at T= 6 K, B= 100 G*

To pursue the study of these lines a conventional proposal was therefore submitted, having into account that because of the possible existence of dynamics at 6 K and the estimated value of the hyperfine interaction, measurements at lower temperatures should be made. Muon spin spectroscopy measurements were undertaken at the MUSR instrument of the ISIS Facility (United Kingdom) using the Variox cryostat. To eliminate the signal of muons stopping in the sample holder, due to the size of the sample relative to the beam width, the sample was mounted on top of a Fe_2O_3 background as shown in Fig. 2.3. Fe_2O_3 was fixed to the sample holder by yellow adhesive tape. A silver sample was mounted in the same setup and geometry used for calibrating the maximum asymmetry and for optimising the sample position.

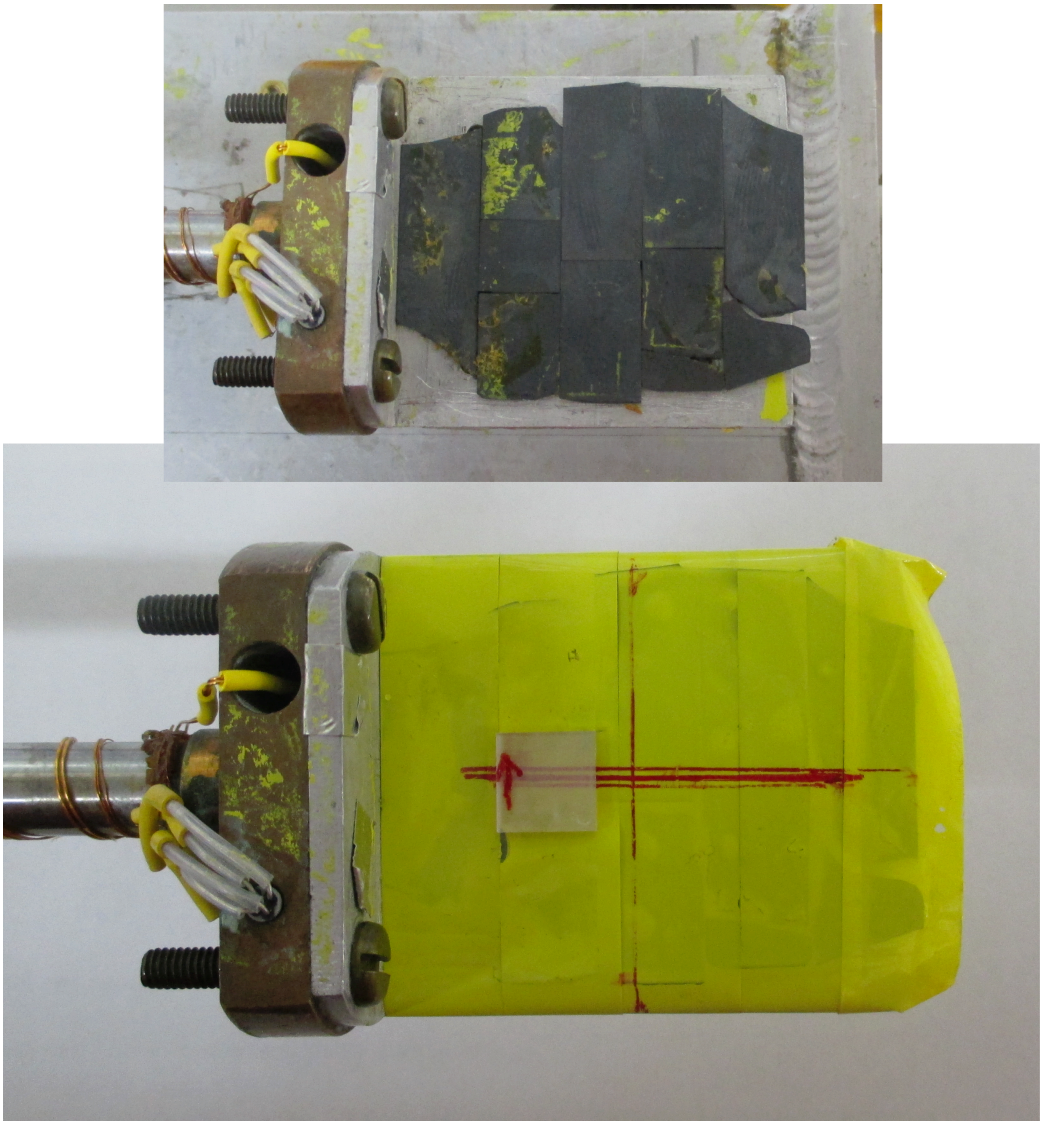

Figure 2.3: *Experimental setup. Top sample holder with Fe_2O_3. Sample holder with TiO_2 sample and Fe_2O_3 background (vector drawn in sample indicates the c-axis or (110) orientation).*

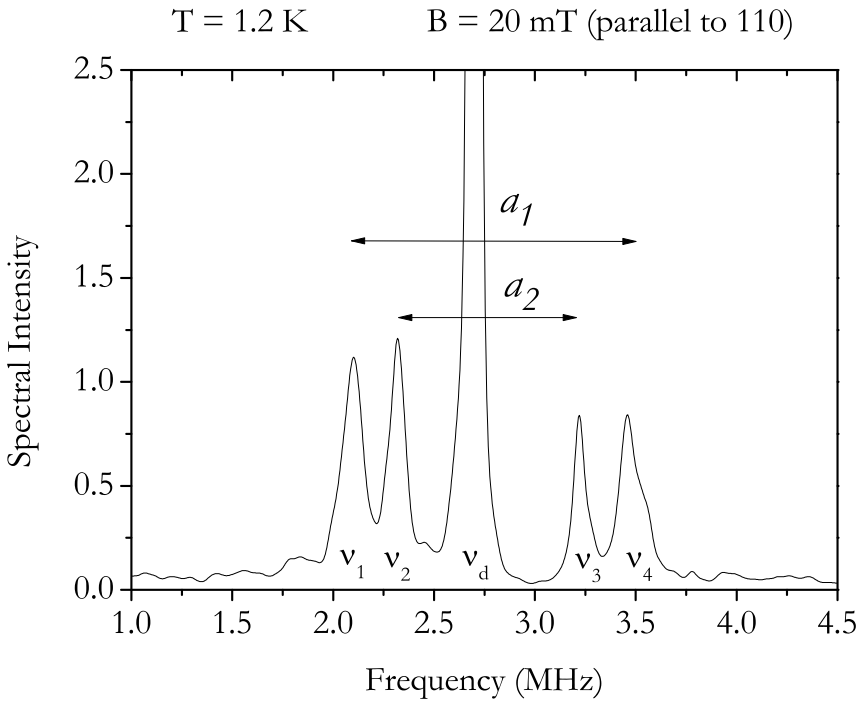

Figure 2.4: *μSR Fourier spectrum of rutile TiO_2 at T = 1.2 K in an external magnetic field of B = 20 mT in the [110] direction. The diamagnetic component (central line at frequency ν_d) and two pairs of hyperfine-split lines (ν_1 to ν_4) are observed.*

2.2.2 Fitting details

Conventional transverse-field B=20 mT parallel to the [110] axis measurements were undertaken from 1.2 K to 10 K and the respective experimental results are presented below. The sample was stored and handled in air.

Figure 2.4 shows the Fourier spectrum of a μSR measurement at 1.2 K in an external magnetic field of 20 mT in the [110] direction. The central line corresponds to the Larmor precession of the bare (diamagnetic) muon and the two pairs of satellite lines are due to the muon - Ti^{3+} polaron with different hyperfine interactions.

In Fig. 2.5 we present the corresponding transverse-field time spectrum of the Fourier spectrum shown in Fig. 2.4. A clear oscillation at the Larmor frequency $\omega/2\pi = (\gamma_\mu/2\pi)$B = 2.71 MHz is observed, corresponding to muons

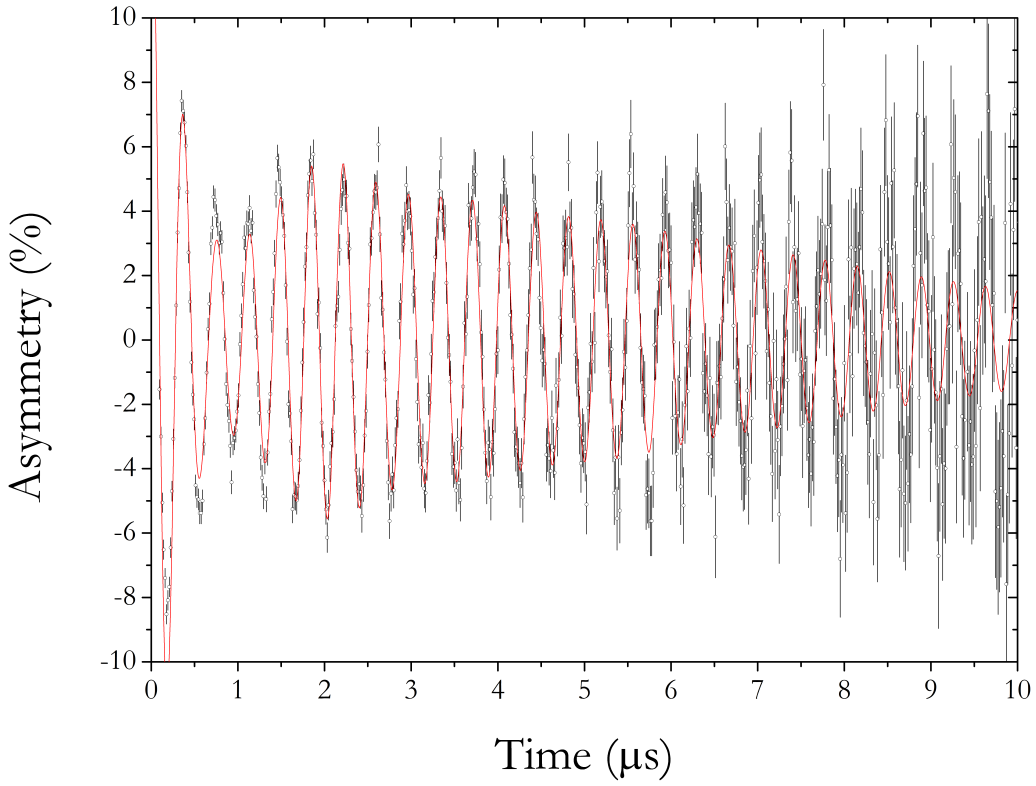

Figure 2.5: *μSR time spectrum of rutile TiO_2 at T = 1.2 K in an external magnetic field of B = 20 mT in the [110] direction. Red line is a fit using a 5 relaxing components as described in the text.*

forming a diamagnetic component. A clear sign of beatings is also visible and we have thus fitted the data with a sum of five components:

$$\begin{aligned} A(t) = A_d e^{-\frac{1}{2}\sigma^2 t} cos(\omega_d t + \phi_d) + \\ + A_{p_1} e^{-\lambda_{p_1} t} cos(\omega_{p_1} t + \phi_{p_1}) + \\ + A_{p_2} e^{-\lambda_{p_2} t} cos(\omega_{p_2} t + \phi_{p_2}) + \\ + A_{p_3} e^{-\lambda_{p_3} t} cos(\omega_{p_3} t + \phi_{p_3}) + \\ + A_{p_4} e^{-\lambda_{p_4} t} cos(\omega_{p_4} t + \phi_{p_4}) \end{aligned} \tag{2.1}$$

where A_d and A_{p_i} are respectively the diamagnetic and muonium like asymmetries (labeled from 1 to 4), σ is the gaussian diamagnetic relaxation, λ_{p_i} are the lorentzian relaxations associated to the muonium like lines, ϕ_d

and ϕ_{p_i} are respectively the diamagnetic and muonium phases. Attending to the fact that this five component fit is very difficult to converge if all parameters are left free, some considerations were made to fix or link some parameters. For the lowest temperatures there was no visible missing fraction, so the total asymmetry (A_{total}) was fixed equal to the value of the silver calibration at 9.4(3) %. The paramagnetic asymmetries (A_{p_i}) were fixed to the lowest temperature values. The relaxations (λ_{p_i}) were linked because at the lowest temperature the differences were in the error range and there was no reasonable explanation for any diference in the relaxation especially having into account the model explained below. After these considerations we obtain the following parameters: $A_d = 5.5(1)$, $\sigma = 0.016(1)\ \mu s^{-1}$ $\lambda_{p_i} = 0.11(1)\ \mu s^{-1}$, $\phi_d = -0.3(8)$ deg, $\phi_{p_1} = 21(14)$ deg, $\phi_{p_2} = 45(19)$ deg, $\phi_{p_3} = -29(11)$ deg, $\phi_{p_4} = -24(9)$ deg and frequencies ($\nu = \omega/2\pi$) $\nu_d = 2.70(1)$ MHz, $\nu_{p_1} = 2.11(1)$ MHz, $\nu_{p_2} = 2.32(1)$ MHz, $\nu_{p_3} = 3.23(1)$ MHz and $\nu_{p_4} = 3.41(1)$ MHz. The corresponding diamagnetic and total muon-Ti^{3+} polaron complex fractions are 60.5(5)% and 39.5(2)%.

2.3 Results

2.3.1 Muon/Hydrogen Configuration

The two different hyperfine interactions experimentally observed and represented in Fig. 2.4 are assigned to the muon-Ti^{3+} polaron complex in the two magnetically inequivalent sublattices of the rutile structure. Figure 2.1 shows a two dimensional sketch of the two sublattices as well as the corresponding three dimensional representation. The top representation consists of Ti^{3+} (Ti^{4+} plus one electron) in the center and six oxygen atoms arranged in a slightly distorted octahedron. The second sublattice has the same structure as the first one but is rotated by 90° around the c-axis. The muon and hydrogen are bound to one of the six oxygen atoms surrounding Ti^{3+}. At the lowest temperatures of the experiment (1.2 K in μSR to be compared with ENDOR at 5 K) only the bond to oxygen atoms in the same $a-b$ plane in which Ti^{3+} is situated is realized. A detailed justification of this assignment will be given below.

Table 2.1: *g matrix and hyperfine interaction matrix parameters of the hydrogen using ENDOR experiment [8]*

Matrix type	Principal value	Principal-axis direction
g matrix		
g_1	1.9765 ± 0.0002	19.0^o from [110]
g_2	1.9732 ± 0.0002	19.0^o from [110]
g_3	1.9405 ± 0.0002	[110]
hydrogen hyperfine matrix		
A_1	+0.616 MHz±0.01 MHz	22.9^o from [110]
A_2	-0.401 MHz±0.01 MHz	22.9^o from [110]
A_3	-0.338 MHz±0.01 MHz	[001]

First we recall the results of the ENDOR experiment for proton in TiO_2 which should be directly comparable to those obtained for μSR, after taking into account that the magnetic moments of the muon and proton are different ($\mu_\mu/\mu_p = 3.183$). Brant et al. [8] have determined the precise geometrical configuration of the hydrogen donor in TiO_2, which we reproduce in Fig. 2.7. The corresponding electronic-tensor and hyperfine tensor are summarized in Table 2.1.

The hyperfine interactions of the proton and of the muon cannot be compared directly since the present experiment was performed at a rather low field where the line splitting does not correspond exactly to the hyperfine interaction. We therefore calculated the line positions with the hyperfine parameters of the ENDOR experiment (Table 2.1), multiplied by the ratio of the magnetic moments, and compared these with the present data. To calculate the line positions one needs to have a few geometric considerations to set up the moun complex hyperfine tensor which we will now describe. We started by obtaining the corresponding principal values for the hyperfine tensor for the muon-Ti^{3+} polaron complex, multiplying those obtained from ENDOR(Table 2.1) by 3.183. We get $A_1 = 1.96$ MHz, $A_2 = -1.28$ MHz and $A_3 = -1.08$ MHz. In order to apply Hurst formulae (Equation 1.41), we must obtain the hyperfine tensor in the frame defined by the principal directions of the g-tensor. This is obtained by an (active) rotation of the hyperfine tensor

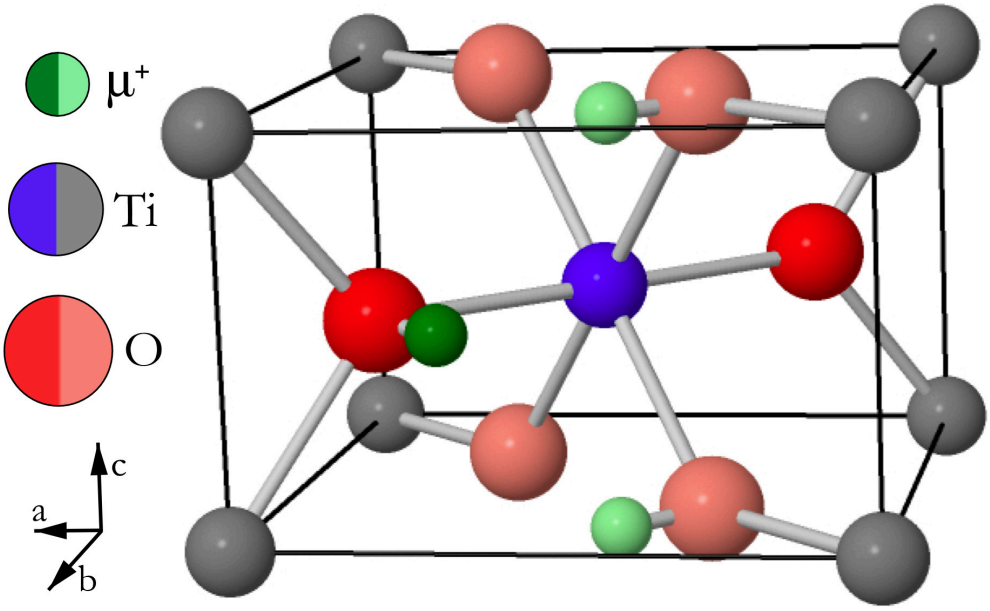

Figure 2.6: *Sketch of the TiO_6 octahedron in rutile TiO_2 with Ti^{3+} in the center and six oxygen atoms surrounding it. At low temperatures, the muon (hydrogen) is bound to one of the six oxygen of the slightly distorted octahedron. In the ground state only the bond to oxygen in the same a-b plane as Ti^{3+} is realized (see text). Only one of the two magnetically inequivalent TiO_6 complexes is shown (sublattice 1), the other one (sublattice 2) is rotated by 90° around the c-axis*

by $\alpha = +3.9$ degrees (difference between the principal-axis direction of the g tensor vectors and the hyperfine vector as seen in Fig. 2.7) counterclockwise with respect to the z-axis (which corresponds to the c- axis). The active rotation matrix is:

$$R(\alpha) = \begin{pmatrix} \cos\alpha & -\sin\alpha & 0 \\ \sin\alpha & \cos\alpha & 0 \\ 0 & 0 & 1 \end{pmatrix} \tag{2.2}$$

and the rotated tensor is:

$$A = RA_{dia}R^T = \begin{pmatrix} A_1\cos^2\alpha + A_2\sin^2\alpha & (A_1 - A_2)\sin\alpha\cos\alpha & 0 \\ (A_1 - A_2)\sin\alpha\cos\alpha & A_1\cos^2\alpha + A_2\sin^2\alpha & 0 \\ 0 & 0 & A_3 \end{pmatrix} \tag{2.3}$$

this results in (in MHz):

$$A = RA_{dia}R^T = \begin{pmatrix} 1.95 & -0.22 & 0 \\ -0.22 & -1.26 & 0 \\ 0 & 0 & -1.08 \end{pmatrix} \tag{2.4}$$

(Alternatively, we could have done a clockwise passive rotation of the reference frame by -3.9 degrees with respect to the z-axis, where the passive rotation matrix by an angle α is R^T).

After that we must rotate the hyperfine tensor from the in-plane position to an out-of-plane position. Starting from the hyperfine tensor presented above (matrix 2.4), which corresponds to the situation sketched in Fig. 2.7 and to the in-plane Ti_a - O_a bond shown in Fig. 2.1(top), we may obtain the hyperfine tensor corresponding to the out-of-plane configurations (Fig. 2.1(bottom)) by the following procedure:

1. Perform an active rotation of the hyperfine tensor by $\alpha = \pm 90$ degrees with respect to the z axis/c-axis; the corresponding rotation matrix is the same as above: $R_1 = R(\alpha)$.

2. Perform an active rotation of the hyperfine tensor by ± 49.3 degrees with respect to the 110 axis. The best way to do so is the following:

(a) perform a passive rotation of the reference frame in order to get a new x axis parallel to the 110 axis: this implies a passive rotation of +71 degrees

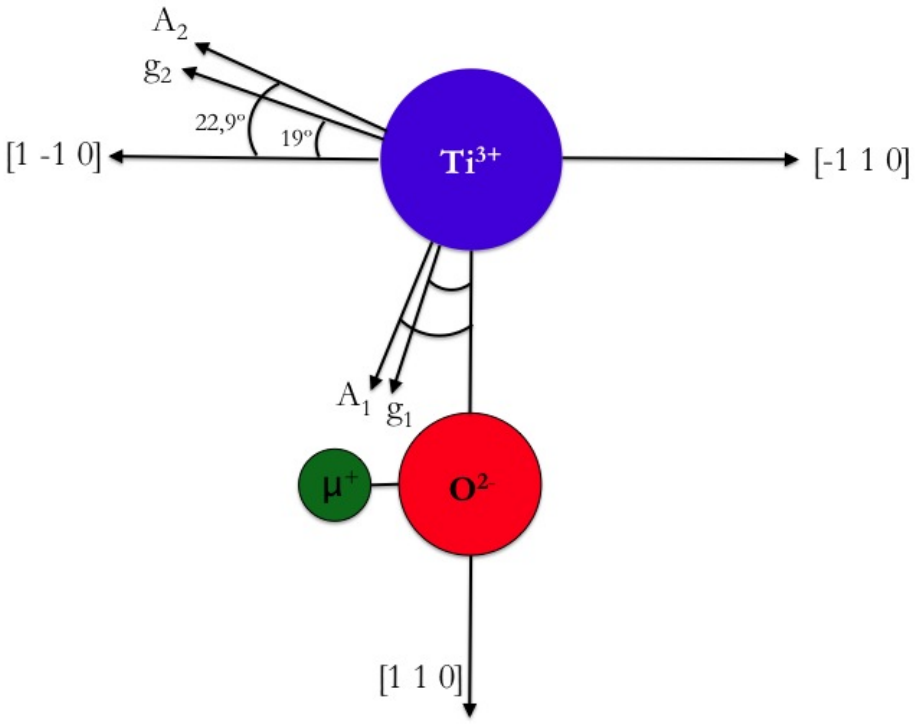

Figure 2.7: *Sketch of the angle relation between the hyperfine tensor and the g tensor in the $a-b$ plane*

(counterclockwise) around the z-axis/c-axis. The corresponding rotation matrix is:

$$R_a = \begin{pmatrix} \cos 71 & \sin 71 & 0 \\ -\sin 71 & \cos 71 & 0 \\ 0 & 0 & 1 \end{pmatrix} \tag{2.5}$$

(b) then perform an active rotation of ± 49.3 degrees of the hyperfine tensor with respect to the x-axis/110 axis. The corresponding rotation matrix is:

$$R_b = \begin{pmatrix} 1 & 0 & 0 \\ 0 & \cos 49.3 & -\sin 49.3 \\ 0 & +\sin 49.3 & \cos 49.3 \end{pmatrix} \tag{2.6}$$

(c) finally cancel the initial passive rotation by performing a passive rotation of the reference frame in the opposite direction. The corresponding rotation matrix is:

$$R_a = \begin{pmatrix} \cos -71 & \sin -71 & 0 \\ -\sin -71 & \cos -71 & 0 \\ 0 & 0 & 1 \end{pmatrix} \tag{2.7}$$

The overall rotation matrix is therefore $R_2 = R_c R_b R_a$

The rotated tensor is therefore:

$$A_{out-of-plane} = R_2 R_1 A_{in-plane} R_1^T R_2^T = R_c R_b R_a R_1 A_{in-plane} R_1^T R_a^T R_b^T R_c^T \tag{2.8}$$

which results in:

$$A_{out-of-plane} = \begin{pmatrix} -1.168 & 0.352 & -1.477 \\ 0.352 & 0.389 & -0.422 \\ -1.477 & -0.422 & 0.388 \end{pmatrix} \tag{2.9}$$

Using the rotated hyperfine tensor $A_{out-of-plane}$ calculated above, we may use Hurst formulae (equation 1.41) to calculate the expected frequencies. We present in Table 2.2 the results for the two most interesting orientations, with transverse field parallel to [001] and parallel to [110]. In the [110] case, we

must, as usual, take into account the two cases corresponding to the different Ti sublattices:

$\phi = 71$ degrees (for example, field parallel to in-plane Ti_a-O_a bond), where the magnetic field is perpendicular to the in-plane O-muon bond (sublattice-1: top part of Fig. 2.1);

$\phi = -19$ degrees (for example, field perpendicular to in-plane Ti_b-O_h bond), where the magnetic field is parallel to the in-plane O-muon bond (sublattice-2: bottom part of Fig. 2.1);

We have calculated the frequencies for all 8 out-of-plane possibilites (rotations of ±90 degrees and ±49.3 degrees for both sub-lattices). We always get the same numbers, as expected.

The results of the expected frequencies using the scaled hyperfine parameters are shown in Table 2.2.

Table 2.2: *Expected frequencies for the muonium like lines calculated using the Hurst formulae (equation 1.41). α and β are the spin states (up and down). In the text the first sub table will be known as a) the second sub table as b) and the third sub table as c)*

	$\theta = 90, \phi = 71$			$\theta = 90, \phi = -19$			$\theta = 0$		
	ν_α	ν_β	$\lvert\nu_\alpha - \nu_\beta\rvert$	ν_α	ν_β	$\lvert\nu_\alpha - \nu_\beta\rvert$	ν_α	ν_β	$\lvert\nu_\alpha - \nu_\beta\rvert$
Out-of-plane	3.147	2.379	0.768	2.795	2.801	0.006	2.621	2.994	0.373
In-plane	2.048	3.484	1.436	3.147	2.379	0.768	3.238	2.162	1.076

Assuming $A_3 = 0$

	ν_α	ν_β	$\lvert\nu_\alpha - \nu_\beta\rvert$	ν_α	ν_β	$\lvert\nu_\alpha - \nu_\beta\rvert$	ν_α	ν_β	$\lvert\nu_\alpha - \nu_\beta\rvert$
Out-of-plane	3.147	2.379	0.768	2.445	3.058	0.613	2.348	3.175	0.827
In-plane	2.048	3.484	1.436	3.147	2.379	0.768	2.702	2.702	0.000

Assuming $A_1 = 1.9$ MHz, $A_2 = -1.45$ MHz, $A_3 = 0$

	ν_α	ν_β	$\lvert\nu_\alpha - \nu_\beta\rvert$	ν_α	ν_β	$\lvert\nu_\alpha - \nu_\beta\rvert$
Out-of-plane	3.228	2.308	0.920	2.460	3.041	0.581
In-plane	2.093	3.451	1.358	3.229	2.310	0.919
Experimental	2.11	3.41	1.30	3.23	2.32	0.91

These calculations assume that the isotropic part of the hyperfine constant for the out-of-plane is the same. In reality it depends on the overlap

between Ti d-electrons and oxygen orbitals and that may not be quite the same for the in-plane Ti-O bonds as for the out-of-plane ones. Also, the muon (and hydrogen) is bound to one of the six oxygen atoms of the TiO_6 octahedron (see Fig. 2.6). However, these O atoms and the corresponding bonds are not equivalent: The oxygen atoms which are in the same $a-b$ plane as Ti^{3+} ("in-plane") differ slightly from the O atoms in the planes below and above this plane ("out-of-plane"). The muon (hydrogen) bonds to the in-plane oxygen form the ground state. Only this configuration is consistent with the experimental hyperfine interaction observed in μSR and ENDOR. At 1.2 K in μSR and at 5 K in ENDOR only the ground state is occupied. We recall that there are two sublattices, rotated by 90°, which give rise to the two pairs of hyperfine lines seen in Fig. 2.4. Both pairs correspond to the ground state configuration but they refer to different sublattices. The excited state which becomes populated with increasing temperature corresponds to the configuration where the muon (hydrogen) is bound to an out-of-plane oxygen. The same assignment was made by Stavola et al. [7] in an IR study of vibrational modes of deuterium in rutile TiO_2. The hyperfine values of the out-of-plane configurations are not known experimentally, but are shown above calculated with the scaled principal axes values from the ENDOR experiment. We have seen that the predicted frequencies of the excited state in sublattice 2 (Fig. 2.6, TiO_6 octahedron rotated by 90°) are the same as those of the ground state in sublattice 1 (TiO_6 octahedron as shown in Fig. 2.6). This is also plausible from symmetry consideration. Thus we take the experimental frequencies of the inner lines in Tab. 2.3 as the frequencies of the excited state in sublattice 2. For the excited state in sublattice 1 we rely completely on calculation. The calculated values are sensitive to the A_3 value. We recall that the A_3 is close to zero in the muon case (Fig. 2.8) and that this reduction in comparison to the ENDOR value likely arises to a larger zero-point motion of the muon in the c-direction. We have thus taken $A_3 = 0$ in the calculation of the frequencies of the exited state in sublattice 1 (Table 2.2 b). For all other frequencies we used experimental values in the simulation of the spectra.

The corresponding calculated frequencies are shown in Table 2.2 b. In Table 2.2 c a refined version of Table 2.2 b is shown, where the A_1 and

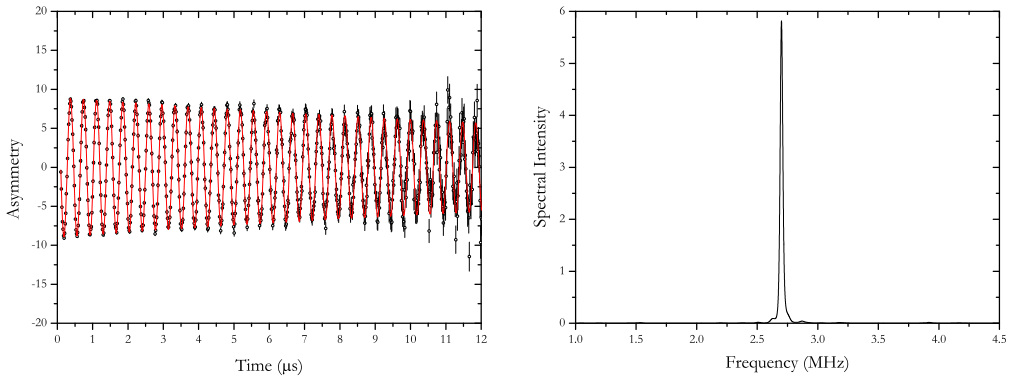

Figure 2.8: *μSR time spectrum (right) and corresponding Fourier spectra (left) of rutile TiO_2 at $T = 1.2$ K in an external magnetic field of $B = 20$ mT in the [100] direction. Red line is a fit using a 1 relaxing component fit*

A_2 parameters were assumed in order to fit the experimental values for the frequencies.

For these calculations we note that the frequencies obtained for the case where the magnetic field is parallel to the in-plane O-moun bond ($\phi = -19$ degrees) are practically the same as those of the out-of-plane case for $\phi = 71$ degrees. These correspond to our observed inner lines and are highlighted in red in Table 2.2. This suggests that the out-of-plane O-muon bond is somehow kept parallel to the [100] plane.

For the other case, things are much different: the frequencies obtained when the magnetic field is perpendicular to the in-plane O-muon bond ($\phi = 71$ degrees) are widely spaced, corresponding to the observed splitting of the outer lines of about 1.3 MHz. However, the corresponding situation for the out-of-plane configuration yields a very narrow splitting, so that these lines are nearly collapsed over the diamagnetic line.

The out-of-plane lines either coincide with the inner lines or with the diamagnetic line. However, if the out-of-plane positions were occupied, the spectral weight of the inner lines would be double of that of the outer lines. Although it is very hard to extract precise values for the asymmetries, we have no evidence of any asymmetry unbalance of any sort.

Again, for the out-of-plane configuration, the expected line splitting for the case where the magnetic field is parallel to the [001] direction is much smaller than for the in-plane case. We recall that we do not observe any splitting at all for this geometry and the line broadening obtained is $\sigma = 0.016(1)\mu s^{-1}$ for the gaussian relaxation of the line. This does not seem compatible even with a broadening due to the out-of-plane line splitting calculated.

We so conclude that the measured lines are due to muons stopping at the in plane sites in the two sublattices. In Table 2.2 b we present the line splitting which is a measure of the hyperfine interaction. It deviates by about 10 to 15 % from the calculated value, slightly outside the quoted errors. Experimental uncertainties, e.g. deviation from the nominal field orientation, could partially or fully account for this discrepancy. On the other hand a difference in the hyperfine interactions (normalized with the magnetic moments) cannot be excluded (Table 2.2 c). In particular, larger zero-point motions of the muon compared to hydrogen could yield differences in the average hyperfine values. However, the main result of this comparison is that the probe atom is bound to oxygen of the TiO_6 octahedron around Ti^{3+} and this geometry is the same for muon and proton. We compare here muon results obtained at 1.2 K with hydrogen data measured at 5 K. This is justified since in both cases the static situation is realized. The μSR data at 5 K would not be adequate for comparison since there is some dynamics involved as will be shown below.

2.3.2 Muon dynamics

The development of the spectral lines with increasing temperature is shown in Fig. 2.9. It can be seen that the hyperfine splitting gets smaller with increasing temperature and disappears completely at the still low temperature of 10 K. Furthermore, the two pairs of lines merge into one visible pair already above 3.8 K.

The first question we want to answer is whether the disappearance of the hyperfine interaction is due to dissolution of the muon-electron complex or to local dynamics. A separation of the muon from the electron or vice

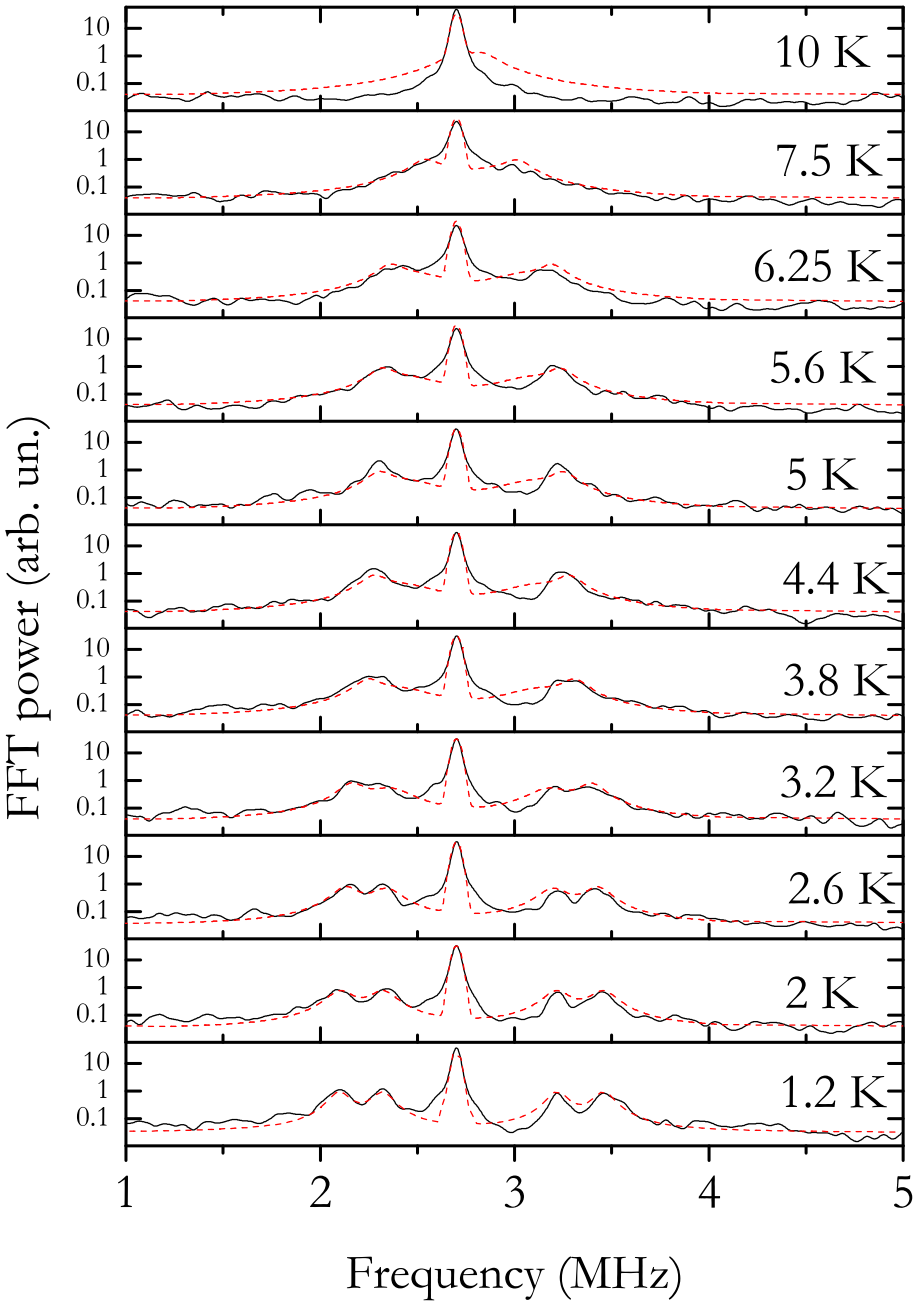

Figure 2.9: *Development of the line spectra as a function of temperature. The dashed red lines are fits assuming an oscillation of the muon between neighboring bonding positions (see text).*

Table 2.3: *Comparison of the frequencies obtained in the μSR experiment with the frequencies calculated with the hyperfine interaction parameters of the hydrogen ENDOR experiment [8] scaled with the magnetic moment ratio of the muon and the proton (this ratio is 3.183). The fourth and seventh column of Tab. 2.3 show the line splitting which gives a rough estimate of the hyperfine interaction. For the inner lines a negative hyperfine interaction was assumed (the sign is not measured in the μSR experiment). These data refer to TiO_2 with the magnetic field of 20 mT in the [110] orientation. The assignment to sublattice 1 and sublattice 2 is discussed in the text.*

	Outer lines (sublattice-1)			Inner lines (sublattice-2)		
Frequencies	ν_1	ν_4	ν_4-ν_1	ν_2	ν_3	ν_2-ν_3
Experimental (MHz)	2.12(2)	3.43(2)	1.31(3)	2.30(2)	3.20(2)	-0.90(3)
Calculated from ENDOR (MHz)	2.05(3)	3.48(3)	1.43(4)	2.38(3)	3.15(3)	-0.77(4)

versa would result in an increase of the diamagnetic and a decrease of the paramagnetic fraction in the μSR experiment. This is, however, not the case, at least not up to 7.5 K. In this temperature range, the paramagnetic fraction determined by adding the intensities of the hyperfine lines or, at the higher temperatures, via the intensity of the broader line, is constant and amounts to about 40% of all muons (Fig. 2.10). Thus the collapse of the hyperfine splitting must be due to some local dynamics or rearrangements.

There is overwhelming evidence in the literature that the Ti^{3+} polaronic state is stable at temperatures below 10 K. The EPR signal of Ti^{3+} was seen at least up to 60 K in studies of rutile TiO_2 [60, 61]. The temperature dependence of Ti^{3+} was investigated explicitly in a recent EPR experiment [62]. The authors of this paper find that the Ti^{3+} center becomes unstable above 15 K on a time scale of 100 seconds. The activation energy for the disappearance of the signal is 24 meV. On the basis of this result one can conclude that Ti^{3+} is definitely stable on a timescale of 10^{-6} s in the temperature region below 10 K, i.e. at the conditions of the present experiment. The EPR experiment excludes also fast spin flips below 10 K. These findings are for the intrinsic polaron but they apply a fortiori also for the trapped Ti^{3+}. Thus a local motion or site change of the muon must be the cause for the evolution of the μSR spectra with temperature.

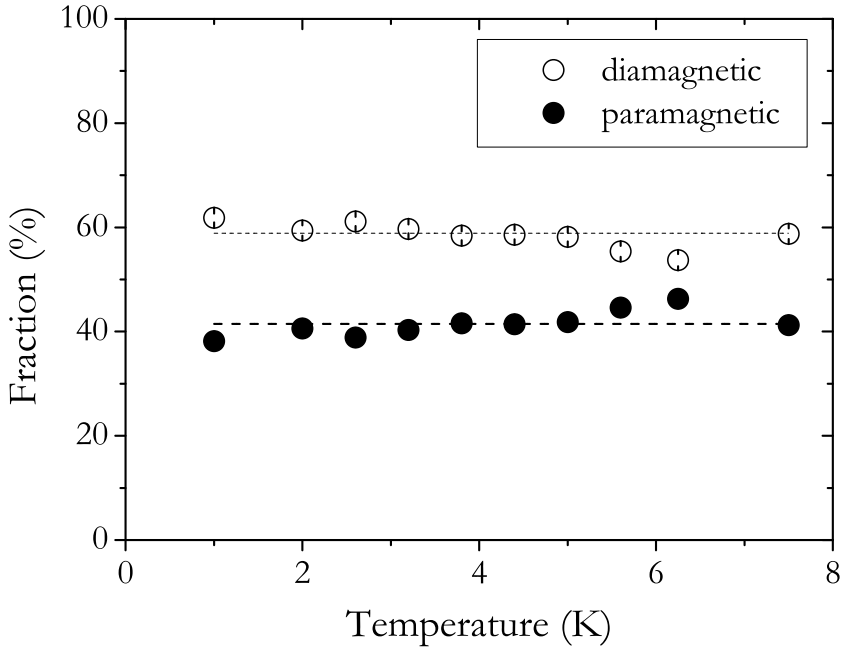

Figure 2.10: *Temperature dependence of the diamagnetic and paramagnetic fractions with corresponding fit to a constant .*

Gradual population of the excited state, without changing the frequencies, cannot explain the shrinking of the hyperfine splitting with temperature. We therefore assume that, at least in μSR, jumps between the two configurations occur. A complete averaging over all bonding sites seems unlikely because of geometric constraints. In the rutile structure, empty oxygen channels occur parallel to the c-axis and the muon (hydrogen) is assumed to be located inside these channels [63]. A movement of the muon out of a channel is prohibited at this low temperature due to a relatively large energy barrier. But an oscillation between neighboring bonds in the same oxygen channel is quite reasonable. As indicated in Fig. 2.11, jumps may occur between position 1 (muon bound to the in-plane oxygen) and position 2 (muon bound to either one of the out-of-plane oxygen below or above the plane), the muon remains thereby in the same oxygen channel and in the same sublattice, and the electron spin direction does not change.

We treat the site change movement in the fast jump limit. This is justified

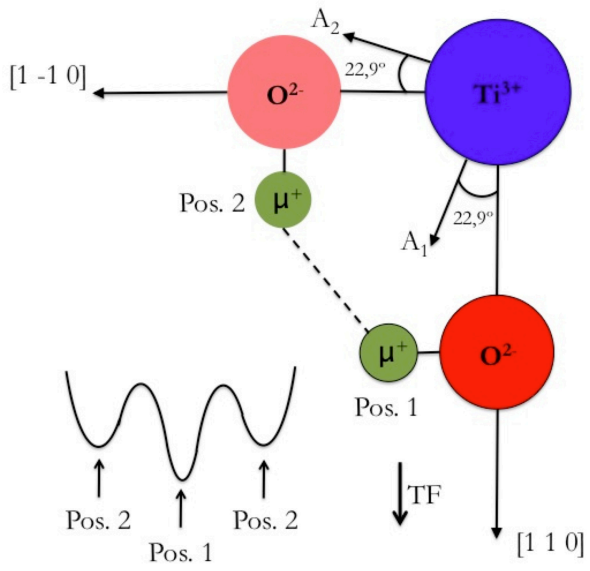

Figure 2.11: *Sketch of the two muon configurations in rutile TiO_2. The projection on the (001) plane is shown. The particles with the bright colors and the solid boarders lie in the same a-b plane as Ti^{3+}, while the others are below and above this plane (adopted from Refs. [8, 64]). Site changes (dashed line) are possible between the two muon positions in the same oxygen channel. In the lower left corner a schematic sketch of the potential between the two sites is displayed. A1 and A2 represent the principal axes directions of the hyperfine tensor in the (001) plane (index 1 and 2 are interchanged compared to their use in Ref. [8])*

since it leads to the observed shrinkage of the hyperfine splitting. For slow jumps the frequencies would basically stay at their positions and only the intensities would change with temperature. But this is not observed. In the fast jump limit the average frequency ν is given by

$$\nu_i = (1 - f) \times \nu_{i(groundstate)} + f \times \nu_{i(excitedstate)} \tag{2.10}$$

The index i runs from 1 to 4 and f is the population probability of the excited state. For $\nu_{i(groundstate)}$ we take the four frequencies shown in Fig. 2.4 and for $\nu_{i(excitedstate)}$ the estimated frequencies as discussed in the text. Averaging occurs only for the ν_i pairs of the same oxygen channel and the same sublattice. This corresponds to an oscillation of the muon between position 1 and position 2 as indicated in Fig. 2.11. We fitted the spectra in Fig. 2.9 allowing the frequencies ν_i to vary according to Eq. 2.10; the only free parameter is the fraction f of the excited state. The development of the spectra is well reproduced by this model (dashed red lines in Fig. 2.9).

It is somewhat surprising that a small change of the muon position leads to such a drastic change of the hyperfine interaction. The reason for this unusual behavior lies in the strong anisotropy of the dipolar interaction (ideal dipole angular distribution: $3\cos^2\theta - 1$). In the present case, the frequencies which have to be averaged lie on different sides of the diamagnetic line. Thus the averaging leads to a reduction of the hyperfine splitting as observed experimentally.

Figure 2.12 shows the population probability f of the excited state obtained from the fit with Eq. 2.10. The solid and dashed line in Fig. 2.11 are adjustments with a Boltzmann distribution:

$$f = \frac{2e^{\frac{-\Delta E}{kT}}}{1 + 2e^{\frac{-\Delta E}{kT}}} \tag{2.11}$$

ΔE is the energy difference between the ground state and the excited state. The factor 2 in Eq. 2.11 takes into account that two bonds are available for the excited state whereas only one bond exists for the ground state. Thereby it is assumed that the muon stays in the oxygen channel and remains bound to Ti^{3+} (see Fig. 2.11).

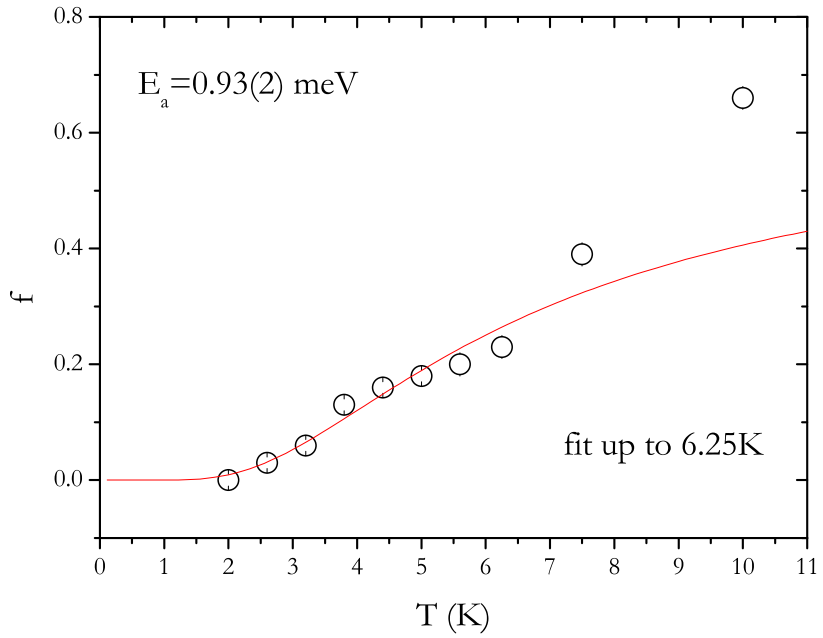

Figure 2.12: *Population probability f of the excited state as a function of temperature. The solid line is a fit with a Boltzmann distribution for all data points, the dashed line is for data up to 6.25 K. The fitted activation energies are given in the figure.*

The fit to all data points up to 10 K yields ΔE= 0.8(1)meV for the muon in good agreement with values obtained by Herklotz et al. [65] in an IR study of hydrogen in rutile TiO_2. They report ΔE = 1.00(5) meV for hydrogen and ΔE = 1.2(1) meV for deuterium. This comparison indicates a small but not very significant isotope effect.

In Ref. [65] as in the present analysis only the ground state and the first excited state were considered. Stavola et al. [7] included in their IR study a third state with excitation energy of 11 meV and a height weighting factor. In this analysis the splitting of the ground state and the first excited state came out to be ΔE = 0.9(1) meV for deuterium. We suppose that our data points at 7.5 K and 10 K, where the fits are not good, are also influenced by this third state. If we include only the data up to 6.25 K, the fit in Fig. 2.12 (dashed line) yields 0.9(1) meV in agreement with the value obtained by

Stavola et al. [7]. Thus in μSR there is also indication of the excitation of this third state but because of the limited temperature range no further specification can be made. Stavola et al. [7] assigned this third state to hydrogen bound to oxygen atoms further away from Ti^{3+} than the six atoms of the octahedron in Fig. 2.6.

2.4 Conclusions

In summary, we show via a comparison of the hyperfine interactions that in rutile TiO_2 muon and proton form the same configuration and the electronic structure is the same within the experimental uncertainty. Deviations of the hyperfine values of the two species besides the scaling with the magnetic moments can be explained by a larger zero-point motion of the muon compared to hydrogen.

In addition, a detailed description of the low temperature bonding configurations is presented: the central part of the configuration consists of Ti^{3+}, at which the donor electron is mainly localized, surrounded by six oxygen atoms. The muon, and the proton in the hydrogen case, is bound to one of the six oxygen of this TiO_6 complex. However, these bonds are not equivalent. The ground state is formed by bonding to the "in-plane" oxygen only; these are the oxygen atoms which are in the same a-b plane as Ti^{3+}. Two different hyperfine interaction occur (two pairs of lines in Fig. 2.4) since the muon may be in either one of the two magnetically inequivalent TiO_6 sublattices (octahedra rotated by 90° around the c-axis).

In the excited state, bonds to the remaining oxygen of the TiO_6 octahedron ("out-of plane") are realized. The gradual population of the excited state with increasing temperature and rapid fluctuations between the corresponding bonding sites leads to the collapse of the hyperfine interaction. These site changes occur within the same oxygen channel and in the same TiO_6 sublattice.

The present data indicate an energy difference between ground state and excited state of about 0.9(1) meV. Because of the rather limited temperature range of the present study the value is not very precise but it is in the same order of magnitude as the ΔE quoted in Ref. [7] for deuterium (also 0.9 meV).

A rather low energy difference between the ground state and the first excited state is expected since the bonds in the TiO_6 are almost equivalent.

Chapter 3

Zirconia

3.1 Introduction

3.1.1 Motivation

Zirconia is a ceramic material with diverse uses as oxygen sensor, thermal barrier coating, cladding material for nuclear reactors, among others. It has also been considered as one of the high-permittivity (κ) oxides that may replace SiO_2 as the gate dielectric in metal-oxide-semiconductor devices[45]. The use of high-κ oxides will allow a thicker layer for the gate dielectric, thus decreasing tunnelling currents[45] while achieving the same level of capacitance. Zirconia possesses relatively high dielectric constant varying from 22(1) for the undoped monoclinic phase to 38(4) for yttria-stabilised zirconia [66] and acts as an insulator with a 5.2 to 5.8 eV gap width.[15] Zirconia is also commonly used as the solid electrolyte in solid-oxide fuel-cell technology,[67] where the electrical conduction is governed through the motion and mobility of oxygen vacancies.[6] The relevant phase of zirconia in this case is the cubic phase rather than the ground-state monoclinic owing to superior mechanical and electrical properties of the former.

As stated in Chapter 1, hydrogen is an ubiquitous impurity in materials and zirconia is not an exception. It is frequently incorporated during processing of zirconia and if no special treatment is applied to the sample the expected hydrogen concentration in a given sample should be in the order

of 1 $\times 10^{18}$ atoms/cm^3. [68] In zirconia, hydrogen effects have been principally related to proton conduction. There is accumulated evidence from recent studies that in dense nanostructured zirconia the ionic conductivity above room temperature can be dominated by proton conductivity at the grain boundaries.[6, 69] The adsorption of water molecules at the surface seems to play an important role in this process.[69] This has even led to proposals of room-temperature operating devices using proton-conducting electrolytes.[70] The proton diffusion is thought to occur via the Grötthus mechanism with proton hopping between adjacent oxygen ions. However, these conclusions are based upon purely macroscopic electrical impedance measurements, from which it is very difficult to disentangle the sintering effect from that of dehydration.[68]

From a theory standpoint, hydrogen states in zirconia have been studied in the past by first-principles calculations, nonetheless with the exception of an earlier attempt by μSR [11] a detailed experimental confirmation and analysis is still largely lacking. More specifically, DFT-based calculations determined the type of hydrogen configurations and defect electrical levels for hydrogen in the monoclinic [71, 5], the ideal cubic[72, 73] and tetragonal[74] and the cubic yttria-stabilized[15] phases. For bulk crystalline yttria-stabilized zirconia (YSZ)[15], in particular, the calculations have also probed the migration behavior of hydrogen for various representative pathways inside the oxide. The hyperfine constants of the neutral hydrogen state were also obtained for the bulk YSZ and for certain hydrogen configurations at the core of a high-angle grain boundary.[17]

3.1.2 The phases of zirconia

At room temperature pure zirconia has a monoclinic structure. This phase takes place at temperatures below 1170°C, with a 6.09 g/cm^3 density. (Zr^{4+}) cations are placed in planes parallel to the "c" axis, separated by (O^{2-}) anions planes. Each Zr^{4+} is surrounded by seven oxygen ions, so that it is triangularly coordinated with the oxygen ions from one plane and tetrahedrally with the oxygen ions from another plane sketched in Fig. 3.1c.

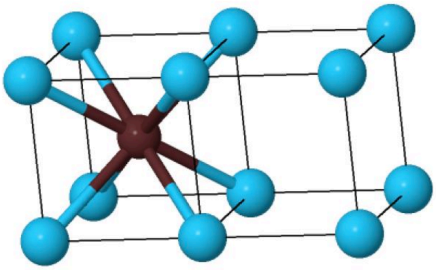

(a) *Cubic*

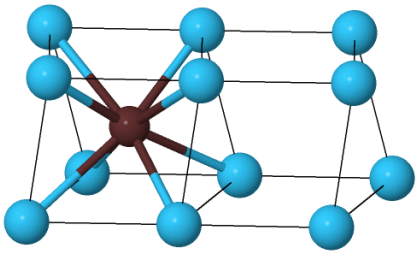

(b) *Tetragonal*

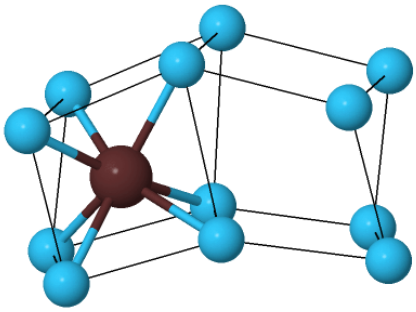

(c) *Monoclinic*

Figure 3.1: *Schematics of the crystal structure of the three most important zirconia phases.*
a) Cubic phase, highlighting the alternation between cubes with and without a Zr cation.
b) Tetragonal phase, that we can see is a distorted cubic phase (distortion along the "ab" plane).
c) Monoclinic phase, and additional distortion in the "c" direction when compared to the tetragonal phase, that implies that each Zr cation now coordinates with 7 oxygen atoms only.
Blue spheres represent oxygen anions and the dark-brown sphere represents the zirconium cation.

The layer thickness is larger when the Zr ions are separated by ions from the plane with which they are triangularly coordinated than when they are separated by ions from the plane with which they are tetrahedrally coordinated.

Between 1179°C and 2340°C a tetragonal phase is exhibited with a 6.10 g/cm^3 density. It has a structure where each Zr^{4+} is surrounded by eight oxygen ions, four of them at a distance of $2,455$ Å and the remaining four at $2,650$ Å sketched in Fig. 3.1. This structure is similar to a distortion of the cubic fluorite structure [75]. Above 2340°C zirconia has a cubic fluorite structure sketched in Fig. 3.1.

At low temperatures the cubic phase can be stabilized by suitable doping with tri-valent or divalent transition-metal oxides (Y_2O_3, Sc_2O_3, MgO, CaO) which also leads to the formation of oxygen vacancies in the lattice as charge-compensating defects.

3.1.3 Theoretical results

As discussed in chaper 1 semi-local DFT calculations are a powerful tool to help explaning the μSR experimental data and hence to give a more complete picture of hydrogen behaviour in materials. As mentioned in the introduction (Chapter 1) Dr. Apostolos Marinopoulos has performed extensive theoretical modelling of the hydrogen impurity in zirconia using *ab-initio* methods [15, 17]. In particular semi-local DFT calculations were used to obtain the minimum-energy supercells of the bulk crystalline scandia-stabilized zirconia (ScSZ) and YSZ cubic phase.

We now briefly summarize the results of these *ab-initio* calculations. The formation-energy plot for the low-energy charge states of hydrogen is shown in Fig. 3.2a for ScSZ and Fig.3.2b for YSZ, as a function of the Fermi-level position in the band gap, E_{gap}. In the same figure the thermodynamic charge-transition levels are indicated by the vertical lines. These results show that the isolated hydrogen impurity is an amphoteric defect in cubic ScSZ as well as in YSZ with the pinning level $E(-/+)$ lying well within the energy gap of the host [15]. This is consistent with the behavior of hydrogen in monoclinic phase of pure zirconia.[5] Furthermore, both the acceptor and donor levels,

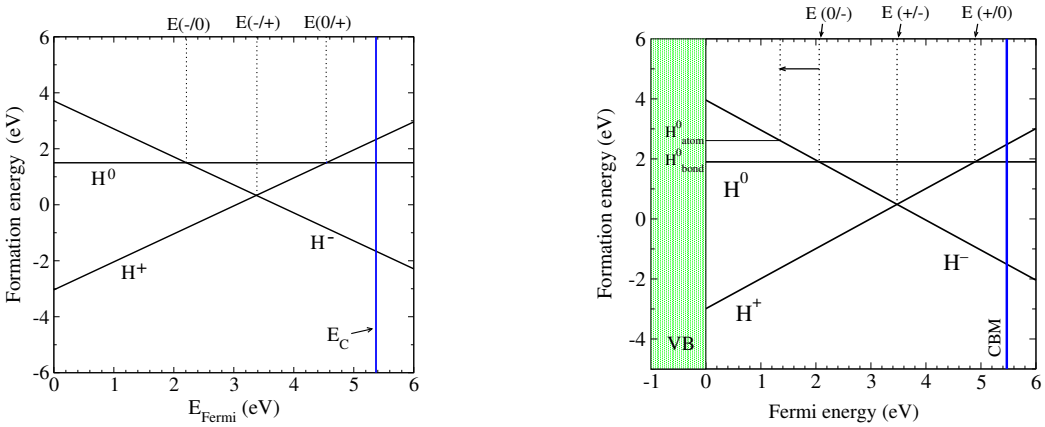

(a) *ScSZ* **(b)** *YSZ*

Figure 3.2: *Formation-energy plot of the different charge states of hydrogen in ScSZ (a) and YSZ (b) as a function of the Fermi-level position in the gap. The plot shows the results obtained by DFT calculations. The thermodynamic charge-transition levels, $E(q/q')$, are denoted by the vertical lines. The valence-band edge (Fermi energy = 0) defines the reference energy for the Fermi level which spans the band gap up to the conduction-band minimum (E_C in (a) and CMB in (b)). The plot depicts the formation energies of the lowest-energy structures that hydrogen forms in the ScSZ (a) and YSZ (b) [15] cell for each of its charge states.*

$E(-/0)$ and $E(0/+)$, respectively, are deep levels that lie appreciably away from the respective bands edges (E_V and E_C), with positions at: $E(-/0) = E_V + 2.21$ eV and $E(0/+) = E_C - 0.83$ eV for ScSZ and $E(-/0) = E_V + 2.06$ eV and $E(0/+) = E_C - 0.58$ eV for YSZ. These results suggest that thermal ionization of neutral hydrogen at low and moderate temperatures is extremely difficult.

For the lowest energy structure in the oxygen bound configuration the corresponding spin-density profile calculated DFT, shown in Fig. 3.3a and Fig. 3.3b, suggests clearly that neutral hydrogen in ScSZ and in YSZ is not a shallow-donor defect. Instead, the electron possesses a very compact (localized) 4d-type density distribution rather than a delocalized character, confirming its deep-donor nature as inferred from the formation-energy plot (see Fig. 3.2a and Fig. 3.2b). It can also be seen that it is trapped at neighboring Zr ions, with an asymmetric distribution. The spin density displays

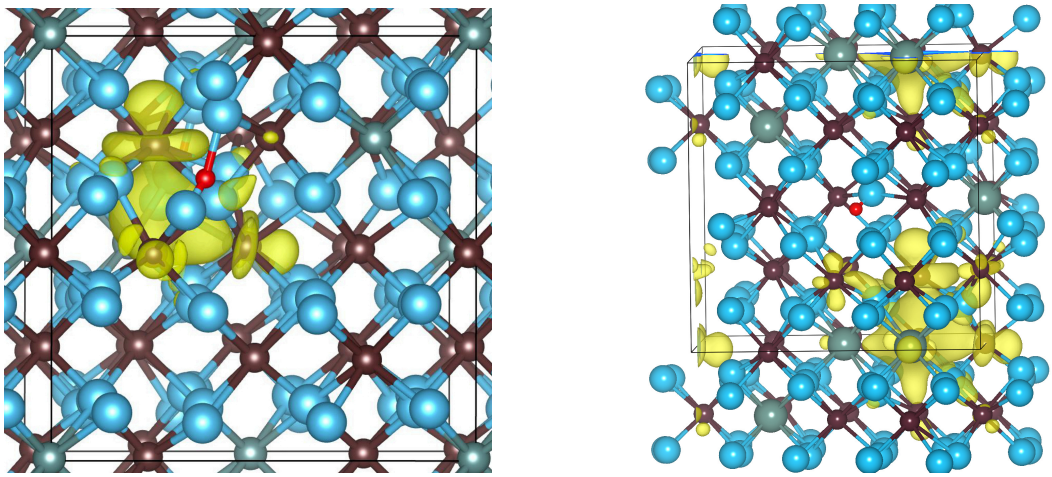

(a) *ScSZ* **(b)** *YSZ*

Figure 3.3: *a) Atomistic structure of a neutral oxygen-bound hydrogen configuration in ScSZ obtained from the hybrid (HSE06) calculations. The spin-density isosurface reveals the localization of the excess electron is shown in yellow.*
b) Electron-density isosurface (in yellow) for the defect state of the neutral bond-type hydrogen configuration. The plot depicts the cubic supercell and the charge isosurface for the occupied defect-induced level in the gap. The results were obtained from the hybrid (HSE06) calculations.[15]
The chemical elements are represented as follows:H(small red sphere in the middle),Zr (smaller dark-brown spheres), O (larger blue spheres), Sc (large light-grey spheres) in a) and Y (very large light-gray spheres) in b).

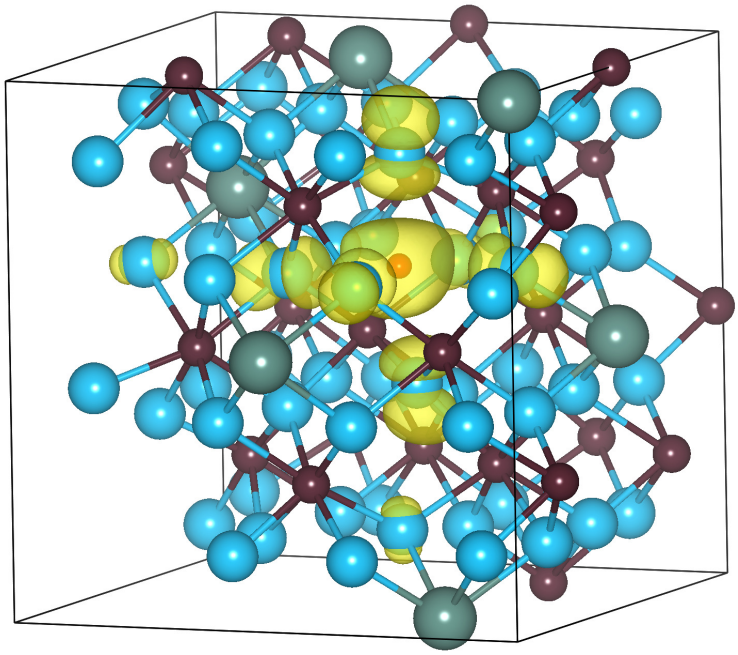

Figure 3.4: *Electron-density isosurface (in yellow) for the defect state of the neutral interstitial hydrogen configuration in YSZ. The plot depicts the cubic supercell and the charge isosurface for the occupied defect level in the gap. The results were obtained from the hybrid (HSE06) calculations. In the case shown here hydrogen resides in the oxygen-vacancy site. The chemical elements are represented as follows:H(small red sphere in the middle),Zr (smaller dark-brown spheres), O (larger blue spheres), Y (very large light-gray spheres).[15]*

a more dominant weight on a Zr ion located at a distance of 3.9 Å to the hydrogen nucleus for the case of ScSZ and at a distance of 4 Å to the hydrogen nucleus for the case of YSZ. The isosurface profile also shows considerable weight of the excess electron in the interstitial space of the fluorite lattice. Inspection of the displacement field near the defect further showed that the excess electron polarizes locally the oxide lattice. In particular, the ZrO distances around the Zr ion which carries the largest electron density increase by as much as 0.10 Å in order to accommodate the extra electron. This is a signature of a small polaron formation induced by the presence of the hydrogen electron, which in turns becomes trapped near the hydrogen impurity

site. This outcome was confirmed by examining several other oxygen-bound H^0 higher energy geometric arrangements in different parts of the supercell. In all of them the excess electron showed similar trapping characteristics. Similarly, hydrogen was found to be an amphoteric defect exhibiting a deep-donor (atom like) behaviour in its lowest energy structure shown in Fig. 3.4 for YSZ.

The calculated hyperfine interactions values A_{iso} between hydrogen and the so called excess electron for the oxygen bound configuration were extremely small. In all calculated geometric arrangements of this configuration A_{iso} was less than 1 MHz, and even equal to zero for one of the higher energy arrangements. These findings are indicative of a vanishing (almost non existent) spin density at the site of the hydrogen nucleus. The lowest-energy neutral oxygen bound configuration in ScSZ (depicted in Fig. 3.3a), in particular, was found to possess a Fermi-contact term with a magnitude of 0.45 MHz in the DFT calculations. The same oxygen bound configuration also possessed a dipolar hyperfine constant D equal to 2.4 MHz. Other higher energy geometric arrangements of this oxygen bound configuration had however smaller values of D. These variations in the value of D suggest a dependence of the anisotropic hyperfine interaction upon the angular distribution of the spin density with respect to the hydrogen site as well as upon the distance between the hydrogen nucleus and the Zr ion which carries most of the spin density. No values of hyperfine interaction were calculated for the YSZ case but values are expected to be similar

These calculations clearly show that the oxygen bound configuration is characterized by a small value of the hyperfine interaction, dominated by the dipolar component.

In the case of the interstitial atom like configuration only calculations relative to YSZ are available. In bulk YSZ there are two hydrogen/muon interstitial atom like configurations. A cube centred configuration (cc), where the muon occupies a position in an empty cube (see Fig. 3.1), and a oxygen-vacancy configuration (V_0), where the muon occupies a structural oxygen-vacancy position (Fig. 3.4) [15]. Calculations in interstitial atom like hydrogen at the core of a high-angle grain boundary in YSZ were also made by Dr. Apostolos [17] where two different interstitial atom like configurations

are reported (Core1 and Core2). Values of the hyperfine interaction for these atom like configurations were calculated between 3682 MHz and 3349 MHz and between 3285 MHz and 2976 MHz for two different geometric configurations of the V_0 atom like configuration (in internal reports of Dr. Apostolos he stated that in his calculations the cc atom like configuration yields values of hyperfine interactions similar to those for the V_0) The atom like configurations for the grain boundary configurations in YSZ are calculated between 3361 MHz and 3018 MHz for Core1 and between 2709 MHz and 2197 MHz for Core2 (the uncertainty depends on the type of functionals and the cutoff energy used in the calculations). In each case D was non zero but no more that 25 MHz for the bulk case and no more then 35 MHz in the atom like configuration at the core of the grain boundary.

The minimum energy pathways (MEP) were also calculated by Dr. Apostolos [15], in the scope of this project, to determine the interstitial-to-bond site changes and the activation energy of these migrations for bulk YSZ. Figure 3.5 represents the overall findings of these calculations. As we can see in this figure there is a barrier of about 0.1 eV that needs to overcome for the muonium/hydrogen atom to go from the interstitial atom like position (V_0 or cc) to the oxygen bound site.

The long discussions between theoretical finding and the experimental results, that we will now present, worked hand in hand to produce a cohesive model.

3.2 Experimental details and analysis

3.2.1 Introduction

Muon-spin rotation and relaxation experiments took place at the EMU instrument of the ISIS Facility, Rutherford Appleton Laboratory, United Kingdom. Conventional transverse-field and longitudinal-field were undertaken from liquid-helium temperature up to 700 K, and the respective experimental details will now be presented.

In the experiments the following polycrystalline samples were used: an undoped monoclinic ZrO_2 sample (obtained commercially from Alfa Aesar),

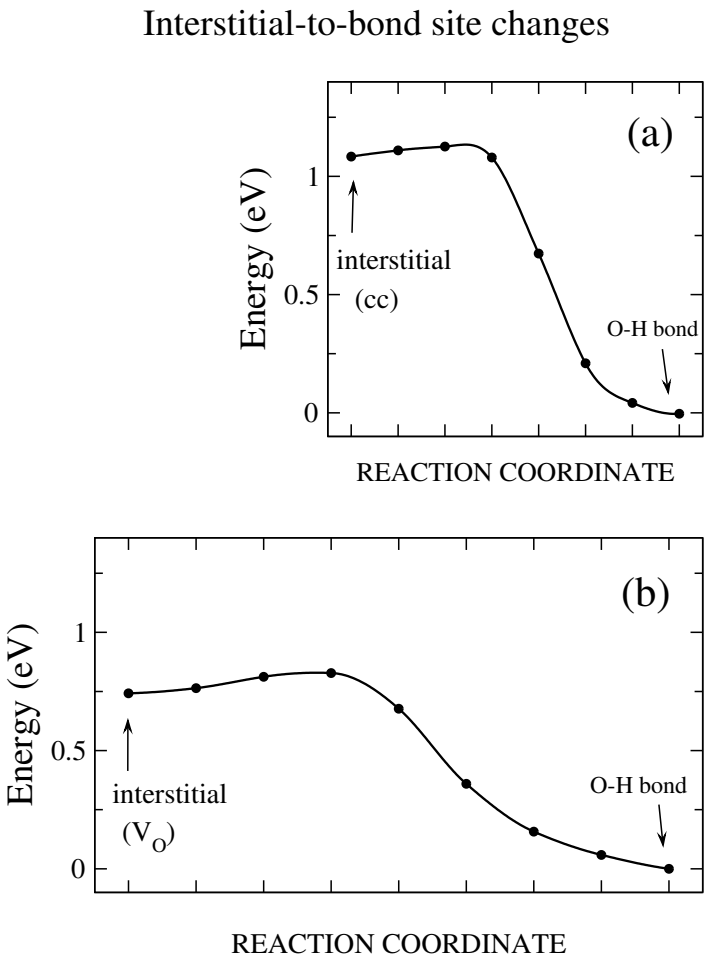

Figure 3.5: *Energy profiles along the minimum-energy paths of the site changes of* H^0*. [15]*

a scandia-stabilized ZrO_2 sample (ScSZ, obtained commercially from Sigma-Aldrich), an yttria-stabilized ZrO_2 sample (YSZ, kindly provided by INNOVNANO), a magnesia-partially-stabilized ZrO_2 sample (MgSZ, obtained commercially from Goodfellow) and two calcia-doped ZrO_2 samples (ZrO_2:Ca and CaSZ, obtained commercially from Alfa Aesar).

The crystallographic structure of the samples was verified using X-ray diffraction (XRD) at the TAIL (Trace Analysis and Imaging Laboratory) at the University of Coimbra. XRD patterns were collected over a 2θ range of $10^o - 135^o$ in steps of 0.01^o and exposition of 2 s per step using a Bruker D8 Advance diffractometer with Cu Kα radiation. The data were analyzed by the Rietveld method using the TOPAS software.[76] The results are summarized in Table 3.1. We recall that the local structures of the cubic and of the tetragonal phases are very similar and distinct from the monoclinic local structure. [75]

The samples were stored and handled in air. During the measurements, the samples were in low-pressure helium exchange gas. No significant structural change with ambient atmosphere is expected to occur for temperatures below 1000 K.

These measurements allowed us to identify and characterize the muonium / hydrogen configurations in zirconia, through low temperature ($\leq 100K$) transverse-field measurements as well as room temperature longitudinal-field measurements. An interstitial state and an oxygen bound state were identified and the missing fraction was characterized by complementary measurements in high-transverse field, performed at the TRI-University Meson Facility (TRIUMF), Canada.

A highly relevant interstitial to oxygen bound site conversion was also characterized.

3.2.2 Basic TF data

In Fig. 3.6 we present typical transverse-field time spectra obtained for the listed samples in table 3.1 and 3.2, at the lowest measured temperature summarised in table 3.3 and with an applied transverse-field B = 10 mT. We note that, despite the overall differences between the samples (doping, crystallo-

Table 3.1: *List of samples used in this work together with crystallographic details of composition verified with X-ray diffraction. Errors in phase abundance are indicated only when at least two phases were clearly identified.*

Sample Designation	Composition	Crystal Structure		
		Cubic %	Tetragonal %	Monoclinic %
ZrO_2 (undoped)	ZrO_2			100
ScSZ	$(Sc_{0.1}Zr_{0.9})O_{1.95}$	35(1)	65(1)	
YSZ	$(Y_{0.08}Zr_{0.92})O_{1.96}$	100		
MgSZ	$(Mg_{0.04}Zr_{0.96})O_{1.96}$	30.6(4)	41.7(4)	27.8(3)
ZrO_2:Ca (monoclinic)	$(Ca_{0.06}Zr_{0.94})O_{1.94}$			100
CaSZ	$(Ca_{0.06}Zr_{0.94})O_{1.94}$	81(1)		19(1)

Table 3.2: *Grain size of the crystallographic phases identified with x-ray diffraction in the ZrO_2 samples used in this work.*

Sample	Grain Size (nm)		
	Cubic	Tetragonal	Monoclinic
ZrO_2 (undoped)			79.4(5)
ScSZ	76(6)	17.9(5)	
YSZ	12.7(1)		
MgSZ	27.0(5)	34.3(6)	30.8(8)
ZrO_2:Ca (monoclinic)			48.8(7)
CaSZ	70(3)		20(2)

graphic structure, grain size, as expressed in Table 3.1), all samples show a remarkably similar behaviour, which expresses the local nature of the muon probe. A clear slightly damped oscillation at the Larmor frequency $\omega/2\pi = (\gamma_\mu/2\pi)\mathrm{B} = 1.39$ MHz is observed, corresponding to muons forming a diamagnetic component. However a fit using a single relaxing oscillation does not model correctly the low temperature time spectra. An additional component with a higher relaxation, corresponding to muons forming a paramagnetic component, is needed. However, the choice of the fitting function is far from trivial, particularly the shape of the additional relaxation.

The choice of the fitting function

The presence of the additional relaxing component was obvious from the first preliminary analysis with a single component, which yielded poor fits (either with a lorentzian or a gaussian shape). Analysis with a single component fit with a stretched exponential relaxation ($e^{(-\lambda t)^\beta}$) however yielded satisfactory χ^2 values. The β parameter, in these stretched exponential fits, was always between 0.5 and 1, a clear sign that we have a mixture of various peaks (lorentzian and or gaussian shaped). The discovery and characterization of the donor polaron state in TiO_2 (Chapter 2) led us to use the polaron model also in ZrO_2 (which, as we will detail, provides excellent results.)

Another important analysis problem is related to the interdependence of the asymmetries and relaxations (namely the relaxation of the additional component). Again, the polaron donor model presented for TiO_2 allowed us to decide a successful analysis strategy, based upon fixing the asymmetries to the lowest temperature value, as will be detailed in the next section.

We have thus fitted the data with a sum of two components:

$$\begin{aligned} A(t) = A_d e^{-\frac{1}{2}\sigma^2 t} cos(\omega t + \phi_d) + \\ + A_{p_1} e^{-\lambda_{p_1} t} cos(\omega t + \phi_{p_1}) \end{aligned} \tag{3.1}$$

where A_d and A_{p_1} are respectively the diamagnetic and paramagnetic asymmetries, σ is the gaussian diamagnetic relaxation, λ_{p_1} is the lorentzian paramagnetic relaxation, ϕ_d and ϕ_{p_1} are respectively the diamagnetic and paramagnetic phases.

For the MgSZ and the Calcia doped samples (CaSZ and monoclinic ZrO_2:Ca), an additional paramagnetic relaxing component with a relaxation of about 10 times higher is present. This relaxation presents a clear lorentzian shape. These data were thus fitted with a sum of three components:

$$\begin{aligned} A(t) = & A_d e^{-\frac{1}{2}\sigma^2 t} cos(\omega t + \phi_d) + \\ & + A_{p_1} e^{-\lambda_{p_1} t} cos(\omega t + \phi_{p_1}) \\ & + A_{p_2} e^{-\lambda_{p_2} t} cos(\omega t + \phi_{p_2}) \end{aligned} \tag{3.2}$$

where the subscript p_1 and p_2 denote the slower and faster relaxing paramagnetic component respectively.

Data analysis were completed with the WiMDA program. [77] A room temperature calibration with a silver sample at B = 10 mT allowed to extract the maximum instrumental asymmetry A_{max} and therefore to measure the fraction of muons thermalizing at each configuration.

The final fitting function was thus chosen according to the following criteria:

- The diamagnetic fraction relaxation is attibuted to nuclear broadening (Van Vleck relaxation) which is well known to be modelled using a gaussian relaxation (σ) shape as shown in Ref. [28, 78].
- The additional paramagnetic component was modelled with a lorentzian shape similarly to the pedestal seen in Ref. [79, 80] where the shallow muonium lines are too broad and/or have a too small amplitude to be clearly defined (this will be discussed in detail in the next section).

3.3 Discussion

The temperature dependence of the paramagnetic relaxation λ_{p_1} for most of our samples is presented in Fig. 3.7. We note that no CaSZ sample plot is shown because in that temperature range we only have five data points, however they are consistent with the trend of ZrO_2:Ca. At the lowest temperatures, this relaxation is about one order of magnitude higher than the

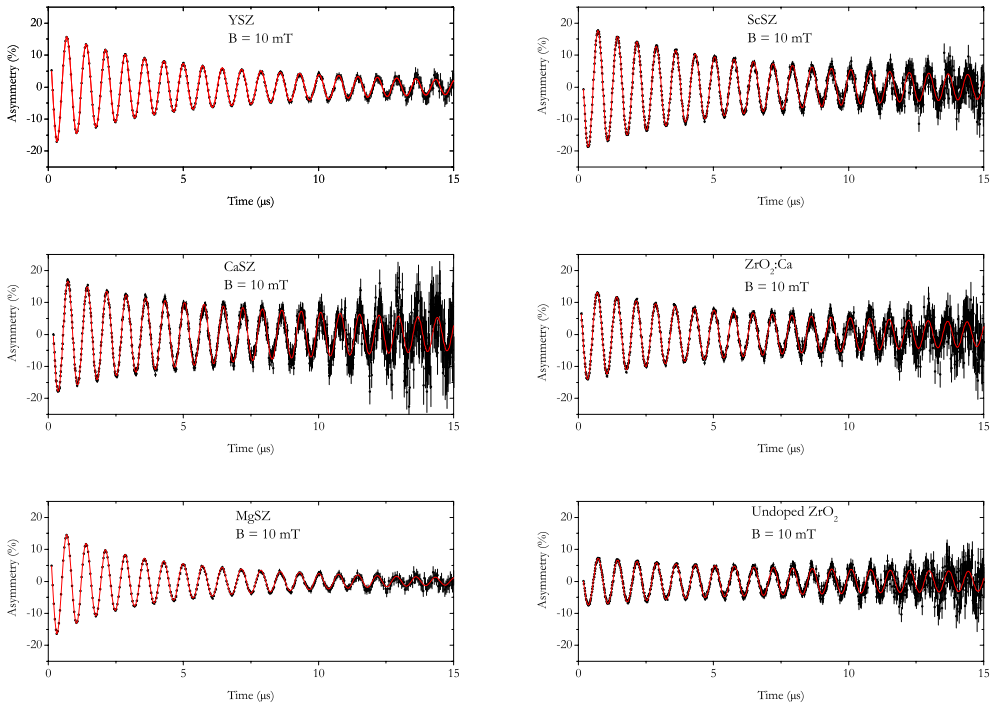

Figure 3.6: *Muon spin asymmetry as a function of time, in transverse geometry ($B = 10$ mT), at low temperatures (Table 3.3). The maximum instrumental asymmetry is indicated (horizontal dashed lines), showing the existence of an unobserved fraction of muon spin polarization (missing fraction). A rapidly decaying component is prominent in the first 6 μs, superimposed to a slowly relaxing component dominant for higher times.*

diamagnetic relaxation σ and thus easily distinguishable. However, λ_{p_1} decreases as temperature increases up to room temperature, making the separation increasingly difficult as the two relaxations become similar. Above c. 100 K it is no longer possible to separate the two relaxing components in the fits and a single relaxing component was used in the analysis. As shown in Fig. 3.7, the relaxation gradually approaches a value which is consistent with the Van Vleck relaxation due to dipolar nuclear broadening. In the temperature range $7 - 100$ K, the diamagnetic relaxation is expected to be fairly constant, any effects due to possible motional narrowing being negligible. Preliminary analysis revealed that the asymmetries A_d and A_{p_1} are constant within the above-mentioned temperature range; this is also consistent with the polaron model presented below. For temperatures below 100 K and for each sample, we have thus fixed the asymmetries A_d and A_{p_1} at the lowest temperature value, as well as the diamagnetic relaxation at $\sigma = 0.03\ \mu s^{-1}$.

In Table 3.3 we summarize the results of this analysis: we indicate the fractions f_d, f_{p_1} and f_{p_2} of muons thermalizing in each configuration, as well as the fraction of muon spin polarization which is not observed (missing fraction) f_{miss}. As will be discussed in detail below, we assign the diamagnetic and paramagnetic p_1 component to the oxygen-bound configuration (described section 3.1.3). However the diamagnetic site has a Zr^{4+} ion neighbour and the paramagnetic p_1 site has a Zr^{3+} polaron neighbour. The missing fraction likely corresponds to muons thermalizing at the interstitial configurations, and its recovery and dynamics can be analysed by means of the repolarization curve and of the behaviour of the additional relaxing component.

3.3.1 Oxygen Bound State

We will now discuss the assignment of the diamagnetic fraction f_d and of the slowly-relaxing paramagnetic fraction f_{p_1} to muons thermalizing at the oxygen bound configuration.

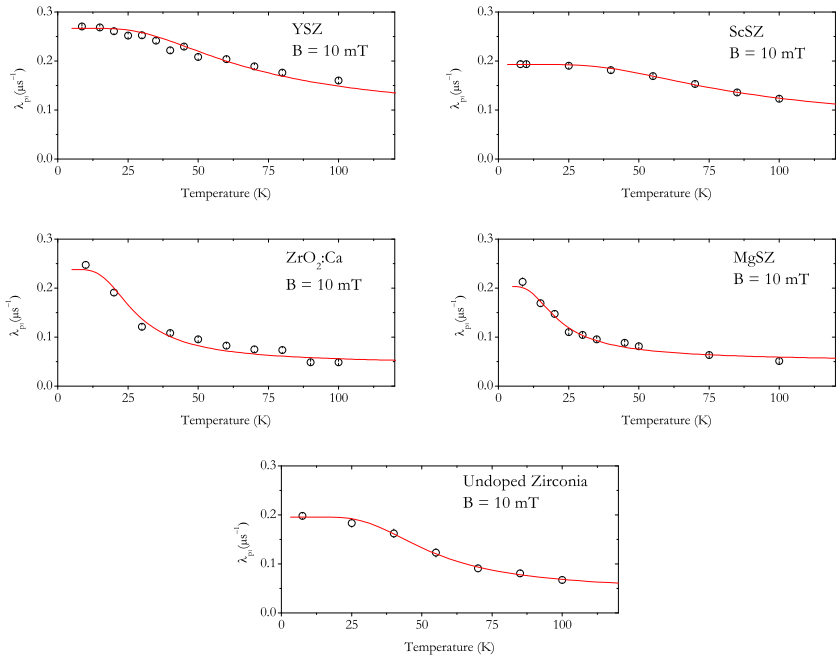

Figure 3.7: *Temperature dependence of the slowly-relaxing paramagnetic relaxation λ_{p1}. The line is a fit as detailed in the text.*

Diamagnetic State

As mentioned already, the diamagnetic fraction has a very small relaxation consistent with that expected from dipolar nuclear broadening (Van Vleck relaxation). This fraction most likely corresponds to muons thermalizing as Mu^+ at the oxygen bound configuration, according to the theoretical predictions of section 3.1.3. As usual in μSR experiments, it is not possible to distinguish directly Mu^+ from the negatively charged diamagnetic configuration Mu^-, but the fact that Mu^- requires the capture of two electrons during the thermalization process of the muon makes it always a far more improbable process.

Table 3.3: *Fitted fractions and relaxations for the different samples at the indicated temperatures. The applied transverse field is 10 mT. The diamagnetic relaxation was fixed to $\sigma = 0.03\ \mu s^{-1}$ to all samples. The indicated errors represent the statistical errors obtained directly from fitting. As discussed in the text, the systematical errors are higher.*

Sample	T (K)	f_d (%)	f_{p_1} (%)	f_{p_2} (%)	f_{miss} (%)	λ_{p_1} (μs^{-1})	λ_{p_2} (μs^{-1})
ZrO_2 (undoped)	7.8	16(1)	21(1)		63(2)	0.20(2)	
ScSZ	7.8	16(1)	79(2)		5(2)	0.19(1)	
YSZ	8.6	15.2(3)	67.3(2)		17.5(4)	0.270(2)	
MgSZ	9.4	16(2)	69(1)	8(2)	7(3)	0.21(1)	1.3(5)
ZrO_2:Ca (monoclinic)	9	18(2)	51(1)	7(2)	24(3)	0.18(1)	1.0(5)
CaSZ (cubic)	10	27(2)	56(2)	7	10(3)	0.20(1)	1.0

Paramagnetic state (p_1)

As for the slowly-relaxing paramagnetic component f_{p_1} it corresponds to muons in the presence of a non-zero hyperfine interaction. However, the fact that this hyperfine interaction is too small prevents the clear observation of its distinctive powder-pattern spectrum,[81] which is here collapsed over the diamagnetic line and manifests itself as an additional broadening. [28, 82] An upper bound for the hyperfine interaction can nevertheless be estimated.

In Fig. 3.8 we present a Fourier transform of a high statistics spectrum obtained for YSZ at 8.5 K. This Fourier spectrum was obtained using the Lomb method[83] and the level of probability of false alarm below 0.0001 is shown as a pointed line. From the similar case of TiO_2 we know that the hyperfine interaction is mainly dipolar.[13, 8] We may immediately estimate its approximate value from the full width at half maximum of the line, yielding $D \approx \lambda/\pi = 0.11$ MHz. A closer inspection to Fig. 3.8 reveals the existence of a small spectral power above the threshold for false alarm, at $f_1 \approx 1.3$ MHz and at $f_2 \approx 1.5$ MHz. These are easily attributable to the known ringing

effects in Fourier analysis, but may also correspond to the expected steps of a powder-pattern hyperfine spectrum [81]. This powder pattern is calculated using the function used by H. V. Alberto et al. [81] that relates the fourier power ($f(\nu)$) and the frequency (ν):

$$f(\nu) = \frac{dP}{d\nu} = \frac{dP}{d\theta}\frac{d\theta}{d\nu} = \sqrt{\frac{3D}{2}}\sqrt{2\left(|\nu-\nu_0| - \frac{A_{iso}}{2}\right) + \frac{D}{2}} \quad \text{for } \nu_0 - \frac{A_\parallel}{2} \leqslant \nu \leqslant \nu_0 - \frac{A_\perp}{2} \quad \text{and } \nu_0 + \frac{A_\perp}{2} \leqslant \nu \leqslant \nu_0 + \frac{A_\parallel}{2} \tag{3.3}$$

where ν_0 is the center of the distribution, $A_\parallel = A_{iso} + D$ and $A_\perp = A_{iso} - \frac{1}{2}D$. The powder pattern represented as a red dashed line in Fig. 3.8 is a simulation using a value of $A_{iso} = 0$ and a value D corresponding approximately to $D \approx f_2 - f_1 = 0.2$ MHz. Both approaches allow to conclude that the hyperfine interaction responsible for λ_{p1} is of almost pure dipolar origin ($A_{iso} \approx 0$) with a dipolar term $D \approx 0.1$ MHz (at most 0.2 MHz) for YSZ. The estimated values for D in the samples studied in this work range from the highest value found for YSZ, $D \approx 0.11$ MHz, to the lowest value $D \approx 0.04$ MHz for CaSZ, the span likely arising from the small differences in the lattice relaxation around the muon oxygen bound configuration and the corresponding different distances of the Zr cations.

The nature of this hyperfine interaction can be understood from the theoretically predicted configuration for the neutral oxygen bound state, as shown in Fig. 3.3a. There it is predicted that the electron associated to the neutral oxygen bound configuration is in fact not centered at the muon, but instead forms a polaronic state with the electron density localized asymmetrically at nearby Zr^{4+} ions, with an extremely small hyperfine interaction dominated by the dipolar component. A careful inspection of Fig. 3.3a and the corresponding calculations reveals that the electron is spread over three Zr^{4+} ions, although with a dominant weight to one of them, the latter could then be considered to be reduced to Zr^{3+} to a good approximation. Such a geometrical arrangement can lead to a large compensation of the dipolar part from different regions of the electron distribution. This polaronic state has been proposed for cubic-stabilized zirconia both in EPR measurements [84, 85]

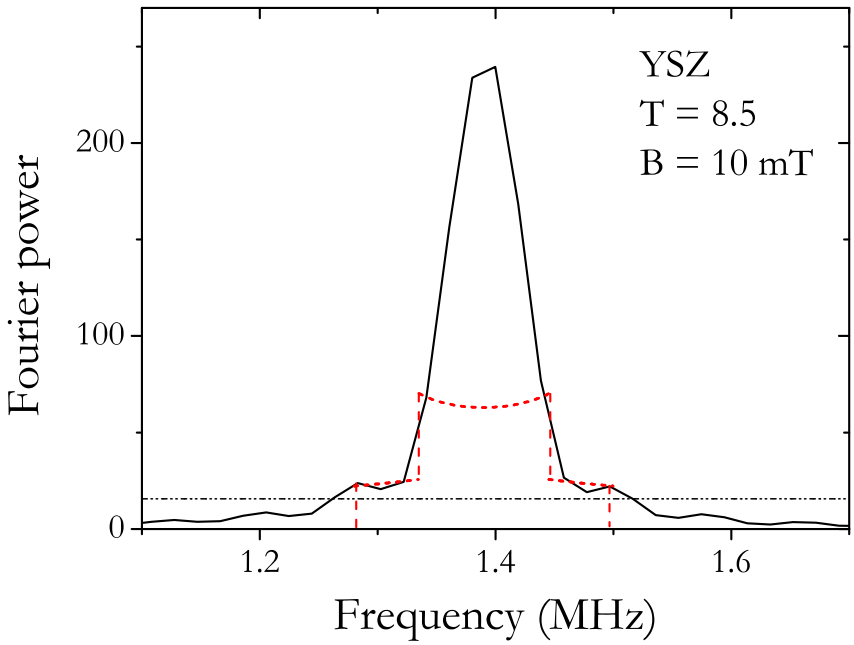

Figure 3.8: *μSR Fourier spectrum of YSZ at $T = 8.5$ K in an external magnetic field of $B = 10$ mT. The red dashed line is a simulation of a powder spectrum with $A_{iso} = 0$ MHz and $D = 0.2$ MHz, as discussed in the text.*

and in *ab-initio* calculations [15]. These polaronic centres can also be created when samples are irradiated with UV light or X-rays or subject to treatment in hydrogen atmosphere.[86] As we have described in chapter 2, such a polaronic state is also present in TiO_2, a system similar to ZrO_2 [13, 87, 8]. The difference between the experimental value of the hyperfine interaction and the predicted computational value for the lowest-energy neutral oxygen-bound configuration is probably an indication that the lattice does not reach its full relaxed configuration around the muon during the time of the experiment (about 15 μs, see Fig. 3.6). The observed differences in λ_{p_1} for the different samples (Table 3.3) are likely due either to small differences in the distances between the hydrogen/muon neutral oxygen bound position and the nearby zirconium atoms or to changes in the electron density function.

3.3.2 Temperature dependence of the paramagnetic relaxation

We now address the temperature dependence of the slow paramagnetic component λ_{p_1}, shown in Fig. 3.7. We have extracted the activation energy of this mechanism by fitting the data in Fig.3.7 with a Boltzmann like function:

$$\lambda_{p_1}(T) = \frac{1}{1 + N exp(-E_a/k_B T)} \tag{3.4}$$

where E_a is the activation energy of the process, k_B is the Boltzmann constant, and the empirical parameter N relates to the shape of the binding potential. We fixed (after an initial fit with free parameters) the weight factor to $N = 18(3)$ for the monoclinic samples (undoped ZrO_2 and ZrO_2:Ca) and $N = 4(1)$ for the cubic/tetragonal samples (ScSZ and YSZ); an intermediate value of $N = 9(2)$ is found for the mixed MgSZ sample. The results for the activation energies obtained using this analysis are summarised in Table 3.4 for all samples except cubic CaSZ. For this sample the little existent data do not allow this analysis, but are overlapping with the data of monoclinic ZrO_2:Ca and consistent with the corresponding activation energy.

A decrease of λ_{p1} with temperature can be attributed to a number of phenomena such as ionization of the polaron, spin fluctuations, motional narrowing due to movement of the muon or different muon-polaron distances due to differences in the electron thermalization.

Of these four models, two seem unlikely: the ionization of the Zr^{3+} polaron does not seem possible if we take into account that EPR data reveal that the corresponding activation energy is at least 0.1 eV for reduced samples [88] which is much higher then what we get (Table 3.4). Motional narrowing due to movement of the muon (as in TiO_2) is also unlikely to occur, because the onset of muon motion between near equivalent hydrogen/muon sites, calculated by Dawson *et al.*, [89] requires activation energies much higher (about 0.4 meV) then those indicated in Table 3.4.

Spin fluctuating model

In this model λ_{p_1} has two contributions, one part λ_e is due to the nearby electron, and the other $\lambda_{nuclear}$ is due to the magnetic field distribution caused by the surrounding nuclear moments, so $\lambda_{p_1} = \lambda_e - \lambda_{nuclear}$. For these very small relaxations is approximately equal to the diamagnetic relaxation σ. The decrease with temperature can be attributed to line narrowing due to electron spin fluctuations [90]. In this model an estimate of the spin-lattice relaxation time T_1 [91, 92] can be estimated using the expression:

$$T_1 = \frac{1}{2\lambda_e} \tag{3.5}$$

We obtain T_1-values in the order of 1 μs at 100 K. As far as we know, the value of T_1 for the corresponding T center observed in EPR measurements has not been measured and only T_1 values for the F center (electron trapped in an oxygen vacancy) are known ($T_1 = 7\mu$s at T=100 K) [93]. In this model the activation energies presented in Table 3.4 will correspond to the energy needed to start these spin fluctuations.

Electron thermalization model

As a final alternative, we consider this process in relation to the formation process of this configuration: the mean distance between the polaron and the muon is bound to increase with temperature, meaning that the electron that comes with the muon and creates the polaron can "thermalize" at longer distances from the muon position. In this model, that we consider the most likely, the extracted activation energies in Table 3.4 are identified with the binding energy of the muon to the electron. The observed differences in the fractions shown in Table 3.3 are probably due to changes in the formation probabilities due to the different crystal structures and to the different cation dopants which likely change the crystal lattice vibrations and therefore affect the final thermalization stages. [94] The same factors affect as well the binding energies shown in Table 3.4.

Table 3.4: *Activation energies associated to the decrease of the paramagnetic relaxation λ_{p_1} with temperature.*

Sample	Activation Energy (meV)
ZrO_2 (undoped)	15(1)
ScSZ	15(1)
YSZ	12(1)
MgSZ	5(1)
ZrO_2:Ca (monoclinic)	7(1)

3.3.3 Atom-like Interstitial State

Longitudinal Field Study

A notable feature shown in table 3.3 is the fact that a significant part of the muon spin polarization is not observed at low temperatures (missing fraction, f_{miss}). As noted above, the fractions (and also the missing fraction) do not vary visibly up to 150 K. The missing fraction is related to muons depolarizing rapidly during the thermalization stage, due to the formation of deeply bound muonium. We thus assign the missing fraction to muons thermalizing in the interstitial configurations discussed in section 3.1.3 (either the pure interstitial or the oxygen-vacancy site). The hyperfine interaction associated to these configurations can be nevertheless characterised by means of the longitudinal-field repolarization technique discussed in chapter 1

We note that the repolarization curve of undoped monoclinic zirconia has already been published in reference [11] and is consistent with a vacuum-like state. We have now performed repolarization studies for ZrO_2:Ca (monoclinic) and YSZ only (figures 3.9 and 3.10, respectively), which show remarkable differences. The repolarization curve for ZrO_2:Ca shown in Fig. 3.9 presents the monotonic increase characteristic of a deep isotropic state. The curve in Fig. 3.9 is a fit with the usual isotropic repolarization curve,[28, 95] yielding a hyperfine parameter $A_{iso} = 3.02(8)$ GHz, characteristic of a deep compact state. However, the repolarization curve for YSZ presented in Fig. 3.10 is two-stepped, which is a usual sign of anisotropy.[96] We have thus fitted the data in Fig. 3.10 with the phenomenological repolarization functions proposed by Pratt in ref. [96] and obtained $A_{iso} = 2.1(2)$ GHz and

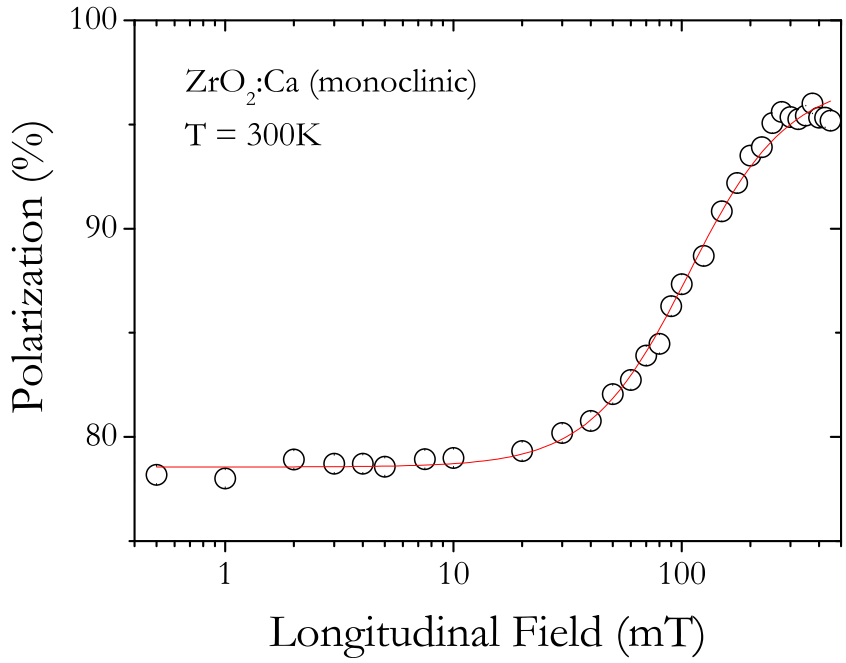

Figure 3.9: *Repolarization curve for ZrO_2:Ca (monoclinic) at $T = 300$ K. The red line is a fit assuming an isotropic hyperfine interaction $A = 3.02(8)$ GHz.*

$D = 0.13(2)$ GHz. The corresponding fit is shown as a red line in Fig. 3.10. Alternatively, the repolarization curve in Fig. 3.10 can be fitted to a combination of two isotropic states with $A_{iso1} = 1.9(1)$ GHz $A_{iso2} = 0.11(1)$ GHz.

The remarkable differences in the repolarization curves shown in Figs. 3.9 and 3.10 may be due to a combination of factors. As discussed in section 3.1.3, in bulk YSZ an atom-like configuration may stabilize at either the oxygen vacancy (V_0) or at a cube center interstitial site (cc) [15]. It is therefore a possibility that the different repolarization curves correspond to these two structurally different interstitial sites.

However, we note that the ZrO_2:Ca sample corresponding to the repolarization curve in fig. 3.9 is purely monoclinic, whereas the YSZ sample corresponding to the repolarization curve in fig. 3.10 is purely cubic. The hyperfine interactions associated to the repolarization curves in Figs. 3.9 and 3.10 could therefore both correspond to neutral muonium in the cube center interstitial site, the differences in the hyperfine interactions arising from

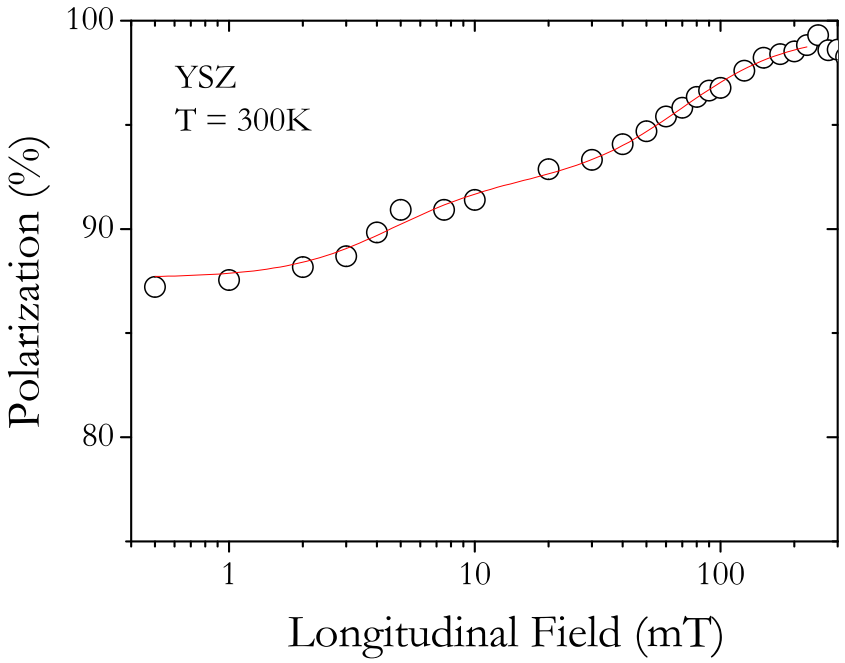

Figure 3.10: *Repolarization curve for YSZ at $T = 300$ K. The red line is a fit assuming an axially symmetric anisotropic hyperfine interaction with $A_{iso} = 2.1(1)$ GHz and $D = 0.13(2)$ GHz.*

the different local electronic structure of the cube center associated to the different crystallographic structure. However, the hyperfine interaction for interstitial hydrogen in cubic bulk YSZ, as referred in section 3.1.3, has been calculated in Ref. [17] to be essentially isotropic with $A_{iso} \approx 3$ GHz. This value is much larger than our experimental value of $A_{iso} = 2.1(1)$ GHz for YSZ, but is remarkably close to our experimental value $A_{iso} = 3.02(8)$ GHz for ZrO_2:Ca. The comparison of the experimental and of the *ab-initio* values, together with the assumption that the muon is sensitive at a local level, suggests that the calculated isotropic state is being observed in ZrO_2:Ca but not in YSZ.

As mentioned, the two-stepped recovery (Fig. 3.10) could in principle be due to hyperfine interactions of muons at different sites. However, the smaller of the two interactions ($A_{iso2} = 0.11(1)$ GHz) corresponds neither to a value expected for the interstitial site nor to a value expected for the

bound configuration. Therefore, the more likely interpretation can be proposed taking in to account the grain sizes shown in Table 3.1 (13 nm for YSZ and 49 nm for ZrO_2:Ca). The grain sizes in YSZ are much smaller, making the role of the grain surface much more important. In muon spectroscopy experiments in nanocrystalline II-VI semiconductors strong evidence of formation of surface states was found.[97] The segregation of impurities to the surface of nanograins is a well known effect [98] and is also known to be enhanced with decreasing grain size. [99]. Moreover, as said in section 3.1.3, first-principles calculations showed that hydrogen at the grain boundary core was characterized by different A_{iso} values from those of hydrogen in the bulk regions, and in certain cases with corresponding magnitude smaller by as much as 20 %. This finding was attributed to the distinct interface structure of the grain boundary which could allow (for certain cases) a much larger spilling of the valence electron density to neighboring ions, thus,leading to a reduction of the spin density at the hydrogen nucleus and, consequently, a smaller A_{iso} value for hydrogen at the grain boundary core. This reduction of the hyperfine interaction at the YSZ grain boundary leads to values as low as $A_{iso} \approx 2.3$ GHz (after scaling taking into account the 3.183 factor of the magnetic moment ratio of the muon and the proton), which compare well with our experimental value. It looks therefore probable that the anisotropic component seen in Fig. 3.10 corresponds to muonium influenced by the surface of the grains.

A final note with respect to the second relaxing paramagnetic component observed in MgSZ, CaSZ and ZrO_2:Ca (monoclinic). As shown in Table 3.3, we observed this relaxation in these samples only, with values of the order of $1\,\mu s^{-1}$. We note that once more we have little available data for the CaSZ sample: as indicated in Table 3.3, we have thus fixed the relaxations λ_{p_1} and λ_{p_2} of the corresponding paramagnetic components equal to the values found for the monoclinic ZrO_2:Ca sample. We have investigated this second relaxing paramagnetic component through muon spin rotation experiments at high-transverse field (up to 7 T) performed using the HiTime instrument of the M15 beamline at TRIUMF.

High TF study

The high-transverse field experiments were performed on the undoped ZrO_2 sample and also on a high-purity powder sample of monoclinic HfO_2, obtained commercially from Alfa-Aesar. The importance of the study of monoclinic HfO_2 in conjunction with undoped ZrO_2 other than the fact that these are oxides with the same structure and the transition metal in the oxide is from the chemical same group (Group IV), is that HfO_2 is one of the most common defect in all high purity ZrO_2 (according to all our samples). Data analysis of this high-transverse field spectra was done using the WiMDA program [77]. The data reveal the presence of two components precessing at the diamagnetic Larmor frequency ω_L, with very different relaxations.

The data were therefore fitted with two relaxing components, according to:

$$A(t) = f_{p2}e^{-\lambda_{p2}t}\cos\left(\omega_L t + \phi_{p2}\right) + f_{slow}e^{-\lambda_{slow}t}\cos\left(\omega_L t + \phi_{slow}\right) \qquad (3.6)$$

The relaxation were chosen lorentzian because it gave the best fit quality and is also the expected relaxation type if we take into account the model that we will present to explain the data.

We present in Figures 3.11(a) and 3.11(c) the first 50 ns of the time spectra obtained at $T = 2$ K, for $B = 2\,\mathrm{T}$. In Figures 3.11(b) and 3.11(d) we show the same spectrum after removal of the slowly relaxing component, fitted as described above. Calibration experiments at room temperature were done with a silver sample in order to extract the maximum instrumental muon spin polarization, as well as the phase of the calibration signal.

The analysis of the slow component was first performed in the time interval $0.3 - 2.89\,\mu$s and the corresponding parameters were henceforth fixed and used in the two component analysis in the interval $0 - 0.3\,\mu$s. In the final fits, the relaxation λ_{p2} of the fast component was fixed to the low-temperature ($T = 2$ K) value. Table 3.5 summarizes the fitting results for the lowest temperature ($T = 2$ K).

We present in Fig. 3.12 the temperature dependence of the fraction of the muon spin polarization corresponding to each configuration, for HfO_2 and for ZrO_2, after normalizing to the maximum instrumental asymmetry obtained

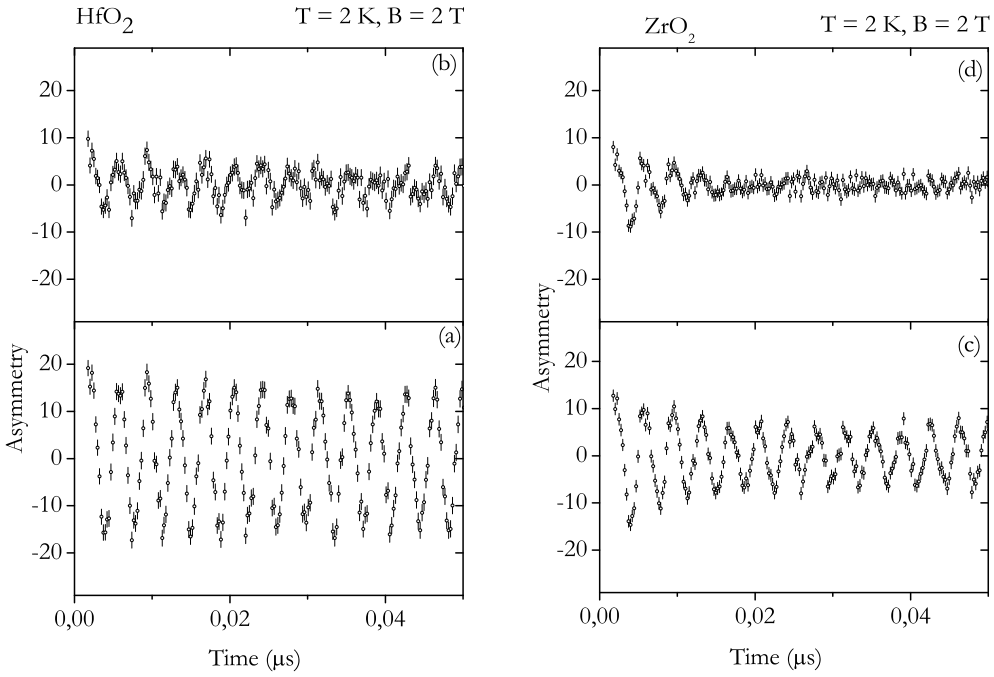

Figure 3.11: *Time spectra at 2T (detail of first channels showing the fast relaxation) for HfO_2 (left) and ZrO_2 (right) at T = 2 K and for transverse magnetic field B = 2 T. The full time spectra are shown in (a) and (c). In (b) and (d) only the fast component is shown, as discussed in the text.*

Table 3.5: *Low-temperature (2 K) fit parameters, as discussed in the text.*

	$\lambda_{slow}(\mu s^{-1})$	$\lambda_{p2}(\mu s^{-1})$	ϕ_{slow} (deg)	$\phi_{p2}(deg)$	$f_{slow}(\%)$	$f_{p2}(\%)$	missing fraction (%)
ZrO_2	0.272(7)	101(8)	152.6(5)	153(2)	25.8(3)	43(3)	31(3)
HfO_2	0.220(4)	11.1(7)	151.8(3)	152(2)	54.9(4)	20.9(9)	24(1)

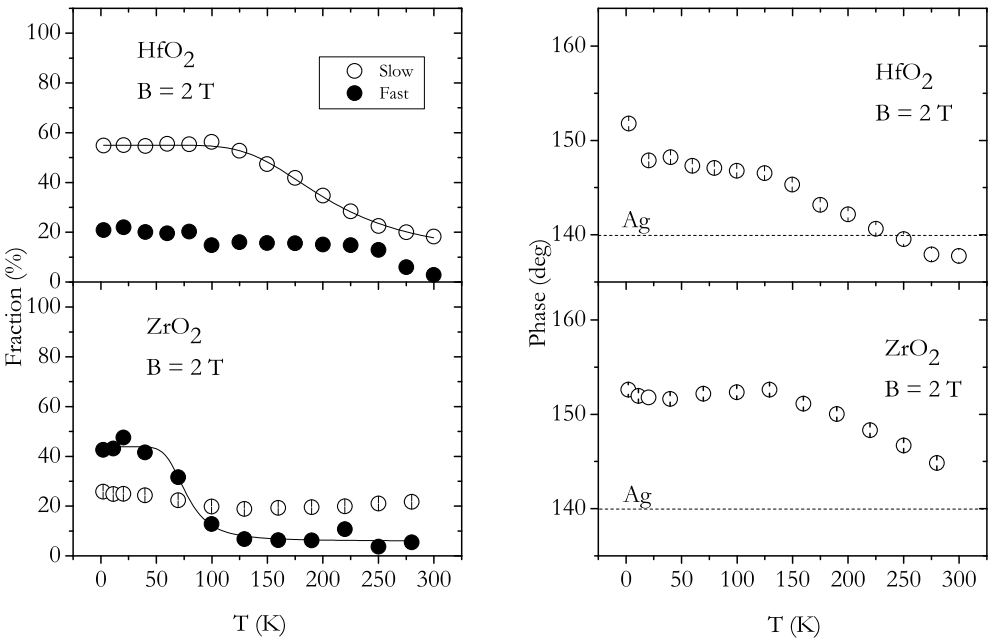

Figure 3.12: *On the left is represented the temperature dependence of the fraction f_{slow} and f_{fast}, for ZrO_2 and HfO_2, for a transverse field $B = 2$ T. The lines are fits using a Botzmann model as described in the text. On the right we represent the temperature dependence of the phase ϕ_{slow} of the slowly relaxing component, for ZrO_2 and HfO_2, for a transverse field $B = 2$ T. The dashed line indicates the value obtained for the silver calibration measurement.*

with the silver calibration. The corresponding temperature dependence of the phase ϕ_{slow} of the slow component is shown in Fig. 3.12. The dashed line in Fig. 3.12 represents the value $\phi_{Ag} = 140(1)$ deg obtained for the phase of the calibration measurement with silver at room temperature.

The low event count of these high-transverse field spectra with respect to the low-transverse field spectra and the presence of the fast component λ_{p_2}, make the separation of the σ and λ_{p_1} relaxations impossible. These two components both correspond to muons thermalizing in the oxygen-bound configuration and were then analysed jointly in a single-component lorentzian-shape relaxation (much similar to λ_{p_1}) that we will call λ_{slow}. This configuration

was already discussed in section 3.3.1. However, at these fields there is an observed phase-shift (Fig. 3.12) of this slow relaxing component that indicates that this state results from the conversion of a previous (unobserved) state. As mentioned already, previous longitudinal-field repolarization measurements in both monoclinic ZrO_2 and HfO_2 reveal the formation of a deep muonium state at room temperature [11]. The slowly relaxing diamagnetic component is thus likely to arise from delayed formation of a precursor deep muonium state, as observed in other semiconductors [91, 92].

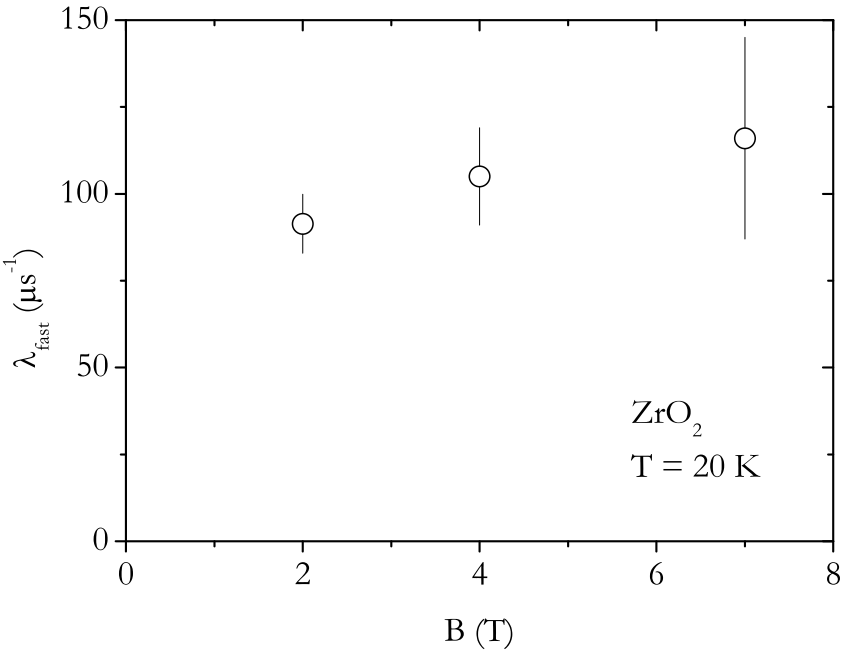

Figure 3.13: *Field dependence of the relaxation λ_{p2} of the fastly relaxing component in ZrO_2, in the transverse geometry, for a temperature $T = 20$ K.*

The precursor muonium state is likely to sit at an interstial position. However, at the lowest temperatures, the lattice has unsufficient time to relax around the impurity and the neutral precursor muonium at the interstitial position thus corresponds to a metastable interstitial configuration [91, 92, 100]. From this metastable interstitial configuration, the muon can quickly convert to the oxygen-bonded position, Mu_{Ob}.

The alternative conversion of the metastable interstitial configuration to its true minimum at an interstitial site does not appear to dominate at the lowest temperatures. This process leads to the formation of the missing fraction, where the stable interstitial state is strongly dephased due to line broadening in the conversion process. However, the temperature dependence of the slow component and of the missing fraction suggest that temperature increases the conversion rate of the metastable interstitial configuration to its true minimum. This process thus becomes a more competitive alternative to the conversion to the oxygen-bonded configuration. This is also evidenced by the temperature dependence of the phases in Fig. 3.12, where a strong phase-shift of the slow component is observed for the lowest temperatures, which gradually approaches the value obtained for the silver calibration as the temperature increases, suggesting a suppression of the process responsible for the phase-shift.

In the stable interstitial configuration, the barrier for the conversion to the oxygen-bonded site is larger. The final fraction of muons ending in the slowly relaxing diamagnetic component therefore decreases as temperature increases, with a corresponding increase of the missing fraction.

We propose that this increase with temperature of the competing formation of the true interstitial configuration is mediated by optical phonons in these ionic compounds. When these modes are activated, the formation process of the true interstitial configuration is enhanced. We have thus modelled the decrease of the slow component with a phenomenological Boltzmann-like functional dependence [11, 12, 16]:

$$f_{slow} = \frac{f^0_{slow}}{1 + N \exp\left(-E_a/k_B T\right)} \tag{3.7}$$

where E_a is the activation energy, k_B the Boltzmann constant and f^0_{slow} is the low temperature value of the slowly relaxing fraction. N is a parameter associated to the effective density of phonon modes.

The lines in fig 3.12 are fits with this phenomenological Boltzmann-like dependence. We get an activation energy of 79(7) meV for the decrease of the slow fraction in HfO_2 above 100 K. We note that the phonon modes in monoclinic HfO_2 are calculated in the range $10 - 100$ meV. [101] We also

note that the fraction of muons stopping at the slowly relaxing diamagnetic fraction is seen to be relatively temperature independent in ZrO_2 (Fig. 3.12), which is consistent with the much smaller value (around 10 meV) of the phonon mode with maximum density of states in monoclinic zirconia [102].

In Fig. 3.13 we show the field dependence of the fast relaxation λ_{fast} in ZrO_2, for $T = 20$ K. λ_{p2} is seen to be fairly field independent, suggesting that it corresponds to lifetime broadening associated to delayed muonium formation. We initially suggested that it corresponded to muons stopping at the interstitial position in a charged state (either Mu_I^+ or Mu_I^-) and converting to Mu_I^0, where the neutral configuration is known to be stable [5, 15]. In the Mu^+ case, the electron is captured from the radiolysis products; in the Mu^- case, the second electron is either lost to the conduction band or to the valence band (hole capture). However, as we shall refer in chapter 5, this apparently diamagnetic configuration may even correspond to a paramagnetic component with an extremely reduced hyperfine interaction.

We note that the fast component disappears as the temperature is increased (above 250 K for HfO_2; above 50 K for ZrO_2). It is not clear from the fits whether this is by line broadening or by a reduction in the fraction f_{p2} of muons stopping in this configuration. In the delayed muonium formation model, it is more likely that the fraction is reduced, so we choose to fix the fast relaxation throughout the temperature dependence.

We note that the relaxation of the fast component is almost one order of magnitude higher for ZrO_2 with respect to HfO_2. Also, the temperature stabilities of these components are very different: whereas in HfO_2 the fast component is observed up to 250 K, in ZrO_2 it disappears at about 100 K, with an activation energy of 46(13) meV (again fitting the fast fraction in Fig. 3.12 with a Boltzmann-like dependence such as that of eq. 3.7).

It is likely that the component associated to the fast fraction sits at (or close to) the same interstitial position than Mu_I^0. If the fast relaxing component corresponded to Mu^+, this would imply delayed electron capture, with an average time of 10 ns (for ZrO_2) or 100 ns (for HfO_2). This seems to be unlikely high. If the fastly relaxing fraction corresponded to Mu^-, a small fraction of the incoming muons would capture two electrons in the thermalization process (as suggested for other systems [12, 16, 103]) and

would end up in the corresponding stable position at the interstitial site.

Fig. 3.14 summarizes our tentative interpretation: muons in HfO_2 and ZrO_2 may stop at the interstitial position or at the oxygen-bonded position. The formation is however a complex process [91, 92], where a precursor muonium is involved. This precursor is likely at the interstitial position, albeit unrelaxed, and may have an electron or not. The delayed formation of neutral muonium from the charged precursor constitutes the fast component. The precursor stopping as neutral Mu may either relax to the true relaxed interstitial position (missing fraction) or tunnel to the oxygen bonded position. This latter case is progressively hindered as the former case progresses.

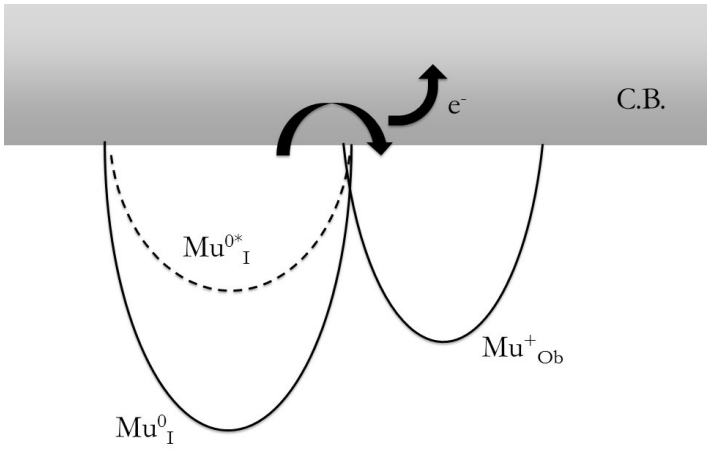

Figure 3.14: *Model for the Mu states in monoclinic ZrO_2 and HfO_2: a precursor neutral muonium state Mu_I^{0*} is formed in a metastable interstitial position. It either converts from there to the oxygen-bound configuration (corresponding to the slowly relaxing component), or to the stable interstial configuration Mu_I^0 (unobserved due to dephasing or line broadening). The fast relaxing component corresponds to muons stopping at the interstitial position in a charged state (either Mu_I^+ or Mu_I^-) and quickly converting to Mu_I^0.*

3.3.4 Interstitial to Oxygen Bound State transition

In the low transverse-field experiments, we have also addressed the temperature dependence of the YSZ, ScSZ and monoclinic ZrO_2:Ca samples, as well

as that of the undoped monoclinic ZrO_2 sample. Above 100 K muon diffusion seems to play a non-negligible role and we will address this specific point in the next section. However, a temperature effect much relevant to the current discussion of the muonium/hydrogen configurations is apparent at these higher temperatures. As shown in Fig. 3.15, the total observed fraction of muons gradually grows up to 100% at about 700 K, meaning that the missing fraction f_{miss} is gradually recovered. We recall that at above 200 K the data are adequately described by a single diamagnetic component as discussed in section 3.3. The temperature dependence of the recovery of the missing fraction is adequately described by a Boltzmann model (Eq.3.8) for all samples. The corresponding activation energies are summarised in Table 3.6.

$$f_d(T) = \frac{f_{d0} N exp(-E_a/k_B T)}{1 + N exp(-E_a/k_B T)} \tag{3.8}$$

The recovery of the missing fraction can arise due to different processes affecting the muons stopping in the neutral muonium state at the intersitial configuration. However, both the loss of the muonium electron to the conduction band ($Mu^0 \rightarrow Mu^+ + e^-_{CB}$) or the capture of an electron from the valence band ($Mu^0 + e^-_{VB} \rightarrow Mu^-$) seem unlikely: the corresponding calculated energies (c. 5 eV and 1.35 eV, respectively) are much higher than those measured (Table 3.6). The capture of the electron released by the polaron in its ionization ($Mu^0 + e^-_{polaron} \rightarrow Mu^-$) also seems unlikely, since Mu^- is likely to be thermally unstable at these high temperatures, which is not consistent with the near absence of relaxation of the observed diamagnetic component. The most likely interpretation for the recovery of the missing fraction shown in Fig. 3.15 is hence that an alteration of the formation probabilities of the interstitial configuration and of the oxygen bound configuration occurs, in favour of the latter. This interpretation is supported the MEP calculations for YSZ by Dr. Apostolos Marinopoulos presented in the subsection 3.1.3, where a very small energy barrier (0.1 eV) was determined for hydrogen to transform from the interstitial to its lower-energy oxygen-bound configuration shown in Fig. 3.5 [15]. This calculated value is consistent with the experimental values reported in Table 3.6. Interestingly, the experimental

values for the monoclinic samples (undoped ZrO_2 and ZrO_2:Ca) are about twice the values of the cubic samples, probably reflecting the fact that the vibration modes with higher oscillator strenghts occur at higher energies for the monoclinic lattice than for the cubic lattice.[75] A vibrational level 0.1 eV above the fundamental was already sugested for the interpretation of EPR data in cubic YSZ.[88] As we have just seen in the analysis of the high-TF data in monoclinic ZrO_2 and HfO_2, vibrations seem to play a very relevant role in the formation of Mu.[94]

In monoclinic undoped ZrO_2 we possibly have a hint of one of the ionization process presented. In that sample for temperatures over 400 K a new fast relaxing component is visible that we have fitted adding and additional lorentzian-shape relaxation λ_{p_3} to the fitting function.

$$A(t) = f_{slow} e^{-\lambda_{slow} t} \cos(\omega_L t + \phi_{slow}) + f_{p_3} e^{-\lambda_{p_3} t} \cos(\omega_L t + \phi_{p_3}) \tag{3.9}$$

This additional relaxation (λ_{p_3}) increases with temperature as the diamagnetic fraction f_{slow} stays constant at 52.7(2)%. Fig. 3.16 shows the temperature dependence of the f_{p_3} fraction and its relaxation λ_{p_3}. Fits to this p_3 relaxation and fraction with a Bolzmann model yield a global activation energy of 0.7(2) eV. Again, this activation energy is too low in comparison with that necessary for capture of an electron from the valence band. The temperature range associated to the process in Fig. 3.16 however coincides with that of polaron ionization, and this process therefore likely corresponds to neutral muonium in the interstitial configuration slowly capturing the electrons released by the polaron. If that is the case $E_a = 0.7(2)$ eV would be the activation energy for the polaron ionization.

$$\begin{aligned} \lambda_{p_3}(T) &= \frac{\lambda_{0p_3} N exp(-E_a/k_B T)}{1 + N exp(-E_a/k_B T)} \\ f_{p_3}(T) &= \frac{f_{0p_3} N exp(-E_a/k_B T)}{1 + N exp(-E_a/k_B T)} \end{aligned} \tag{3.10}$$

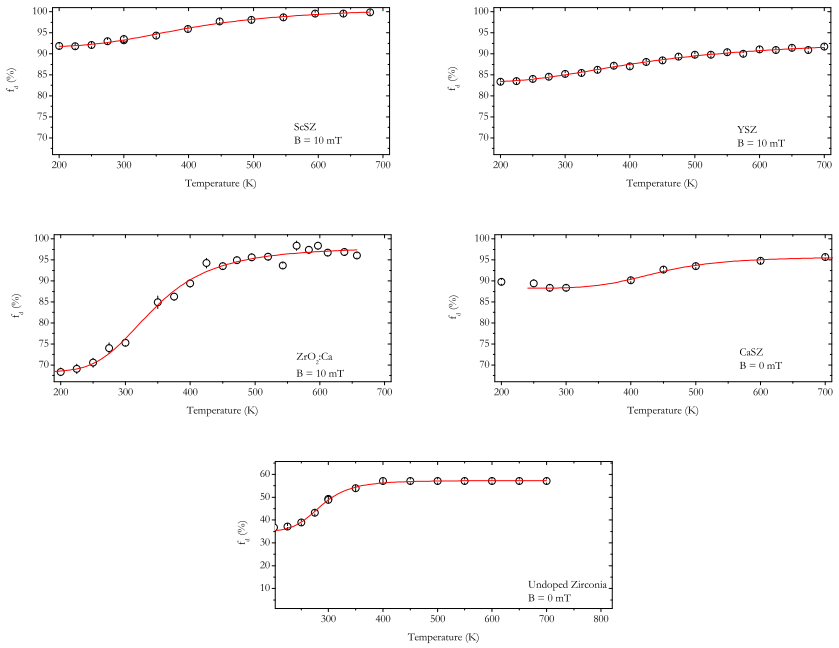

Figure 3.15: *Observed fraction of muon spin polarisation as a function of temperature, in transverse geometry (B = 10 mT), for the ScSZ sample. The line is a fit to a Boltzmann model with an activation energy E_a = 0.14(3) eV, which we associate to the barrier between the atom-like interstitial configuration and the oxygen-bound configuration.*

Table 3.6: *Activation energies of the recovery of the missing fraction (Fig. 3.15) and associated with the barrier between the atom-like interstitial configuration and the oxygen-bound configuration.*

Sample	Activation Energy (eV)
ZrO_2 (undoped)	0.26(2)
ScSZ	0.14(3)
YSZ	0.12(2)
ZrO_2:Ca (monoclinic)	0.21(2)

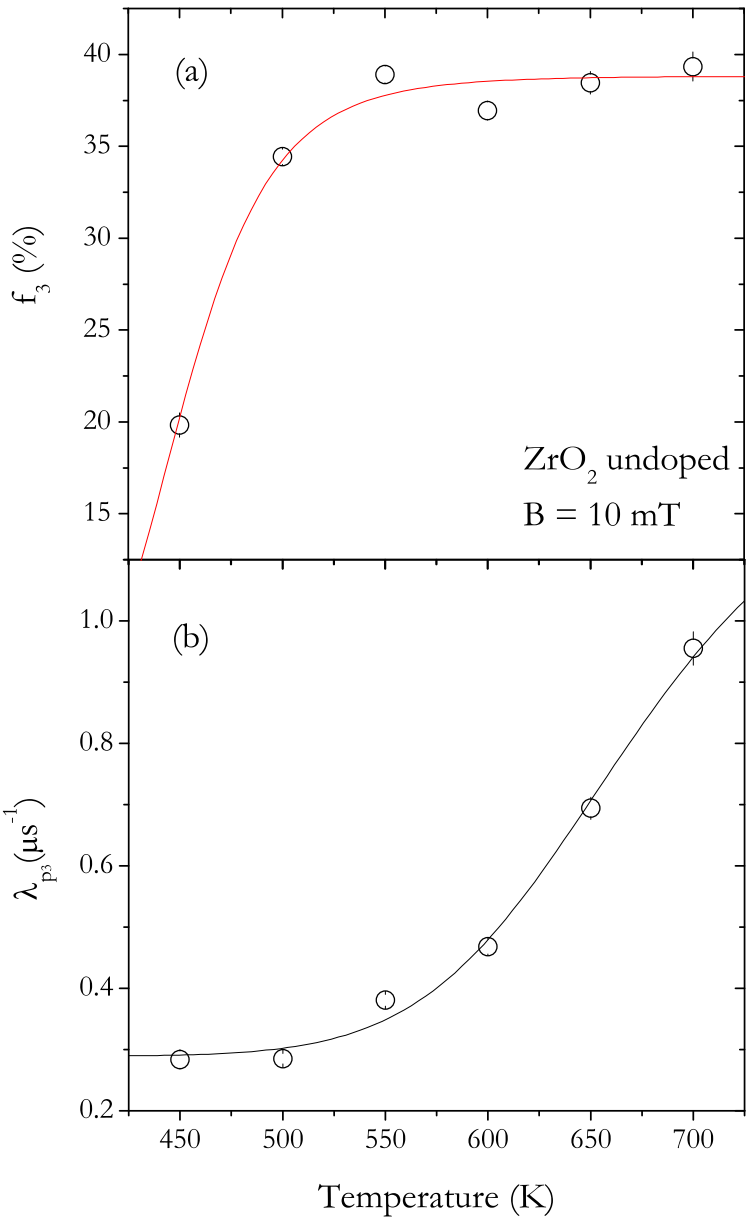

Figure 3.16: *Temperature dependence of the third relaxing paramagnetic component, observed in undoped ZrO_2. (a) Fraction of muon spin polarization f_{p3}; (b) Relaxation λ_{p3}. The lines are a fit to an activated Boltzmann model with a common activation energy $E_a = 0.7(2)$ eV, which we assign to the ionization energy of the Zr^{3+} polaron (see text).*

3.3.5 Hydrogen/Muon long range diffusion

As we have mentioned in the previous section, above 100 K there are signs of muon diffusion in ZrO_2, through the temperature dependence of the relaxation. However in the low-TF measurements these signs are very feeble and difficult to separate from the ongoing polaron dynamics. We have thus performed experiments in zero-field (at ISIS and TRIUMF) in order to try a better separation of the two processes.

In this zero-field experiments, the muon solely experiences the internal magnetic fields generated by its immediate environment. The time dependence of the muon polarisation will therefore be strongly influenced by any fluctuations of those fields, in particular if the muon is diffusing through the samples lattice.

In zero-field measurements a Kubo-Toyabe relaxation of the signal is expected [78, 104, 105]. However, the nuclear magnetic moments in our zirconia samples are very small and the separation of the nuclear relaxation from the paramagnetic polaron relaxation at temperatures higher then 100 K where the long range diffusion of the muon occurs, is extremely difficult. It was therefore impossible to fit the zero-field data using a two component model as in the low temperature TF data. The best fits were obtained using a single lorentzian relaxing component.

$$A(t) = f_{slow} e^{-\lambda_{slow} t} \tag{3.11}$$

This lorentzian relaxation shape reflects the averaging of the relaxation of the muon, as some muons will stop closer to the polaron than others. However the activation energy extracted depends on the temperature dependence of the relaxation that we expect to be identical to all the muons associated to this signal and stopping as oxygen-bonded muons.

In Figs. 3.17, 3.18 and 3.19 we present the temperature dependence of the λ_{slow} relaxation fitted to the zero-field spectra of the ScSZ, YSZ and undoped samples for temperatures up to room temperature. When we compare the temperature dependence of λ_{slow} in zero-field with the correspondent transverse-field data we note that a peak appears in the ScSZ and undoped sample at around 200 K; a plateau appears for the YSZ sample at more or

less the same temperature.

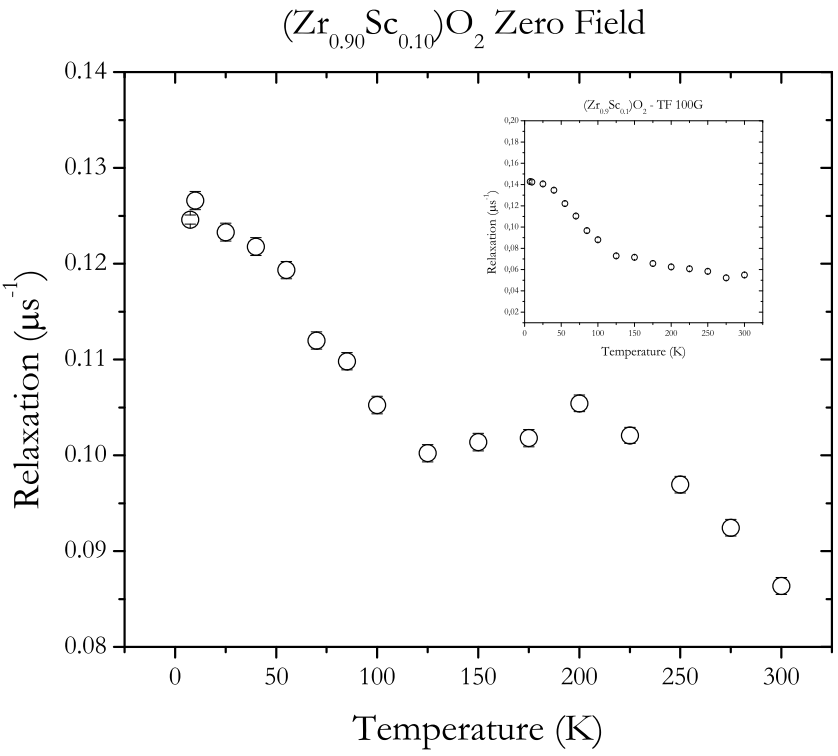

Figure 3.17: *Temperature dependence of the relaxation of the one component fit to the zero-field spectra of the ScSZ sample for temperatures up to room temperature. On the top right corner the temperature dependence of the relaxation of the corresponding one component fit to the transverse-field (10 mT) spectra of the same sample is shown for comparison.*

These peaks likely correspond to trapping peaks; after thermalizing, the muon starts to diffuse and is trapped elsewhere, usually at a high concentration defect. In this case one of the most likely traps for muon/hydrogen is the zirconium vacancy. In fact, positron annihilation studies in ZrO_2 by Cizek et. al [106] show that at room temperature a substantial fraction of positrons decay in a zirconium vacancy populated by a hydrogen atom. Zirconium vacancies therefore are deep traps for protons/muons.

In Figs. 3.20 and 3.21 we present the temperature dependence of the slow relaxation for high temperatures where the decrease of the relaxation after

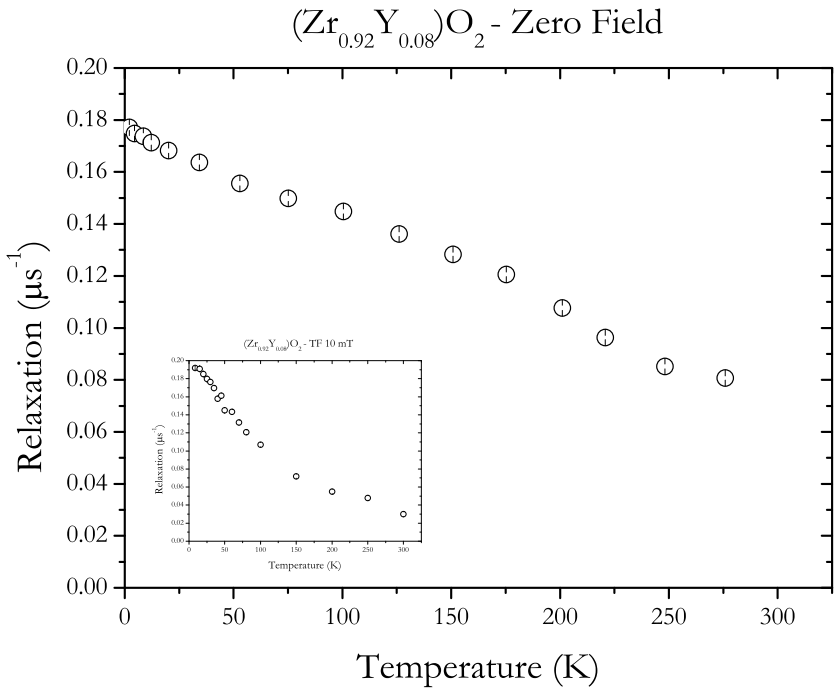

Figure 3.18: *Temperature dependence of the relaxation of the one component fit to the zero-field spectra of the YSZ sample for temperatures up to room temperature. On the bottom left corner the temperature dependence of the relaxation of the corresponding one component fit to the transverse-field (10 mT) spectra of the same sample is shown for comparison.*

the trapping peak is fitted with a Boltzmann like equation, as in Eq. 3.4, yielding a activation energy of 0.3(1) eV and 0.094(8) eV for ScSZ and YSZ respectively.

For the undoped sample, the appearance of the λ_{p_3} relaxing component prevents fitting the temperature dependence of the λ_{slow} to temperatures above 400 K. However the fit to the few temperature points available in Fig. 3.19 allow extracting an activation energy of 0.19(2) eV.

Finally, we note that we proposed quasielastic neutron scattering (QENS) measurements at the OSIRIS instrument at ISIS on our YSZ sample. These measurements were carried out on an "express" proposal by Dr. Mark Telling. In Fig. 3.22 we show the QENS spectra obtained for 203 K, 253 K and 293 K as well as calibration spectra showing the OSIRIS instrument

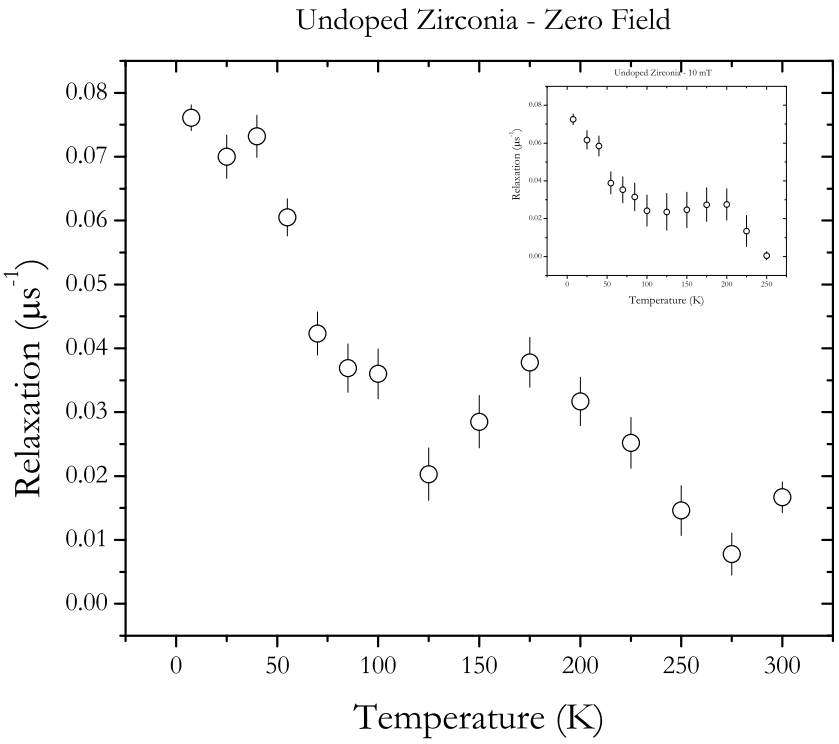

Figure 3.19: *Temperature dependence of the relaxation of the one component fit to the zero-field spectra of the undoped zirconia sample for temperatures up to room temperature. On the top right corner the temperature dependence of the relaxation of the corresponding one componente fit to the transverse-field (10 mT) spectra of the same sample is shown for comparison.*

resolution. A preliminary analysis of this data simply comparing the breath of the Quasi-Elastic peak at $Q = 1$ Å^{-1} as a function of temperature shows distinct broadening as function of temperature, and also when compared to the instrument resolution. This is an indication that there is definitely something moving on the pico-second time scale accessible using OSIRIS. This should most probably be hydrogen moving. Fitting the data with a simple lorentzian and constant background term gives a good fit. If we fit the lorentzian relaxation obtained in function of temperature with a Boltmann model we obtain an activation energy of 0.04 eV. The width of this broadening at 293 K as a function of Q over the usable Q range appears Q-

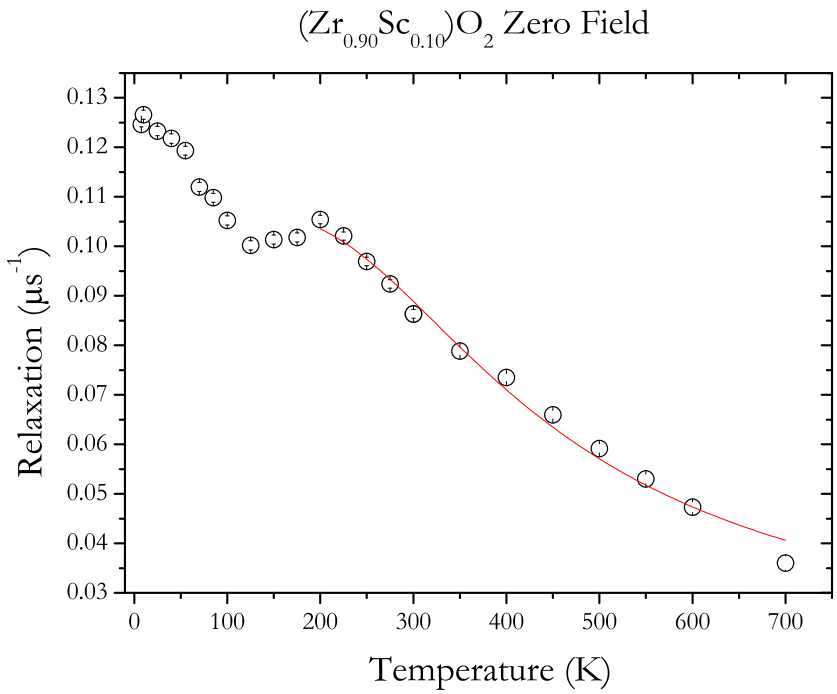

Figure 3.20: *Temperature dependence of the relaxation of the one component fit to the Zero-Field spectra of the ScSZ sample for the full temperature range measured. The fit presented is a Boltzmann like fit as in Eq. 3.4*

independent which suggests that what ever is moving is confined. The mean broadening (FWHM) is approximately 110 μeV

In the existing proton-conduction studies in YSZ [107] they work in wet atmospheres and with porous materials (through-going cavities). The proton movement occurs either in the physisorbed water film (this is relevant below 120 ^oC, where more and more water condensates on the grain surfaces) or for the chemisorbed hydrogen on the grain surfaces. In the present experiment, there is probably no physisorbed hydrogen present (because the sample was in vacuum). Moreover, the experimental data do not conform with diffusion in water because the width for H_2O is 280 meV at 1 $Å^{-1}$ and it is q-dependent.

In the chemisorbed case hydrogen is attached to a surface oxygen forming an O-H bond, similar to the O-μ configuration inside the grain. However, the surface hydrogen may perhaps move somewhat more freely than the muon inside the material. This fact might account to the difference between the

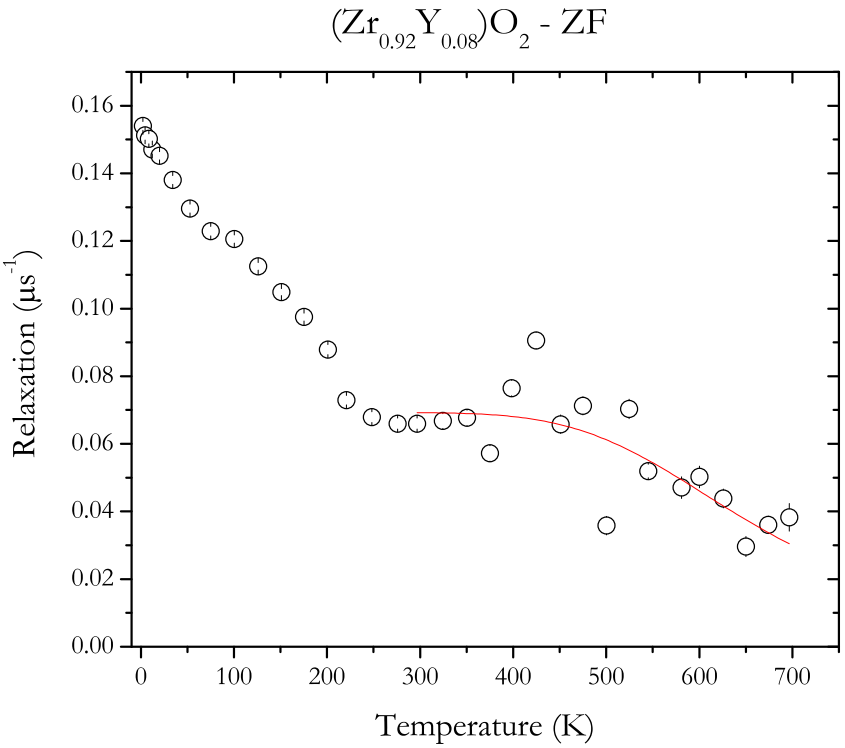

Figure 3.21: *Temperature dependence of the relaxation of the one component fit to the Zero-Field spectra of the YSZ sample for the full temperature range measured. The fit presented is a Boltzmann like fit as in Eq. 3.4 The statistical uncertainties are shown however the real uncertainties should be much higher due to the difficulty of these fits.*

activation energy of the muon diffusion activation energy being higher to the hydrogen diffusion activation energy obtained by QENS.

The various muon/hydrogen movements are discussed by Hempelmann et al. in a Sc-doped $SrZrO_3$ [108] that should be a similar system these zirconium oxides. A possible local motion seen by Hempelmann et al could be the rotation of muon/hydrogen around the oxygen-metal bond axis (muon/hydrogen should be perpendicular to this axis as we know also from TiO_2). But it is still to early in the analysis to have a definitive hydrogen motion model.

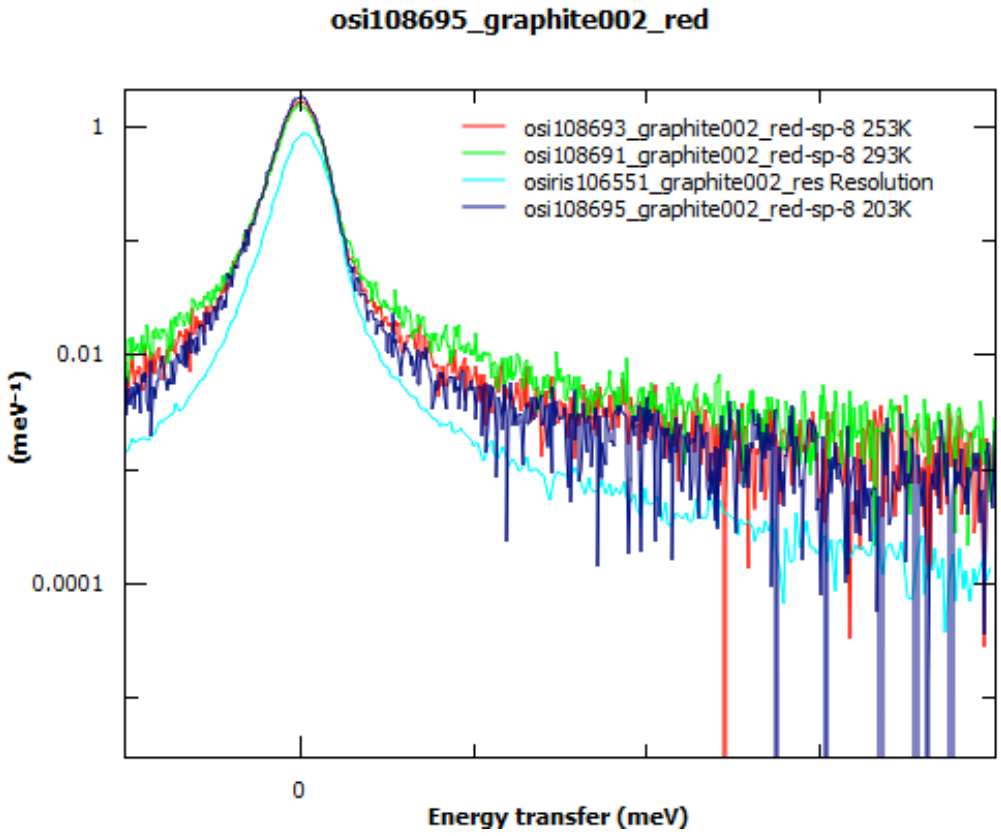

Figure 3.22: *Quasielastic neutron scattering spectra obtained for* 203 *K (violet),* 253 *K (red) and* 293 *K (green) as well as calibration spectra (cyan)*

Chapter 4

Atom-like interstitial state

4.1 Introduction

In Chapter 3 we have presented a model on the hydrogen configurations in ZrO_2. The atom-like interstitial state has for zirconia been identified indirectly by the repolarization of the muon spin in longitudinal fields. In the course of this investigation, we have addressed other high-permittivity oxide systems, with a two-fold advantage: first, this approach allows to underline the basic common features of the isolated hydrogen configurations in oxides, secondly, the details of the particular oxide sample (defects, doping) or electronic structure are bound to impact on the experimental data, allowing to access the same basic configurations from different perspectives.

In the course of this survey of oxides, we have identified for the first time the atom-like muonium state in Lu_2O_3. We have also performed for the first time a detailed characterization of the hyperfine interaction in the alkaline-earth oxides BeO and MgO, which had been identified for long by Brewer J. H., however never published [11], and Kiefl et al. [109]. These atom-like configurations were identified directly by their respective muonium lines observed in high-transverse fields (at TRIUMF for Lu_2O_3, at PSI for the alkaline-earth oxides).

In this chapter, we limit ourselves to presenting the characterization of these atom-like states in Lu_2O_2, BeO and MgO. Besides the particular novelty of the new states identified, the direct identification and characterization

of these states present a particularly enlightening complement to the ZrO_2 data on the atom-like state. Conversely, the models developed for ZrO_2 in Chapter 3 are bound to impact strongly on the development of a full model for the muonium states in these particularly important oxides. This is out of the scope of the present dissertation and will be briefly addressed in Chapter 5.

4.2 Lutetium oxide

4.2.1 Introduction

Lutetium oxide (Lu_2O_3) also known as lutecia is a ceramic material with possible applications in high-power lasers due to its high thermal conductivity (12.2 $Wm^{-1}K^{-1}$) [110, 111], in scintillators due to its high density (approximately 9.4 g/cm^3) [112], in complementary metal oxide semiconductor devices because of its predicted thermodynamical stability on silicon, large conduction band offset and relatively high dielectric constant ($k \approx 12 - 13$) [113].

The Lu_2O_3 crystal structure is isomorphous with Y_2O_3 and belongs to the bixbyite structure type, which is body-centered cubic, space group Ia3-(Th7) (N. 206) with Z = 16 and unit cell parameter a = 10.39 Å[114, 115]. The structure can be represented as an 80-atom cubic *c*-type structure (Fig. 4.1) [116, 114] and is formed by 64 slightly distorted minicubes composed of O anions at the vertices as shown in Fig. 4.2. Only 32 centres of these minicubes are occupied by the Lu metal (M) cations, and the remaining are empty (denoted as structural void-M sites). This type of structure offers two available independent cations sites for the Lu^{3+} atoms with local symmetries C_2 sites (noncentrosymmetric), that we will call M_1, and C_{3i} sites (centrosymmetric), that we call M_2. Each of these Lu^{3+} atoms has 6-fold coordination as is shown in Fig. 4.2. The unoccupied O vertices will be henceforth denoted as unocc-O sites. For the M_2-centred minicubes all of the six anions are equally distanced from the cation center (2.24 Å[115]). In the M_1-centred cube the distance between the anions and the respective cation center occurs with three different paired distances (2.19, 2.20, 2.23 Å[115]).

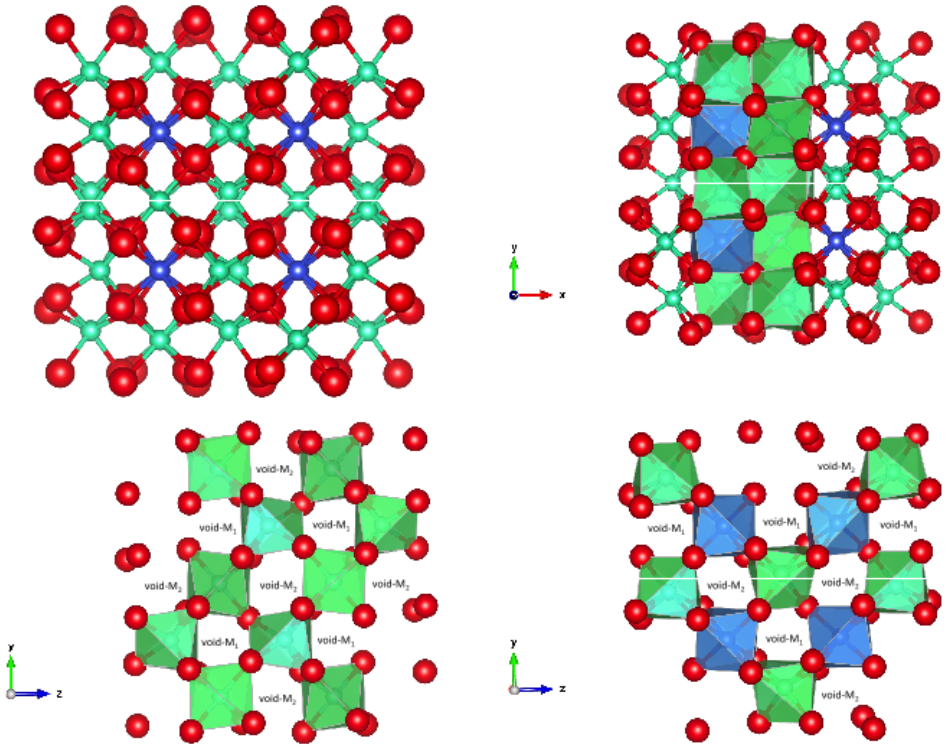

Figure 4.1: *Conventional bixbyite structure type cell of Lu_2O_3. O is represented by the larger red spheres and Lu by the smaller blue (M_2) and green spheres (M_1). The structural interstitial voids sites of the lattice are labelled accordingly. Figure obtained using VESTA [117] and the crystallographic parameters in [114].*

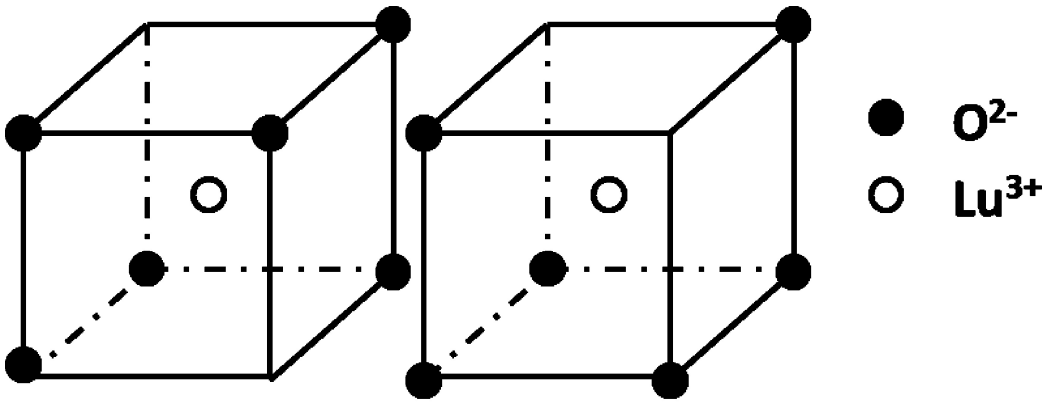

Figure 4.2: *Schematic of the two available independent cations sites for the Lu^{3+} atoms with local symmetries C_2 (noncentrosymmetric), here named M_1 (on the right) and C_{3i} (centrosymmetric), here named M_2 (on the left).[114]*

Fig. 4.1 represents part of the conventional cell of lutecia denoted with the above mentioned crystallographic sites.

Hydrogen as an ubiquitous impurity can be unintentionally incorporated during the growth environment [118], in particular in the presence of water for Lu_2O_3 [119].

Prior to our work little was known about hydrogen defects in Lu_2O_3. In conjunction to our experimental μSR study a theoretical study was performed by Estelina da Silva et al. [18], which we briefly summarize in the following subsection.

4.2.2 Theoretical results

In the theoretical work parallel to this dissertation, first-principal calculations were performed using DFT (density functional theory).

Three stable configurations were found for H^0, in close analogy with those found in the isostructural Yttrium oxide. [16] One stable configuration exists for the interstitial unoccupied O site (unocc-O) and another for the interstitial void metal at the M_1-centre (void-M_1) (Figs. 4.3 and 4.4, respectively). The resulting relative energies between these two configurations imply that unocc-O is lower in energy than void-M_1.

A third stable H^0 configuration found is a bond O-H system (bond-O), where H binds to a O ion (Fig. 4.5). The energy of this bond configuration is higher when compared to the interstitial neutral configurations.

The same configurations, with similar relative energy ordering, were found for the negatively-charged systems. In contrast, for the H^+ state, only the bond-O configurations are found as energy-minima.

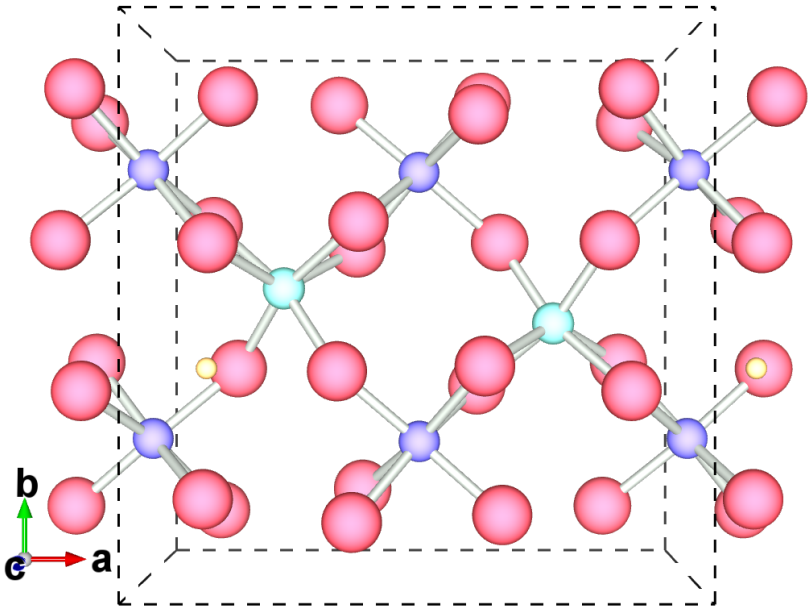

Figure 4.3: *DFT stable H configuration for the H^0 and H^- states. The H impurity (represented by the small yellow sphere) stabilizes at an unoccupied O site.*

For the bond-O configuration the preferred configuration of the charged impurity will allow the lowering of interatomic forces which will in turn lower the overall energy cost due to the overlapping electron densities. These configurations show a stronger lattice distortion, when compared to the interstitial H configurations, which is more pronounced for the positively charged states. At the close vicinity of the impurity center, several Lu-O bonds 'deform' from their original lengths in order to accommodate the perturbation caused by the impurity.

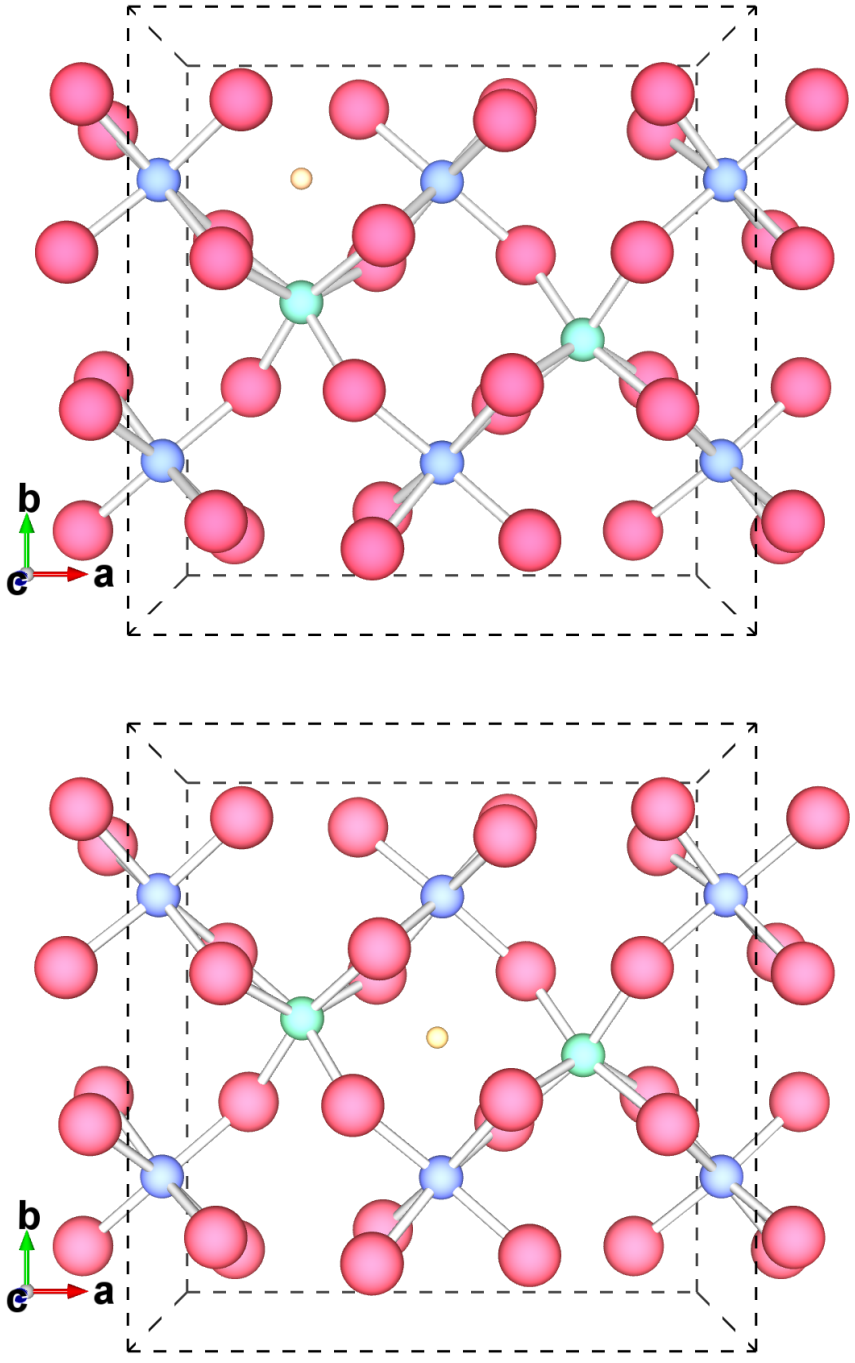

Figure 4.4: *Stable H configuration for the H^0 and H^- states. The H impurity stabilizes at a void metal centre. The top plot represents the void-M_1 configuration and the bottom plot the void-M_2 configuration. The latter configuration is not found at all levels of the theory for the neutral state and is not stable with the refined approach.[18]*

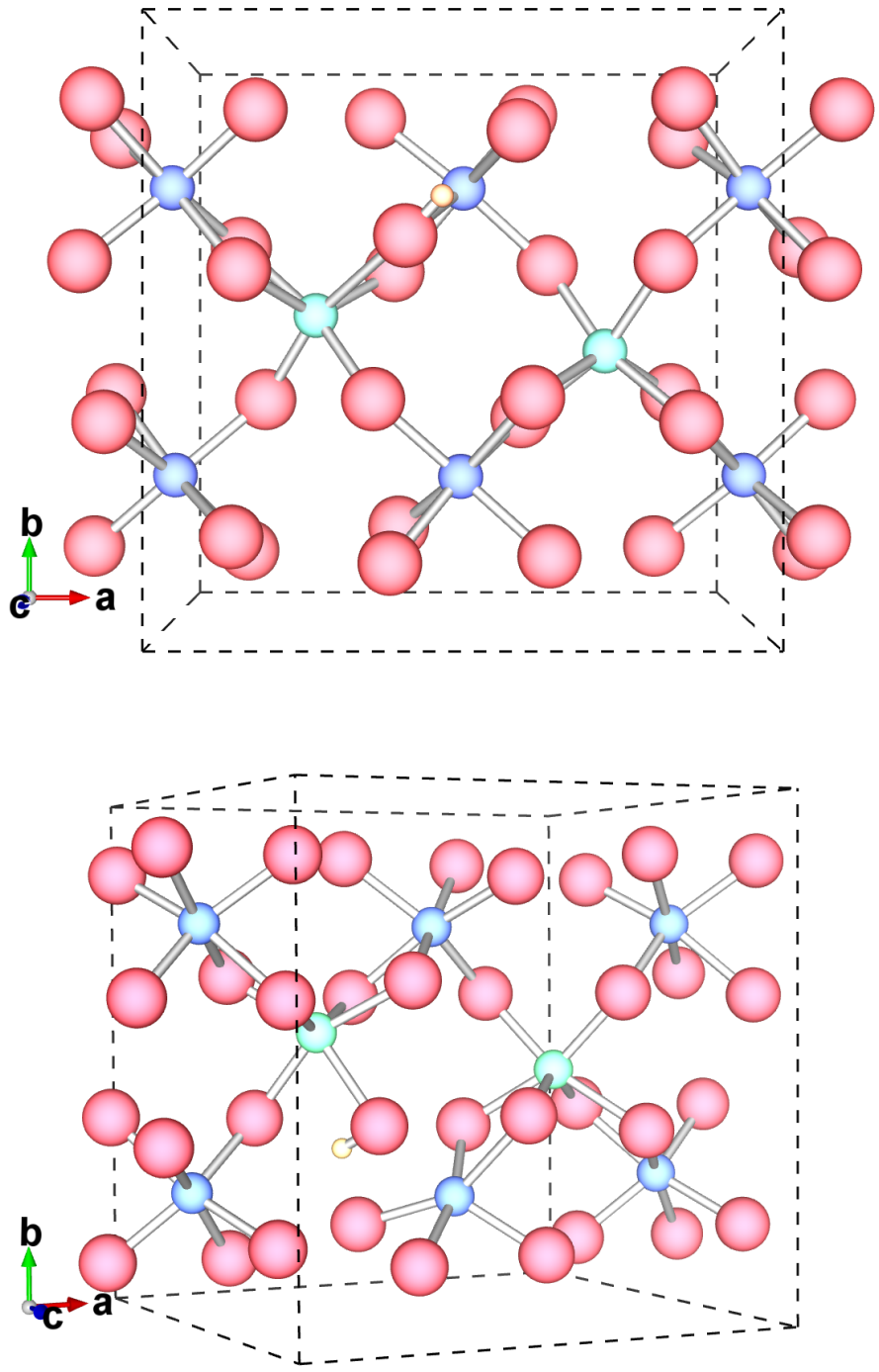

Figure 4.5: *DFT+U bond-O configurations of the H impurity for the H^0 (top) and H^- (bottom) charge states. The stable configuration for the H^+ system is similar to the H^- state. The presented structures are the representative lowest-energy bond-O configurations.*

For the DFT methods, the formation energies show that the most stable hydrogen configuration of the neutral and negative charged systems is at the unocc-O site. For the positive charged states, only the bond-O configuration exists, although it occurs with different surrounding environments. For the neutral and negatively charged systems, higher-energy configurations also occur, and the bond-O configurations are energetically less favourable for both charged systems than the configuration with hydrogen at the void-M_1 site (see Fig. 4.6). The fact that this bond-O configuration is higher in energy than the interstitial configurations is consistent with findings for other oxides, i.e. yttria,[16] uranium oxide. [120]

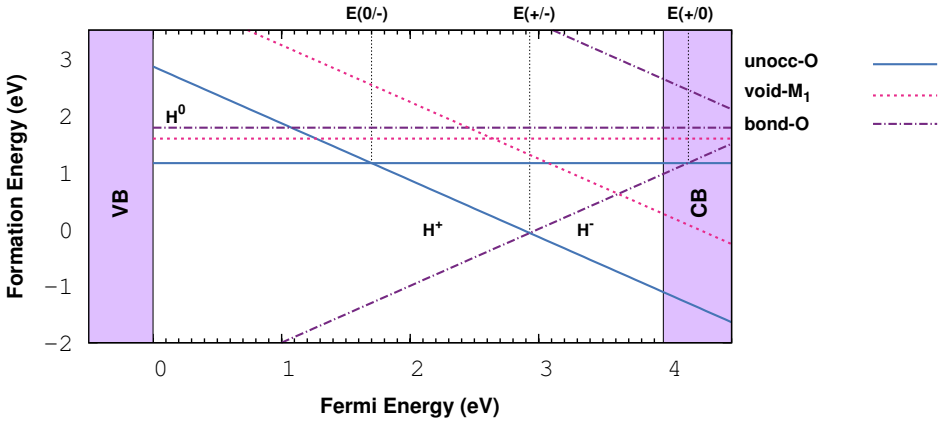

Figure 4.6: *Formation energy of the different hydrogen configurations as a function of the Fermi-level position. The range of E_F corresponds to the bulk theoretical band-gap with E_F=0 aligned at the valence-band maximum. The formation energies of the different geometrical configurations are represented by different line types and colors. The thermodynamic charge-transition (electrical) levels are marked by the vertical lines.*

For the higher energy, bond-O, configurations, the respective pinning and the donor levels lie above the conduction band minimum. From these results it can infered that a portion of these bond-type configurations are shallow donor-like configurations with corresponding donor and pinning levels interacting with the conduction band states.

For the calculated unocc-O and void-M_1 configurations, the defect levels

are positioned quite close to the valence-band. The unocc-O configuration impurity level is found at 0.3 eV above the valance band maximum. The void-M_1 configuration level is positioned at higher energies, although still close to the valance band maxium - 1.4 eV. The oxygen-bond configurations level is positioned very close to the conduction band minimum ($\sim$ 0.2 eV below the conduction band minimum).

The electron-density isosurfaces of the neutral systems were also evaluated in order to provide a more detailed information regarding the nature and localization of the impurity electron.

For the unocc-O and the void-M_1 configurations, where a defect level is positioned close to the valence band maximum (Fig. 4.7), one may observe that the isosurfaces possess a strong *s*-type character with the electron centred at the impurity.

For the bond-O systems, and similarly to what was found in Ref. [16] for yttria and in Ref.[15] for cubic zirconia, one may observe that the hydrogen electron is trapped at the closest cation neighbours (Fig. 4.8). In response to the formation of the impurity-anion bond, significant lattice distortion takes place for these configurations. The resulting displacement field near the hydrogen impurity causes the defect electron to become trapped close to the impurity atom, at a cation centre. [11] This behavior resembles the effect (already suggested by Cox *et al.*[11]) of a polaron-type formation, where the polaron-center may be shallow and therefore act as a donor-centre as well. The impurity electron is trapped close to the hydrogen nucleus, at nearby metal centres, and has predominantly a conduction-band *d*-type character - the defect-level is positioned quite close to the conduction-band allowing the respective states to interact with each other (Fig. 4.8).

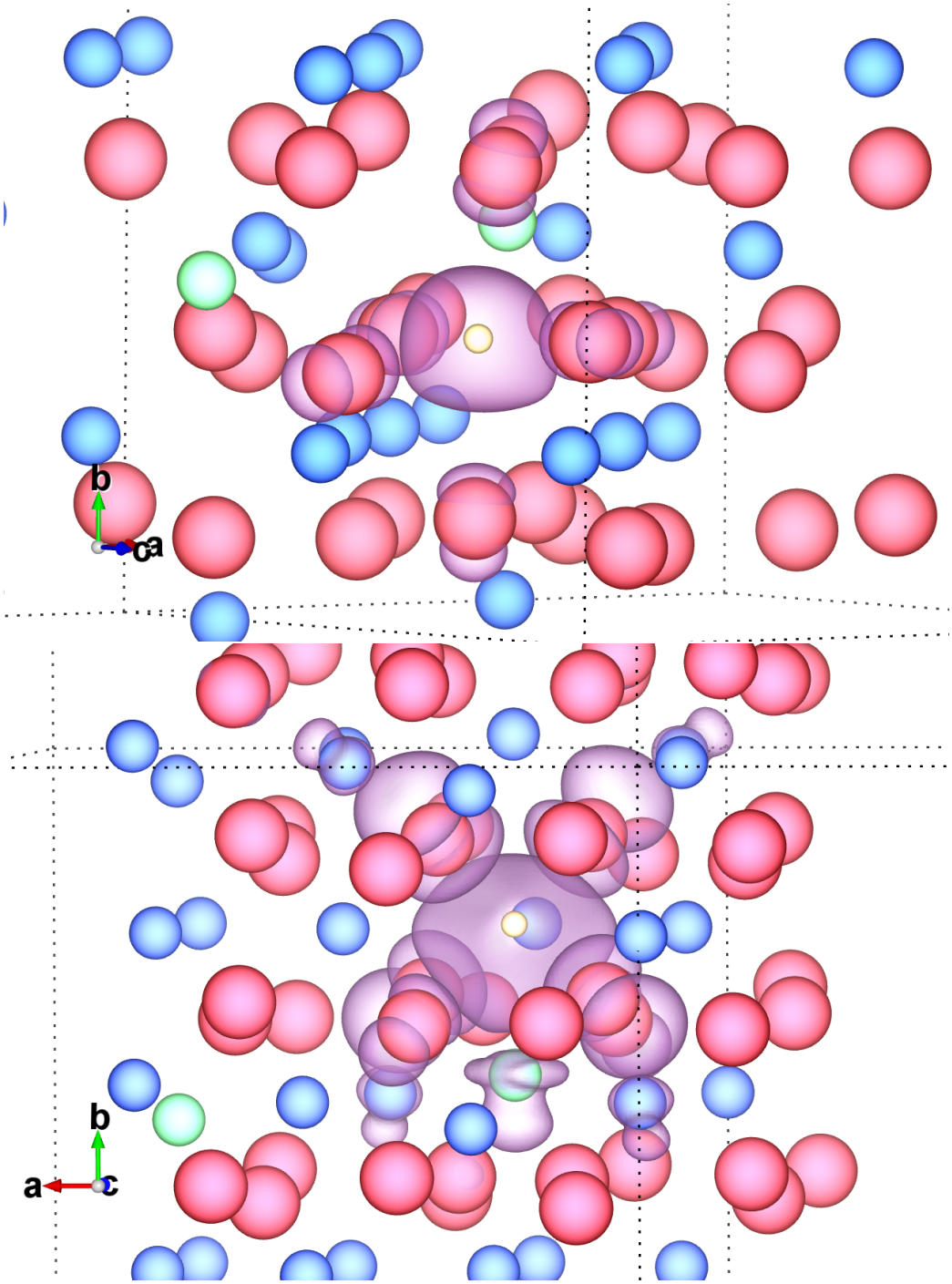

Figure 4.7: *Isosurfaces of the electron charge densities for the neutral state of unocc-O and void-M_1 configurations. The atoms are represented by their ionic radius, where O is depicted in red, Lu in blue/green and hydrogen in yellow.*

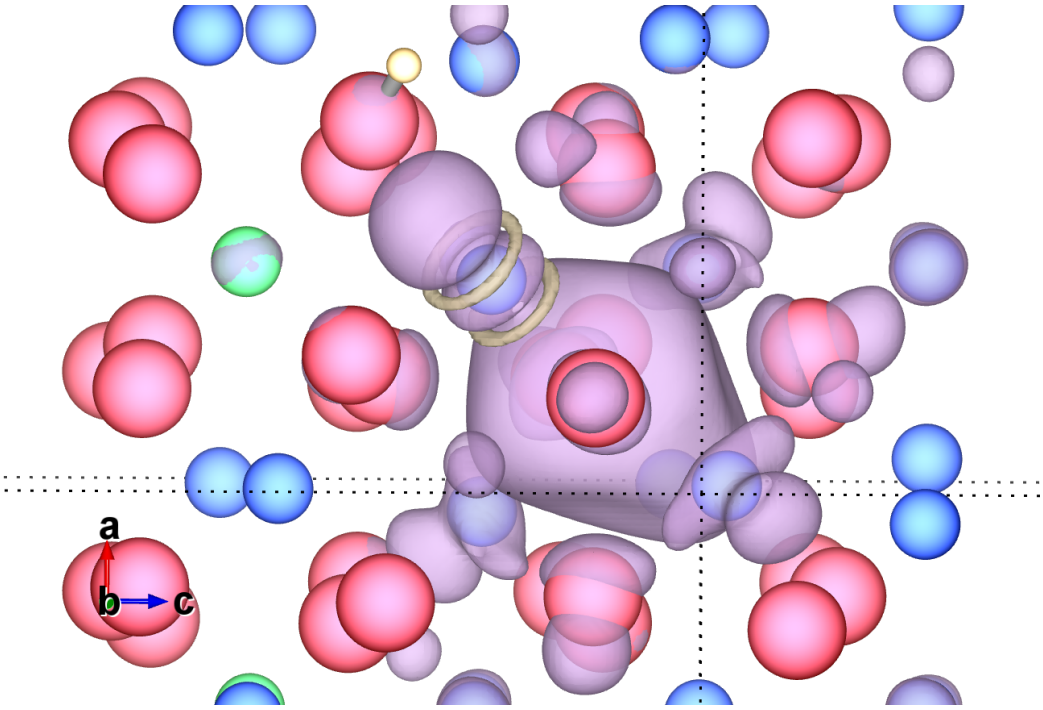

Figure 4.8: *Isosurfaces of the electron charge densities for the neutral state of the representative, lowest energy, bond-O configuration. The atoms are represented by their ionic radius, where O is depicted in red, Lu in blue/green and hydrogen in yellow. The purple color of the isosurface refers to positive values and the yellow to negative values.*

Hyperfine Constants

The calculation of the hyperfine tensors was also performed for the neutral impurity centers in order to allow a direct comparison with the experimentally obtained hyperfine constants measured by μSR.

The calculations for the neutral interstitial hydrogen configurations (hydrogen at the unoccupied unocc-O and void-M_1 sites) revealed a predominant isotropic component with very small dipolar part. The Fermi-contact isotropic constant, A_{iso}, was found equal to be 926 MHz and 1061 MHz for the unocc-O and void-M_1 configurations, respectively. These results indicate that it is the latter configuration which yields a higher spin localization.

4.2.3 Interstitial atom like muonium state

The Lu_2O_3 sample used in the present study was obtained commercially from Alfa-Aesar (REActon 99.995%). As mentioned in 4.2.1, the main objective of this chapter is to present the direct characterization of the atom-like muonium state in high-k oxides. We begin therefore by presenting μSR measurements in high-transverse fields obtained with the HiTime spectrometer on the M15 surface muon channel at TRIUMF (Vancouver, Canada) As shown in Fig. 4.9, the μSR spectrum at $T = 300$ K, for an external applied magnetic field $B = 7$ T, shows a clear oscillating pattern, which corresponds to the beating between two frequencies identified at $\nu_{\rm d} = 948.96(2)$ MHz and at $\nu_{12} = 833.2(2)$ MHz. The corresponding Fast-Fourier Transform (FFT) for applied fields of 2, 4 and 7 T are shown in Fig. 4.10. ν_d corresponds to the expected Larmor frequency of the diamagnetic muon at the applied field. ν_{12} is the frequency characteristic of the $1 \rightarrow 2$ transition in the field-dependent hyperfine spectrum of muonium. In the high-field limit, this frequency corresponds to the "flip" of the muon spin with electron spin up and amounts to half of the spectral weight. The other half of the spectral weight corresponds to the unobservable ν_{34} frequency characteristic of the $3 \rightarrow 4$ transition where the muon spin "flips" with electron spin down. The time spectrum in Fig. 4.9 was analysed using a sum of damped oscillations of the form:

$$A(t) = A_{\rm dia} e^{-\lambda_{\rm dia} t} \cos\left(2\pi\nu_{\rm dia} t + \phi_{\rm dia}\right) + A_{\rm Mu} e^{-\lambda_{\rm Mu} t} \cos\left(2\pi\nu_{\rm Mu} t + \phi_{\rm Mu}\right) \quad (4.1)$$

A room temperature calibration with a silver sample at $B = 7$ T allowed to extract the maximum instrumental asymmetry $A_{\rm max}$ and therefore to measure the fraction of muons thermalizing at the diamagnetic configuration ($f_{\rm dia} = A_{\rm dia}/A_{\rm max}$) and the fraction of muons thermalizing at the paramagnetic muonium configuration ($f_{\rm Mu} = 2A_{\rm Mu}/A_{\rm max}$, where the multiplication by two accounts for the unobservable v_{34} transition). We find that $f_{\rm dia} = 23(1)\%$ and $f_{\rm Mu} = 46(3)\%$. The corresponding relaxations were found to be $\lambda_{\rm dia} = 0.1(1)\,\mu\,s^{-1}$ and $\lambda_{\rm Mu} = 6(1)\,\mu\,s^{-1}$.

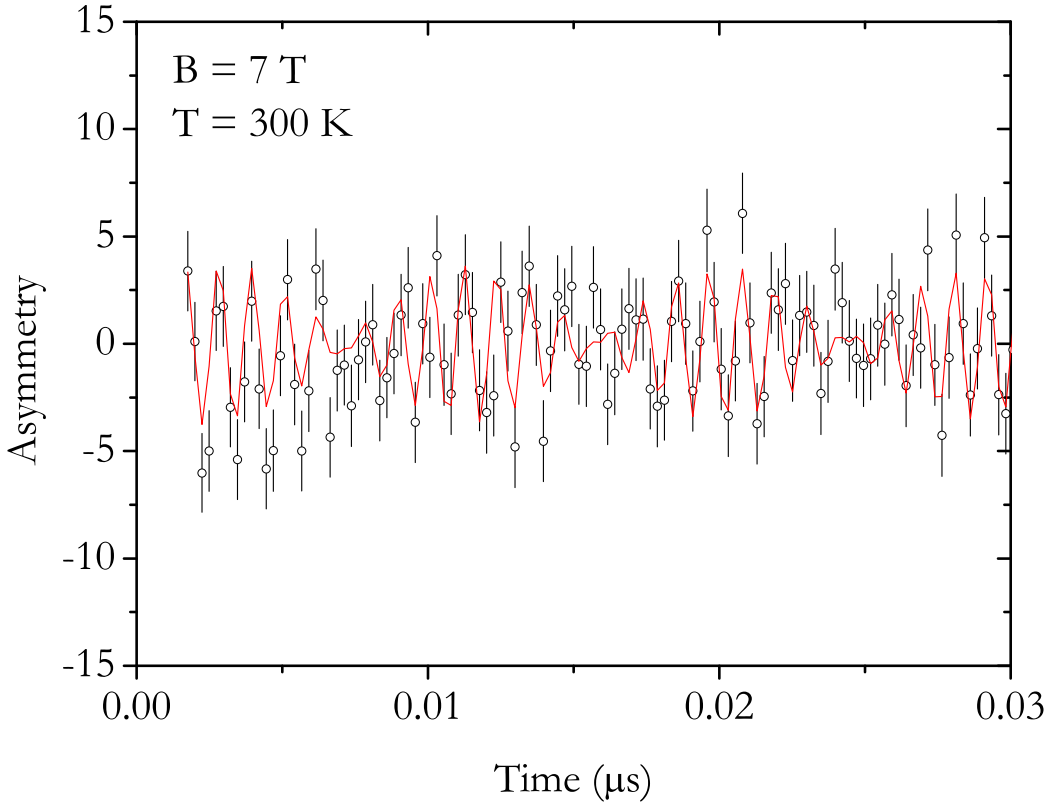

Figure 4.9: *μSR time spectrum of a polycrystalline sample of Lu_2O_3, for an applied transverse magnetic field $B = 7$ T, at $T = 300$ K. The beating of the diamagnetic frequency and of the muonium ν_{12} line is clearly seen. The red line is a fit as described in the text.*

The experimental observations are consistent with the presence of an isotropic hyperfine interaction. The frequencies ν_{12} plotted in Fig. 4.11 were therefore fitted according the following equation which arises immediately from Table 1.3:

$$\nu_{12} = \left| \frac{A_{iso}}{2} + \nu_- - \frac{\nu_+}{\beta} \right| \tag{4.2}$$

where A_{iso} is the hyperfine parameter, $\nu_\pm = (\gamma_e \pm \gamma_\mu)B/2$, (with $\gamma_e = 28024.21$ MHz/T and $\gamma_\mu = 135.53$ MHz/T), and $\beta = \sqrt{1 + (A_{iso}/2\nu_+)^2}$. The fit in Fig. 4.11 yields $A_{\rm iso} = 3597(1)$ MHz.

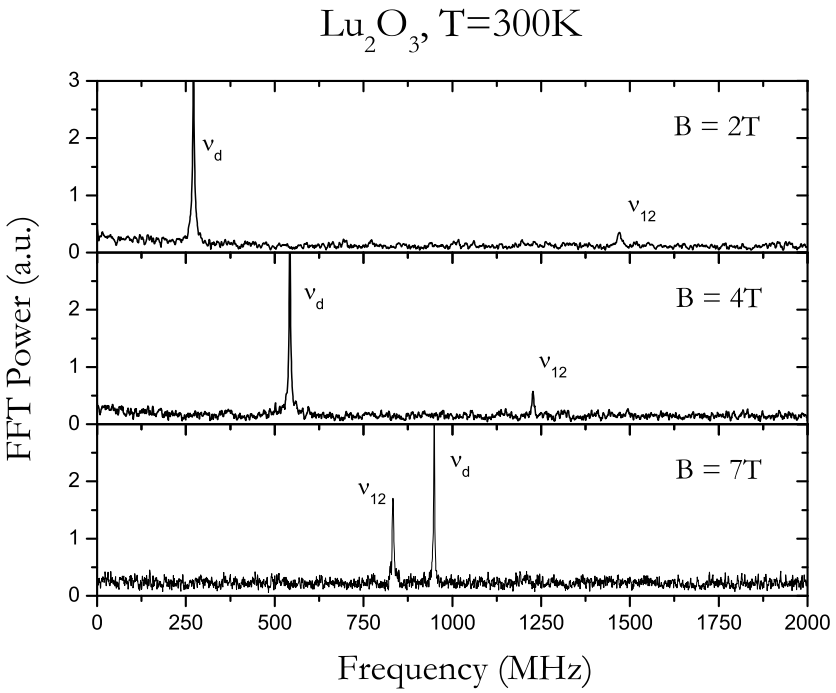

Figure 4.10: *Fast-Fourier transform (FFT) of the μSR time spectrum at room temperature, for an applied transverse magnetic fields of $B = 2$ T, $B = 4$ T and $B = 7$ T showing the presence of the diamagnetic frequency ν_{d} and of the muonium ν_{12} frequency.*

In order to compare this value with the calculated values for hydrogen, we must take into account that the hyperfine interaction for muonium is expected to be higher than that for hydrogen by the factor 3.184 corresponding to the ratio of the magnetic moment of the muon and that of the proton. [13] The expected value for the experimentally-measured hyperfine interaction, taking the correction into account, is equal to $A_{\mathrm{iso}} = 1129.7(3)$ MHz. This means that the calculated values for the unocc-O and void-M_1 interstitial configurations (see previous subsection) are lower than the experimental value by 18% and 6%, respectively. These discrepancies are judged satisfactory given the approximate treatment of exchange and on-site correlation adopted in the theoretical calculations.

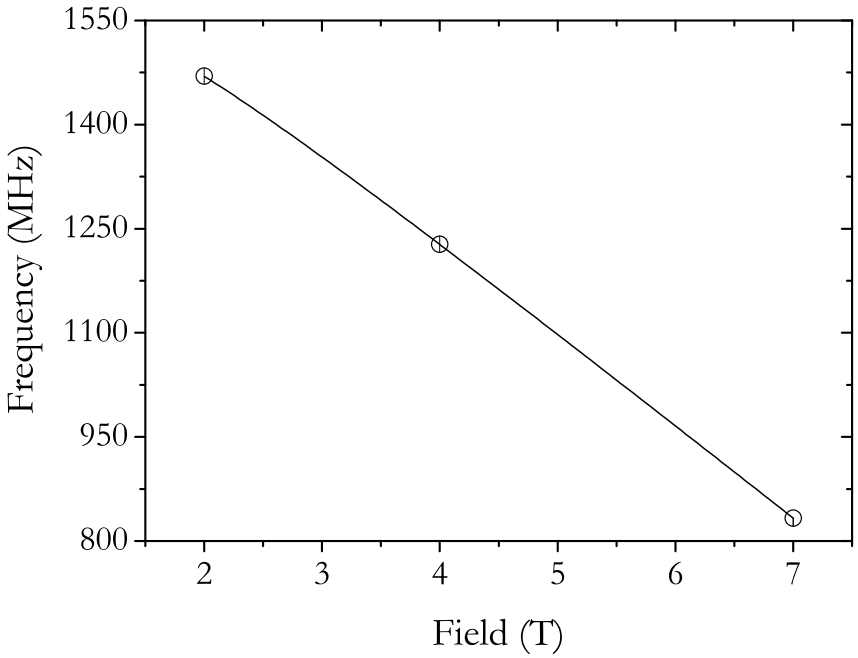

Figure 4.11: *Frequency ν_{12} as a function of applied transverse magnetic field, as obtained from the fits to the time spectra. The lines are a fit to an isotropic muonium state with the hyperfine parameter A_{iso} as the single fitting parameter, resulting in $A_{\mathrm{iso}} = 3597(1)$ MHz.*

In fact, similar discrepancies have also been reported recently between the hyperfine interactions calculated by *ab-initio* methods and those measured experimentally. [40] These authors report differences of about 15% to 20% in the calculation of hyperfine interactions in solids using the PBE functional, which notably decrease when using a hybrid-functional (HSE06) approach. Also (and more in relevance to the present work), in a study [17] of hyperfine parameters of neutral hydrogen configurations in zirconia, the isotropic constants calculated within PBE were smaller to those obtained by HSE06 by as much as 10 % (for a fixed plane-wave cutoff energy). Taking into account that the calculated values of the hyperfine interactions for the unocc-O and void-M_1 interstitial configurations are themselves different by less than 15%, it is not possible to assign the experimentally observed muonium state to a

specific configuration from the value of the hyperfine interaction alone. The observed value is nevertheless consistent with the calculated values. It is also important to note that a slight variation of the value of the hyperfine interaction of muonium with respect to that of hydrogen is expected due to the different zero-point motion of the muon and of the proton.

In short, these results basically reveal the formation of an atom-like muonium configuration with an hyperfine interaction of 3629(2) MHz at low temperatures, in line with the calculated values for any of the interstitial positions of hydrogen in Lu_2O_3. Together with the muonium state directly observable spectroscopically, there is evidence of the presence of another atom-like state, possibly a precursor configuration. Although the experimental data do not provide a direct identification of the muonium site corresponding to the directly observed state, the fact that this state is formed promptly in the wide temperature range from $T = 7$ K up to $T = 300$ K implies that it corresponds to a very stable configuration, possibly the ground state configuration at the unocc-O site.

We have also followed the temperature dependence of this Mu state down to $T = 2.5$ K, and found that the same isotropic state is present at low-temperatures, albeit with a smaller fraction ($\sim 20\%$) and a slightly larger hyperfine interaction $A_{\rm iso} = 3629(2)$ MHz, corresponding to $A_{\rm iso} = 1139.8(6)$ MHz after taking the referred magnetic moment ratio into account. The temperature dependence of the muonium fraction is shown in Fig. 4.13 and the temperature dependence of the hyperfine interaction is shown in Fig. 4.12. The full modelling of the temperature dependence is not of the scope of the present dissertation, but a few points can be immediately discussed.

We begin noting that the slight decrease of the hyperfine interaction with increasing temperature is a well known effect of the onset of lattice vibrations. [28, 100] The decrease in the hyperfine interaction with temperature is most likely due to local vibrational mode (e.g. the oscillation of the muonium in the potential provided by the crystal matrix). If we assume that is the case the change of the hyperfine interaction is adequately described by a series on the mean square displacement $< u^2 >$ [100]:

$$a(T) = a_0 + a_2 < u^2 > + a_4 < u^2 > + ... \tag{4.3}$$

Within this harmonic oscillator model, the temperature dependence can be obtained from a Boltzmann distribution. Admitting a single vibrational frequency ν that produces an energy of $E_a = h\nu$ (known as the Einstein model), one arrives at the following formula for the temperature dependent isotropic interaction A(T):

$$A(T) = A_0 + \frac{C_1}{\exp(E_a/kT)} + \frac{C_2}{(\exp(E_a/kT))^2} \tag{4.4}$$

where A_0 is the hyperfine interaction at $T = 0$ K and E_a is the single vibration frequency in the Einstein model. The coupling constants C_1 and C_2 are assumed temperature-independent. This model was used in the II-VI zinc-chalcogenide widegap semiconductors with great success [19].

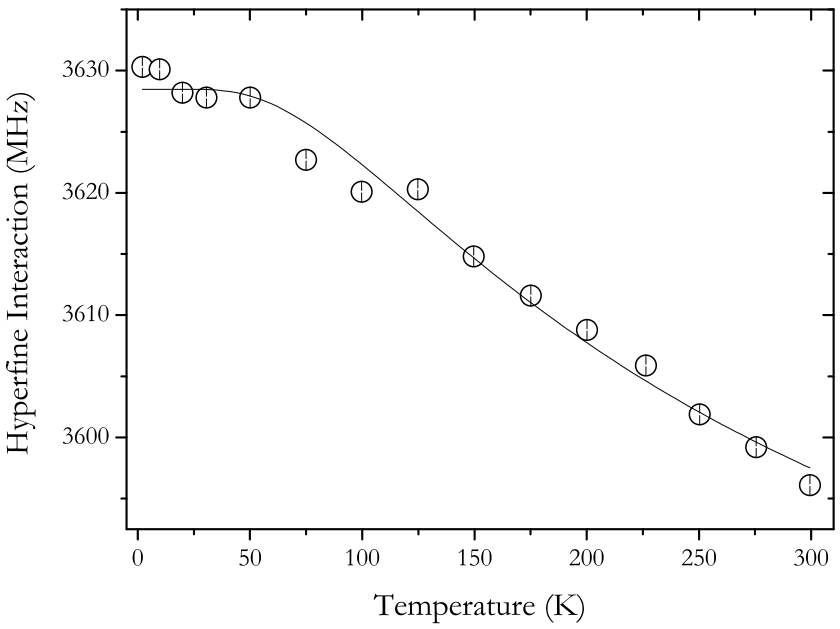

Figure 4.12: *Temperature dependence of the hyperfine interaction of the atom-like muonium configuration. The solid line is a fit using an Einstein model.*

For this oxide this model was used for the temperature dependence of the hyperfine interaction in Lu_2O_3 and we observed that only the first two terms of equation 4.4 were needed to fit the data and produce a good result as shown in figure 4.12. This is a sign that the oscillations of the interstitial muonium are very small. The parameters obtained in the fit were $C_1 = -69(6)$ MHz, $A_0 = 3628,5(7)$ MHz and $E_a = 21(2)$meV.

A second important point to be highlighted in the temperature dependence of the atom like state is the variation of the muonium fraction with temperature (Fig. 4.13). The formation probability relates to the muonium formation process and is a temperature-dependent process. [91, 92, 94] The increase of the formation probability of the observed muonium state with increasing temperature is reflected in the corresponding decrease of the unobservable fraction of muon spin polarization (missing fraction), the diamagnetic fraction remaining sensibly constant. We have fitted the temperature dependence of the muonium fraction in Fig. 4.13 with a Boltzmann model:

$$f_{Mu}(T) = \frac{f_{Mu_0} N exp(-E_a/k_B T)}{1 + N exp(-E_a/k_B T)} \tag{4.5}$$

where f_{Mu} is the muonium fraction, E_a is the activation energy of the process, k_B is the Boltzmann constant, and the empirical parameter N relates to the shape of the binding potential. We obtain $E_a = 0.15(7)$ eV. The missing fraction is associated to muons whose spin polarization is lost during the thermalization process and therefore reflects the presence of another paramagnetic state, either as a precursor or as a final state. [91, 92, 94] The diamagnetic fraction is likely associated to muons thermalizing as Mu^+ in oxygen-bond configurations.

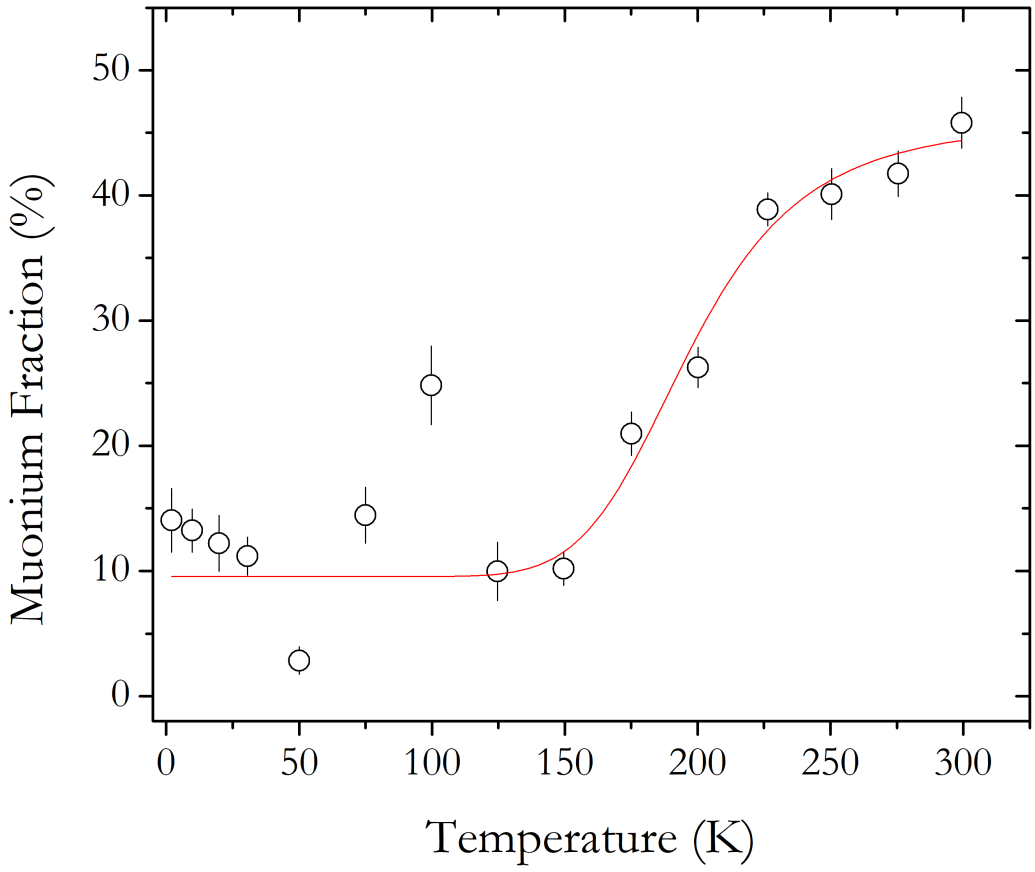

Figure 4.13: *Temperature dependence of the atom-like muonium fraction. The solid line is a fit using a Boltmann distribution function.*

4.3 Alkaline earth metal oxides

4.3.1 Introduction

The interest in the alkaline earth metal oxides has known a growth in the last years due to the fact that they are prime candidates for use as the interface passivation layer for III-V metal oxide semiconductor devices [121, 122, 123] which unpins the Fermi level at the oxide-dielectric/ III-V substrate interface in HfO_2 based MOSFETs [4]. In addition, BeO is also a candidate for the replacement of HfO_2 as high-k gate dielectric in high power applications [124]. MgO is also strongly considered as potential solid fuel cell catalyser [125].

H^- ions are known for long to be the electron traps responsible for the long lifetime of F luminescence in MgO [126]. In MgO films deposited by pulsed laser deposition, hydrogen has been recently proved to introduce additional electron traps attributed to H^- at an oxygen vacancy site [127]. Recently, hydrogen was suggested to be a two level system defect in atomic layer deposition BeO [128]. *Ab-initio* calculations are available both for hydrogen in MgO and BeO. For MgO, Li and Robertson [54] have calculated the position and formation energy (shown in Fig. 4.14) for the most stable positions of H^-, H^0 and H^+ and found H^- and H^0 at an interstitial position and H^+ retains weak bonds with three Mg atoms and at the same time binding strongly to an O atom.

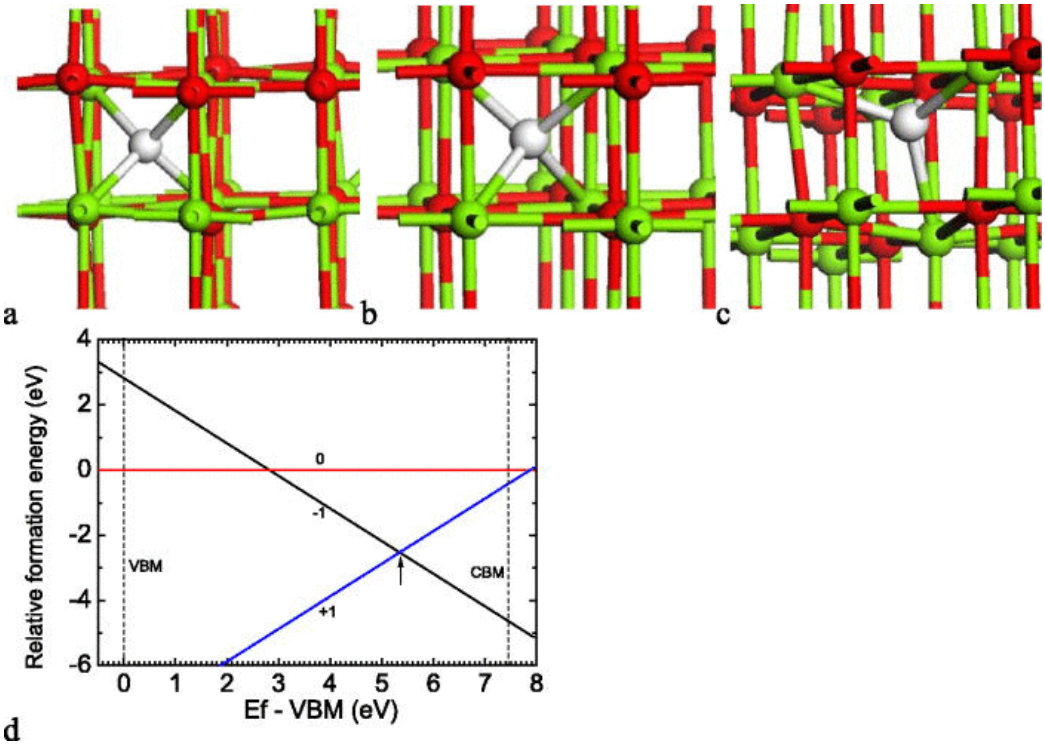

Figure 4.14: *Atomic configurations of H interstitial of different charge states in MgO, (a) H^-, (b) H^0, (c) H^+, and (d) charge transition diagram. Figure from Li and Robertson [54] and reprinted with authorization.*

.

For BeO a thorough theoretical work was performed by A. G. Marinopou-

los [129], who calculated not only the most stable position for the charged species, but also metasable sites (Fig 4.15) Most importantly, in these theoretical calculations in BeO the hyperfine interaction of the neutral states have been calculated, allowing a direct comparison with experiment (Table 4.1)

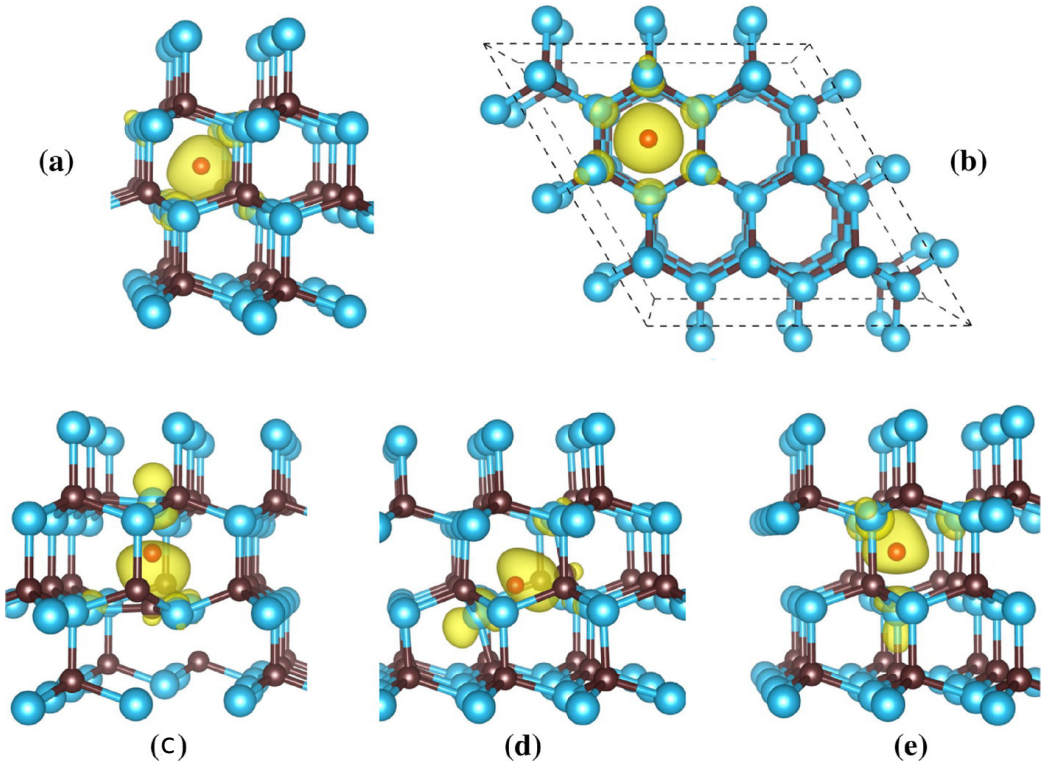

Figure 4.15: *Stable neutral hydrogen configurations and their spin-density isosurface (depicted in yellow) for BeO as obtained from hybrid-functional calculations performed by A. G. Marinopoulos [129]. (a) Ground-state interstitial configuration* $H^0_{\rm int}$*; view perpendicular to the* **c** *axis. (b) Ground-state interstitial configuration* $H^0_{\rm int}$*; view parallel to the* **c** *axis. (c) Elongated-bond-type configuration,* H^0*-*$OH_{\parallel}$*, with OH bond parallel to the* **c** *axis. (d) Elongated-bond-type configuration,* H^0*-*$OH_{\perp}$*, with OH bond almost perpendicular to the* **c** *axis. (e) Higher-energy interstitial configuration* $H^0_{\rm int2}$*; view perpendicular to the* **c** *axis. Elements are represented as: H (small red sphere), Be (small dark-brown spheres), O (large blue spheres).*

.

Table 4.1: *Formation energies (in eV) and hyperfine constants (in MHz) of the different neutral hydrogen configurations in BeO, obtained by different functionals (PBE and HSE06). The formation energy of the ground-state configuration ($H^0_{\rm int}$) provides the reference energy for the quoted energies.*

	PBE			HSE06		
	$\Delta E_{\rm form}$	$A_{\rm iso}$	D	$\Delta E_{\rm form}$	$A_{\rm iso}$	D
$H^0_{\rm int}$	0.00	1329	4.5	0.00	1460	4
H^0-$OH_{\parallel}$	0.73	670	51	0.99	693	60
H^0-$OH_{\perp}$	0.89	605	54	1.13	655	56
$H^0_{\rm int2}$	1.15	1171	4.5	1.41	1307	5

4.3.2 Experimental details and analysis

The oxide samples used in the present study were high-purity single crystals. The BeO sample used was a high-purity single crystal grown by V.A. Maslov using a modified solution-melt method under reverse temperature drop conditions [130] and the MgO sample was a high-purity single crystal with a 110 orientation commercially acquired from Alfa Aesar. Muon spin rotation experiments were performed in the HAL9500 of the Laboratory for Muon Spectroscopy at the Paul-Scherrer Institut (Villigen, Switzerland). Positive muons with nearly 100% spin-polarization were implanted in the sample at a range of $T = 6$ K to $T = 300$ K. An external magnetic field was applied perpendicular to the initial muon spin polarization. Samples were mounted on the sample holders in order for the applied transverse field to be in MgO perpendicular to the -100 direction and in BeO parallel to the 001 direction.

As mentioned already, we will focus on the study of the atom like interstitial configurations in these earth alkaline metals.

Fast-Fourier transforms (FFT) of the μSR spectra obtained at fields ranging from $B = 1$ T to $B = 8$ T are shown in Fig. 4.16. The FFT spectra clearly show the presence of three lines corresponding to oscillations of the detected muon spin polarization. The lowest frequency corresponds to the expected Larmor frequency of the muon subject to a diamagnetic environment, $\nu_{dia} = \gamma_\mu B$, where $\gamma_\mu = 135.53$ MHz/T is the gyromagnetic ratio of

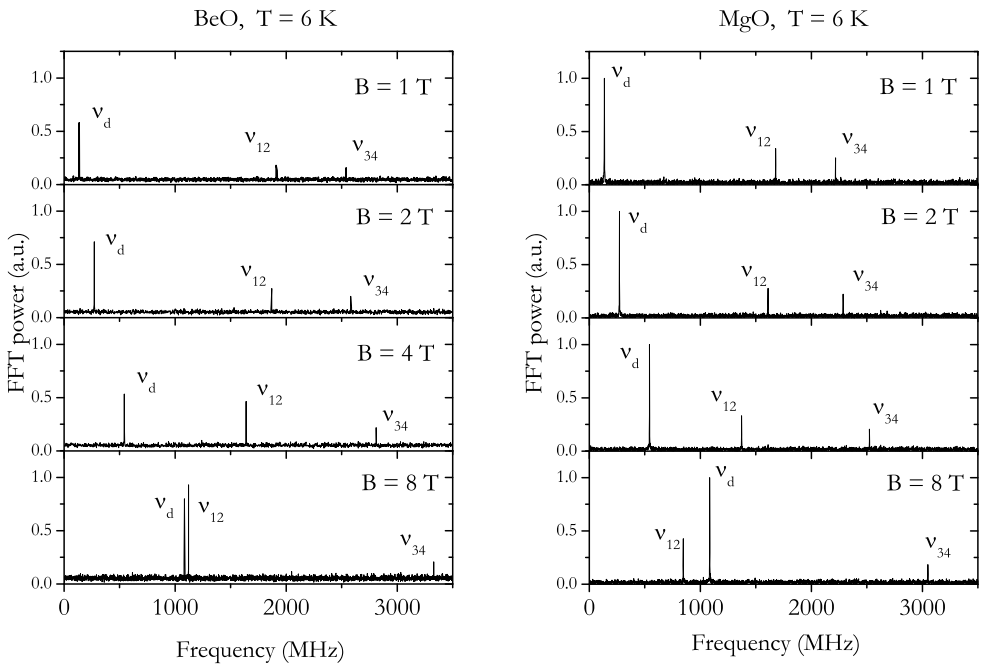

Figure 4.16: *Fast-Fourier transforms (FFT) of the μSR spectra, for BeO (left) and MgO (right), obtained at fields ranging from $B = 1$ T to $B = 8$ T, at $T = 6$ K. Three lines are clearly visible: ν_d corresponds to a diamagnetic state; ν_{12} and ν_{34} correspond to a muonium state with a vacuum-like hyperfine interaction, as discussed in the text.*

the muon. The two frequencies observed at higher frequencies correspond to muons in a paramagnetic environment and, as we will detail below, correspond to the ν_{12} and ν_{34} transitions of a muonium state with a vacuum-like hyperfine interaction. The unbalance of the ν_{12} and ν_{34} lines observed in Fig. 4.16 is an instrumental effect due to the frequency-dependent detector efficiency.

The time spectra were therefore analysed using a sum of damped oscillations of the form:

$$A(t) = A_{\rm dia} e^{-\lambda_{\rm dia} t} \cos\left(2\pi\nu_{\rm dia} t + \phi_{\rm dia}\right) + A_{12} e^{-\lambda_{12} t} \cos\left(2\pi\nu_{12} t + \phi_{12}\right) + A_{34} e^{-\lambda_{34} t} \cos\left(2\pi\nu_{34} t + \phi_{34}\right)$$

At 1 T the relaxation λ_{dia}, is basically constant with applied field at about 0.16 μs^{-1} for BeO and 0.06 μs^{-1} for MgO. These relaxation λ_{dia} are likely due to nuclear dipolar broadening. λ_{12} and λ_{34} are found to be 0.3 μs^{-1} both for MgO and BeO. The asymmetry parameters A_{dia}, A_{12} and A_{34} are highly frequency-dependent at these applied high fields, but with the help of a Ag calibration we observe that the sum of the muonium fractions $f_{12} + f_{34}$ are constant (at about 60% for BeO and at about 30% for MgO).

We note that a significant percentage of the muon spin polarization is not observed at this temperature and field (about 7% for BeO and about 30% for MgO) , corresponding either to a third configuration and/or to the presence of dynamical processes associated to the muon thermalization. The fitted frequencies ν_{12} and ν_{34} are plotted in Fig. 4.17 and consistently behave as the hyperfine transitions of an isotropic muonium state with a vacuum-like hyperfine parameter. According to this model we expect (Table 1.3):

$$\nu_{12} = \left| \frac{A_{iso}}{2} + \nu_- - \frac{\nu_+}{\beta} \right|$$
$$\nu_{34} = \left| \frac{A_{iso}}{2} - \nu_- + \frac{\nu_+}{\beta} \right|$$

where $A_{\rm iso}$ is the hyperfine parameter, $\nu_\pm = (\gamma_e \pm \gamma_\mu)B/2$, (with $\gamma_e = 28024.21$ MHz/T and $\gamma_\mu = 135.53$ MHz/T), and $\beta = \sqrt{1 + (A_{iso}/2\nu_+)^2}$. The lines in Fig. 4.17 are a global fit to this model with the hyperfine parameter $A_{\rm iso}$ as the single fitting parameter. The fit yields $A_{\rm iso}$(Mu) = 4451.2(2) MHz for BeO and $A_{\rm iso}$(Mu) = 3895.9(8) MHz for MgO. This value for MgO is very close to the one obtained by Kiefl et al. (3849.2(8) MHz at 300 K) [109].

We have also determinated the temperature dependence of the hyperfine interactions. The decrease in the hyperfine interactions with temperature is

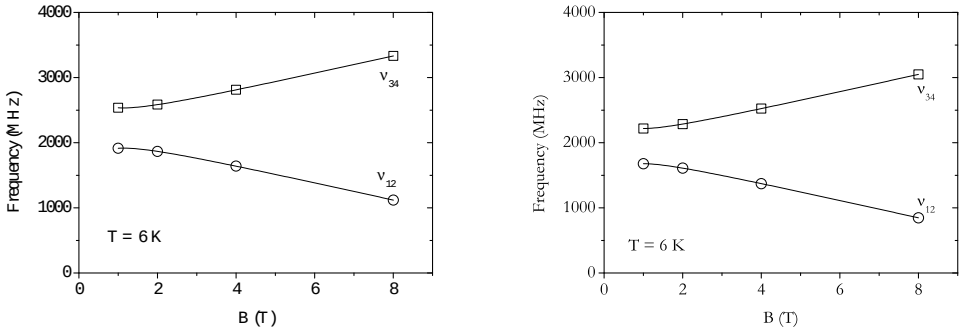

Figure 4.17: *Frequencies ν_{12} and ν_{34} as a function of applied transverse magnetic field, as obtained from the fits to the time spectra. The lines are a global fit to an isotropic muonium state with the hyperfine parameter $A_{\rm iso}$ as the single fitting parameter, resulting in $A_{\rm iso} = 4451.2(2)$ MHz for BeO (left) and $A_{\rm iso} = 3895.9(8)$ MHz for MgO (right).*

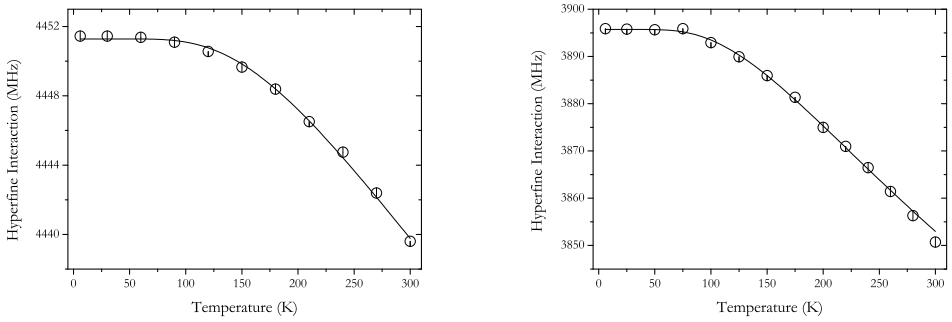

Figure 4.18: *Temperature dependence of BeO (left) and MgO (right) of the hyperfine interaction of the atom-like muonium configuration. The solid line is a fit using an Einstein model.*

again associated to local vibrational modes and fitted to Einstein model used for Lu_2O_3 (equation 4.4). The fits to this model are shown in figure 4.18 As for Lu_2O_3, we observed that only the first two terms of equation 4.4 were needed to fit the data. This is once again a sign that the corresponding vibrations are very small. The parameters obtained in the fit were $C_1 = -91(7)$ MHz, $A_0 = 4451,3(1)$ MHz and $E_a = 54(2)$ meV for BeO and $C_1 = -187(9)$ MHz, $A_0 = 3895.7(2)$ MHz and $E_a = 40(9)$ meV for MgO.

Chapter 5

Conclusions and future perspectives

We now summarize the main results of this dissertation and present some pathways for the future, based on the present investigation. In the present work, novel aspects have been unveiled related to the two basic isolated hydrogen/muonium configurations: the oxygen-bound donor-like configuration and the interstitial acceptor like configuration, as well as related to the respective interconversion and interplay. In a technical aspect related to the μSR technique, we have also obtained new results related to the elusive muonium formation processes.

5.1 Oxygen-bound configuration

The main result arising from this investigation is the firm establishment of a polaron-like configuration for the oxygen-bound state in TiO_2 and ZrO_2, where the electron brought by the muon in the implantation is trapped in a cation close to the muon final site. The resulting hyperfine interaction is extremely reduced and essentially with a dipolar character, making it extremely difficult to detect directly. This was possible in monocrystalline rutile TiO_2, but not in polycrystalline ZrO_2, where the hyperfine interaction leads to a broadening of the diamagnetic line. The polaron state in ZrO_2 was nevertheless clearly established from the analogy with TiO_2 and from

the first-principles calculations in ZrO_2 running parallel to this work.

5.2 Interstitial atom-like configuration and the energy barrier to the oxygen-bound configuration

An atom-like configuration has also been characterized in this work. In ZrO_2 and HfO_2 this identification has been indirect, but clear spectroscopic signals were characterized for the first time in Lu_2O_3 and BeO. The conversion of this configuration to the oxygen-bound configuration was observed in ZrO_2 and interpreted, with the help of the minimum-energy paths (MEPs) calculations, in terms of a model where at the end of the thermalization process of the muon needs a certain amount of energy to surpass a barrier from one local minimum energy configuration to another. This is likely to occur in other systems both investigated in this work or described in the literature that were interpreted in terms of hole capture or ionization but whose conversion energy may not correspond adequately to these types of process [11].

5.3 Muonium formation and the role of lattice vibrations

A particularly important result obtained in this work is related to the fact the μSR is an implantation technique where the muon has an initial kinetic energy of 4 MeV. This means that metastable states may be assessed and may be sufficiently long-lived to impact on the μSR signal. In HfO_2 and ZrO_2, we propose a metastable neutral interstitial configuration, whose conversion to the stable interstitial configuration is hindered by the lattice at low temperatures and occurs only when lattice vibrations are available.

5.4 Future perspectives

From the vast amount of data gathered in the oxide systems addressed in this work, two important topics have been left out of this dissertation although they have been object of intense work in its final stages. These topics relate to the nature of the fast relaxing component observed in ZrO_2 and to the temperature dependence of the muonium configurations in Lu_2O_3, BeO and MgO. The first constitutes a natural devellopment of the muonium formation problem, whereas the second extends the study now presented to these other technologically relevant systems.

5.4.1 Fast component in ZrO_2

As mentioned in section 3.3, a fast relaxing component was observed in several ZrO_2 samples. This was apparently diamagnetic. Longitudinal field μSR data reveals however that this fast relaxing component peaks at low fields: the complementary non-relaxing component is represented in Fig. 5.1 and is strongly suggestive of the repolarization pattern of a paramagnetic muonium state with a small hyperfine interaction. This means that this short-lived relaxing component is actually paramagnetic. We have not followed this important question within this dissertation, but it has been object of posterior work [131].

5.4.2 Building a complete model for the isolated hydrogen configurations in Lu_2O_3, BeO and MgO

As mentioned in Chapter 4, we followed the temperature dependence at high-fields of the μSR signals in Lu_2O_3, BeO and MgO. Beyond the characterization of the atom-like configuration presented in Chapter 4, these data have extremely rich information about the oxygen-bound configuration in these systems, as well as about the interconversion between these basic configurations. The analysis and modelling of the temperature dependence are out of the scope of this dissertation and will benefit from additional experiments and from the modelling here presented for ZrO_2.

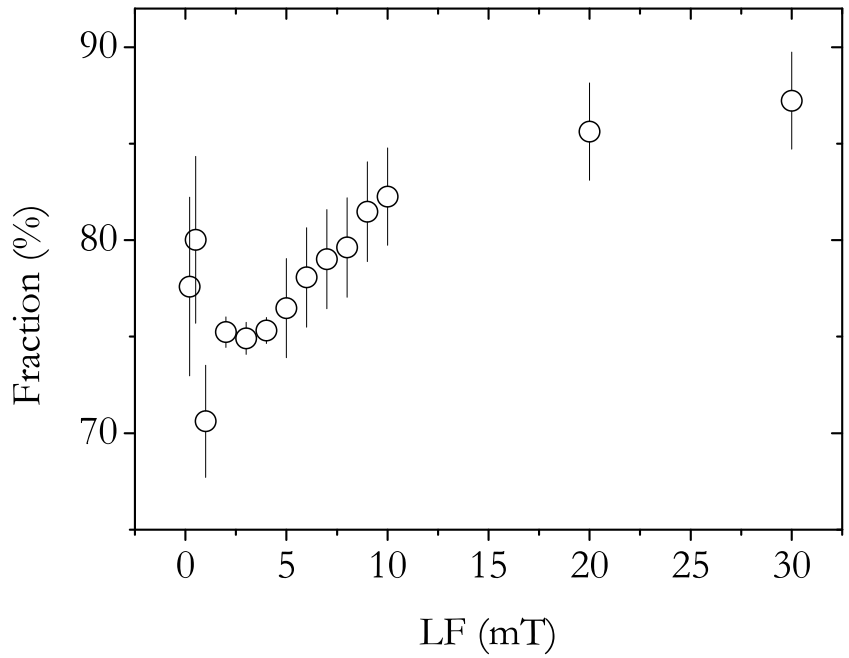

Figure 5.1: *Decoupling curve in longitudinal magnetic field of MgSZ at 8 K.*

In BeO the experimental determination of the muon stopping site is possible in principle. In fact, Be has 100% spin 3/2 and a high magnetic moment ($-1.1779\ \mu_N$). An angular dependence of the relaxation rate of the diamagnetic component was attempted at PSI (Fig. 5.2) and this relaxation rate was found to be independent of the angular position. This is a signal that the diamagnetic configuration is possibly at an anti-bonding site [19]. The theoretical calculations have the bond-type configuration as the lowest energy oxygen bond configuration and the antibonding configuration as a higher (possibly metastable) configuration. To clarify this point, avoided level crossing resonance (ALC) measurements were proposed and approved at ISIS (and scheduled to October 2017).

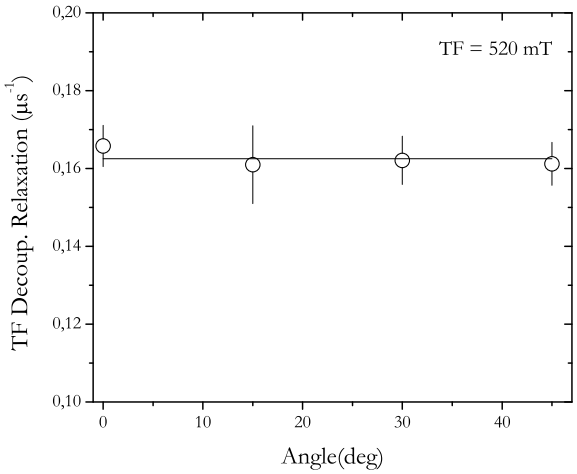

Figure 5.2: *BeO angular dependence of the relaxation rate. The line is a constant function fit yielding* $\lambda = 0.163(1)\mu s$

.

Bibliography

[1] Magdalena Momirlan and T.N. Veziroglu. The properties of hydrogen as fuel tomorrow in sustainable energy system for a cleaner planet. *International Journal of Hydrogen Energy*, 30(7):795 – 802, 2005.

[2] Shuji Nakamura, Naruhito Iwasa, Masayuki Senoh, and Takashi Mukai. Hole compensation mechanism of p-type gan films. *Japanese Journal of Applied Physics*, 31(5R):1258, 1992.

[3] Jörg Neugebauer and Chris G. Van de Walle. Hydrogen in gan: Novel aspects of a common impurity. *Phys. Rev. Lett.*, 75:4452, Dec 1995.

[4] M. T. Bohr, R. S. Chau, T. Ghani, and K. Mistry. The high-k solution. *IEEE Spectrum*, 44(10):29–35, Oct 2007.

[5] J.L. Lyons, A. Janotti, and C.G. Van de Walle. The role of oxygen-related defects and hydrogen impurities in HfO2 and ZrO2. *Microelectronic Engineering*, 88(7):1452–1456, jul 2011.

[6] Sangtae Kim, Hugo J Avila-Paredes, Shizhong Wang, Chien-Ting Chen, Roger A De Souza, Manfred Martin, and Zuhair A Munir. On the conduction pathway for protons in nanocrystalline yttria-stabilized zirconia. *Physical chemistry chemical physics : PCCP*, 11(17):3035–8, may 2009.

[7] Michael Stavola, Figen Bekisli, Weikai Yin, Kirby Smithe, W. Beall Fowler, and Lynn A. Boatner. Contrasting the experimental properties of hydrogen in SnO_2, In_2O_3, and TiO_2. *Journal of Applied Physics*, 115(1):012001, 2014.

[8] A. T. Brant, Shan Yang, N. C. Giles, and L. E. Halliburton. Hydrogen donors and Ti^{3+} ions in reduced TiO_2 crystals. *Journal of Applied Physics*, 110(5):053714, 2011.

[9] Takahira Miyagi, Masayuki Kamei, Takefumi Mitsuhashi, and Atsushi Yamazaki. Discovery of the deep level related to hydrogen in anatase tio2. *Applied Physics Letters*, 88(13):132101, 2006.

[10] E. Mamontov, L. Vlcek, D. J. Wesolowski, P. T. Cummings, W. Wang, L. M. Anovitz, J. Rosenqvist, C. M. Brown, and V. Garcia Sakai. Dynamics and structure of hydration water on rutile and cassiterite nanopowders studied by quasielastic neutron scattering and molecular dynamics simulations. *The Journal of Physical Chemistry C*, 111(11):4328–4341, 2007.

[11] S. F. J. Cox, J. L. Gavartin, J. S. Lord, S. P. Cottrell, J. M. Gil, H. V. Alberto, J. Piroto Duarte, R. C. Vilão, N. Ayres de Campos, D. J. Keeble, E. A. Davis, M. Charlton, and D. P. van der Werf. Oxide muonics: II. modelling the electrical activity of hydrogen in wide-gap and high-permittivity dielectrics. *Journal of Physics: Condensed Matter*, 18(3):1079, 2006.

[12] R. C. Vilão, A. G. Marinopoulos, R. B. L. Vieira, A. Weidinger, H. V. Alberto, J. Piroto Duarte, J. M. Gil, J. S. Lord, and S. F. J. Cox. Hydrogen Impurity in Paratellurite α-TeO_2: Muon-Spin Rotation and Ab Initio Studies. *Physical Review B*, 84(4):045201, July 2011.

[13] R. C. Vilão, R. B. L. Vieira, H. V. Alberto, J. M. Gil, A. Weidinger, R. L. Lichti, B. B. Baker, P. W. Mengyan, and J. S. Lord. Muonium donor in rutile TiO_2 and comparison with hydrogen. *Physical Review B*, 92(8):081202, 2015.

[14] R. B. L. Vieira, R. C. Vilão, A. G. Marinopoulos, P. M. Gordo, J. A. Paixão, H. V. Alberto, J. M. Gil, A. Weidinger, R. L. Lichti, B. Baker, P. W. Mengyan, and J. S. Lord. Isolated hydrogen configurations in zirconia as seen by muon spin spectroscopy and ab initio calculations. *Physical Review B*, 94(11):115207, sep 2016.

[15] A. G. Marinopoulos. Incorporation and migration of hydrogen in yttria-stabilized cubic zirconia: Insights from semilocal and hybrid-functional calculations. *Physical Review B - Condensed Matter and Materials Physics*, 86, 2012.

[16] E. L. Silva, A. G. Marinopoulos, R. C. Vilão, R. B. L. Vieira, H. V. Alberto, J. Piroto Duarte, and J. M. Gil. Hydrogen impurity in yttria: Ab initio and μSR perspectives. *Physical Review B*, 85(16):165211, apr 2012.

[17] A G Marinopoulos. First-principles study of hydrogen configurations at the core of a high-angle grain boundary in cubic yttria-stabilized zirconia. *Journal of physics. Condensed matter : an Institute of Physics journal*, 26(2):025502, jan 2014.

[18] E. Lora da Silva, A. G. Marinopoulos, R. B. L. Vieira, R. C. Vilão, H. V. Alberto, J. M. Gil, R. L. Lichti, P. W. Mengyan, and B. B. Baker. Electronic structure of interstitial hydrogen in lutetium oxide from DFT + U calculations and comparison study with μ SR spectroscopy. *Physical Review B*, 94(1):014104, jul 2016.

[19] R. C. Vilão. *Isolated Hydrogen in II-VI Zinc-chalcogenide widegap semiconductors modelled by the muon analogue*. PhD thesis, Faculdade de Ciências e Tecnologia - Universidade de Coimbra, 2007.

[20] W. A. MacFarlane. βNMR and μSR as local magnetic probes of condensed mater. MPI-UBC, Stuttgat Quantum Materials "Summer" School, October 2010.

[21] A Schenck. *Muon Spin Rotation Spectroscopy: Principles and Applications in Solid State Physics*. Adam Hilger Ltd, Bristol, 1985.

[22] S. G. Karshenboim. Constraints on a long-range spin-dependent interaction from precision atomic physics. *Phys. Rev. D*, 82(11):113013, Dec 2010.

[23] Randolf Pohl, Aldo Antognini, François Nez, Fernando D. Amaro, François Biraben, João M. R. Cardoso, Daniel S. Covita, Andreas

Dax, Satish Dhawan, Luis M. P. Fernandes, Adolf Giesen, Thomas Graf, Theodor W. Hänsch, Paul Indelicato, Lucile Julien, Cheng-Yang Kao, Paul Knowles, Eric-Olivier Le Bigot, Yi-Wei Liu, José A. M. Lopes, Livia Ludhova, Cristina M. B. Monteiro, Françoise Mulhauser, Tobias Nebel, Paul Rabinowitz, Joaquim M. F. dos Santos, Lukas A. Schaller, Karsten Schuhmann, Catherine Schwob, David Taqqu, João F. C. A. Veloso, and Franz Kottmann. The size of the proton. *Nature*, 466(7303):213–216, July 2010.

[24] David Tucker-Smith and Itay Yavin. Muonic hydrogen and mev forces. *Phys. Rev. D*, 83(10):101702, May 2011.

[25] J. M. Bailey, W. E. Cleland, V. W. Hughes, R. Prepost, and K. Ziock. Muonium. ii. observation of the muonium hyperfine-structure interval. *Phys. Rev. A*, 3(3):871–884, Mar 1971.

[26] W. Liu, M. G. Boshier, S. Dhawan, O. van Dyck, P. Egan, X. Fei, M. Grosse Perdekamp, V. W. Hughes, M. Janousch, K. Jungmann, D. Kawall, F. G. Mariam, C. Pillai, R. Prigl, G. zu Putlitz, I. Reinhard, W. Schwarz, P. A. Thompson, and K. A. Woodle. High precision measurements of the ground state hyperfine structure interval of muonium and of the muon magnetic moment. *Phys. Rev. Lett.*, 82(4):711–714, Jan 1999.

[27] C. J. Joachain B. H. Bransden. *Physics of Atoms and Molecules*. Prentice Hall, Harlow, 2nd edition edition, 2003.

[28] Bruce D. Patterson. Muonium states in semiconductors. *Rev. Mod. Phys.*, 60(1):69, Jan 1988.

[29] R. B. L. Vieira. Hydrogen impurity in paratellurite α-TeO_2 using muon-spin rotation. Master's thesis, Faculdade de Ciências e Tecnologia - Universidade de Coimbra, 2011.

[30] J. M. Gil, H. V. Alberto, R. C. Vilão, J. Piroto Duarte, P. J. Mendes, L. P. Ferreira, N. Ayres de Campos, A. Weidinger, J. Krauser, Ch. Niedermayer, and S. F. J. Cox. Novel Muonium State in CdS. *Physical Review Letters*, 83(25):5294–5297, dec 1999.

[31] J. Gil, H. Alberto, R. Vilão, J. Piroto Duarte, N. Ayres de Campos, A. Weidinger, J. Krauser, E. Davis, S. Cottrell, and S. Cox. Shallow donor muonium states in II-VI semiconductor compounds. *Physical Review B*, 64(7):075205, jul 2001.

[32] Chris G. Van de Walle. Hydrogen as a Cause of Doping in Zinc Oxide. *Physical Review Letters*, 85(5):1012–1015, jul 2000.

[33] S. F. J. Cox, E. A. Davis, S. P. Cottrell, P. J. C. King, J. S. Lord, J. M. Gil, H. V. Alberto, R. C. Vilão, J. Piroto Duarte, N. Ayres de Campos, A. Weidinger, R. L. Lichti, and S. J. C. Irvine. Experimental Confirmation of the Predicted Shallow Donor Hydrogen State in Zinc Oxide. *Physical Review Letters*, 86(12):2601–2604, mar 2001.

[34] R. Lichti, K. Chow, and S. Cox. Hydrogen Defect-Level Pinning in Semiconductors: The Muonium Equivalent. *Physical Review Letters*, 101(13):136403, sep 2008.

[35] R.L. Lichti, K.H. Chow, J.M. Gil, D.L. Stripe, R.C. Vilão, and S.F.J. Cox. Location of the H level: Experimental limits for muonium. *Physica B: Condensed Matter*, 376-377:587–590, apr 2006.

[36] Carlos Fiolhais, Fernando Nogueira, and Miguel A.L. Marques. *A Primer in Density Functional Theory (Lecture Notes in Physics) (v. 620)*. Springer, 2003.

[37] B. Hitti, S. R. Kreitzman, T. L. Estle, E. S. Bates, M. R. Dawdy, T. L. Head, and R. L. Lichti. Dynamics of negative muonium in n-type silicon. *Phys. Rev. B*, 59(7):4918–4924, Feb 1999.

[38] P. W. Anderson. Model for the electronic structure of amorphous semiconductors. *Phys. Rev. Lett.*, 34(15):953–955, Apr 1975.

[39] Johann-Martin Spaeth and Harald Overhof. *Point Defects in Semiconductors and Insulators: Determination of Atomic and Electronic Structure from Paramagnetic Hyperfine Interactions*. Springer Berlin Heidelberg, Berlin, Heidelberg, 2003.

[40] Krisztián Szász, Tamás Hornos, Martijn Marsman, and Adam Gali. Hyperfine Coupling of Point Defects in Semiconductors by Hybrid Density Functional Calculations: The Role of Core Spin Polarization. *Physical Review B*, 88:075202, Aug 2013.

[41] VASPwiki. http://cms.mpi.univie.ac.at/wiki/.

[42] O. V. Yazyev, I. Tavernelli, L. Helm, and U. Röthlisberger. Core Spin-Polarization Correction in Pseudopotential-Based Electronic Structure Calculations. *Physical Review B*, 71:115110, Mar 2005.

[43] Ulrike Diebold. The surface science of titanium dioxide. *Surface Science Reports*, 48(5-8):53–229, January 2003.

[44] Xiaobo Chen and Samuel S Mao. Titanium dioxide nanomaterials: synthesis, properties, modifications, and applications. *Chemical reviews*, 107(7):2891–959, July 2007.

[45] John Robertson. High dielectric constant gate oxides for metal oxide Si transistors. *Reports on Progress in Physics*, 69(2):327–396, feb 2006.

[46] P F Chester and D H Bradhurst. Electrolytically Induced Conductivity in Rutile. *Nature*, 199(4898):1056–1057, September 1963.

[47] G J Hill. The effect of hydrogen on the electrical properties of rutile. *Journal of Physics D: Applied Physics*, 1(9):1151–1162, September 1968.

[48] Skjalg Erdal, Camilla Kongshaug, Tor S. Bjø rheim, Niina Jalarvo, Reidar Haugsrud, and Truls Norby. Hydration of Rutile TiO 2 : Thermodynamics and Effects on n - and p -Type Electronic Conduction. *The Journal of Physical Chemistry C*, 114(19):9139–9145, May 2010.

[49] E. J. Spahr, L. Wen, M. Stavola, L. A. Boatner, L. C. Feldman, N. H. Tolk, and G. Lüpke. Giant Enhancement of Hydrogen Transport in Rutile TiO_{2} at Low Temperatures. *Physical Review Letters*, 104(20):205901, May 2010.

[50] Tor S Bjørheim, Svein Stølen, and Truls Norby. Ab initio studies of hydrogen and acceptor defects in rutile TiO_2. *Physical chemistry chemical physics : PCCP*, 12(25):6817–25, July 2010.

[51] F. Filippone, G. Mattioli, P. Alippi, and A. Amore Bonapasta. Properties of hydrogen and hydrogen–vacancy complexes in the rutile phase of titanium dioxide. *Physical Review B*, 80(24):245203, December 2009.

[52] W. P. Chen, Y. Wang, and H. L. W. Chan. Hydrogen: A metastable donor in TiO[sub 2] single crystals. *Applied Physics Letters*, 92(11):112907, 2008.

[53] Chris G Van de Walle and J Neugebauer. Universal alignment of hydrogen levels in semiconductors, insulators and solutions. *Nature*, 423(6940):626–628, 2003.

[54] H. Li and J. Robertson. Behaviour of hydrogen in wide band gap oxides. *Journal of Applied Physics*, 115(20):203708, May 2014.

[55] Matthew D. McCluskey, Marianne C. Tarun, and Samuel T. Teklemichael. Hydrogen in oxide semiconductors. *Journal of Materials Research*, 27:2190–2198, 2012.

[56] B. R. Carroll, R. L. Lichti, P. W. Mengyan, B. B. Baker, Y. G. Celebi, P. J. C. King, K. H. Chow, and I. Yonenaga. Spectroscopic identification of shallow muonium acceptors in Si0.06Ge0.94. *Applied Physics Letters*, 105:122101, 2014.

[57] Detlev Hofmann, Albrecht Hofstaetter, Frank Leiter, Huijuan Zhou, Frank Henecker, Bruno Meyer, Sergei Orlinskii, Jan Schmidt, and Pavel Baranov. Hydrogen: A Relevant Shallow Donor in Zinc Oxide. *Physical Review Letters*, 88(4):045504, 2002.

[58] A. Weidinger, H. V. Alberto, J. M. Gil, R. C. Vilão, J. Piroto Duarte, and N. Ayres de Campos. Muon and hydrogen states in II-VI semiconductor compounds. A μSR study. *physica status solidi (c)*, (2):711–714, February 2003.

[59] S F J Cox. The shallow-to-deep instability of hydrogen and muonium in II–VI and III–V semiconductors. *Journal of Physics: Condensed Matter*, 15(46):R1727–R1780, 2003.

[60] N.M. Dimitrijevic, Z.V. Saponjic, B.M. Rabatic, O.G. Poluektov, and T. Rajh. Effect of Size and Shape of Nanocrystalline TiO_2 on Photogenerated Charges. An EPR Study. *Journal of Physical Chemistry C*, 111(40):14597–14601, 2007.

[61] Chinthala Praveen Kumar, Neeruganti Obularajugari Gopal, Ting Chung Wang, Ming-Show Wong, and Shyue Chu Ke. EPR investigation of TiO_2 nanoparticles with temperature-dependent properties. *The Journal of Physical Chemistry B*, 110(11):5223–5229, 2006.

[62] Shan Yang, A. T. Brant, N. C. Giles, and L. E. Halliburton. Intrinsic small polarons in rutile TiO_2. *Physical Review B - Condensed Matter and Materials Physics*, 87(12):125201, 2013.

[63] Marina V. Koudriachova, Simon W. de Leeuw, and Nicholas M. Harrison. First-principles study of h intercalation in rutile TiO_2. *Phys. Rev. B*, 70:165421, Oct 2004.

[64] A. T. Brant, N. C. Giles, and L. E. Halliburton. Insertion of lithium ions into TiO_2 (rutile) crystals: An electron paramagnetic resonance study of the Li-associated Ti^{3+} small polaron. *Journal of Applied Physics*, 113, 2013.

[65] F. Herklotz, E. V. Lavrov, and J. Weber. Infrared absorption of the hydrogen donor in rutile TiO_2. *Phys. Rev. B*, 83:235202, 2011.

[66] D. P. Thompson, A. M. Dickins, and J. S. Thorp. The dielectric properties of zirconia. *Journal of Materials Science*, 27(8):2267–2271, 1992.

[67] Neelima Mahato, Amitava Banerjee, Alka Gupta, Shobit Omar, and Kantesh Balani. Progress in material selection for solid oxide fuel cell technology: A review. *Progress in Materials Science*, 72:141–337, jul 2015.

[68] Joong Sun Park, Young Beom Kim, Joon Hyung Shim, Sangkyun Kang, Turgut M. Gür, and Fritz B. Prinz. Evidence of Proton Transport in Atomic Layer Deposited Yttria-Stabilized Zirconia Films. *Chemistry of Materials*, 22(18):5366–5370, sep 2010.

[69] Camille Tandé, Domingo Pérez-Coll, and Glenn C. Mather. Surface proton conductivity of dense nanocrystalline YSZ. *Journal of Materials Chemistry*, 22(22):11208, 2012.

[70] S. Kim, U. Anselmi-Tamburini, H. J. Park, M. Martin, and Z. A. Munir. Unprecedented Room-Temperature Electrical Power Generation Using Nanoscale Fluorite-Structured Oxide Electrolytes. *Advanced Materials*, 20(3):556–559, feb 2008.

[71] Yves A. Mantz and Randall S. Gemmen. Protonated Forms of Monoclinic Zirconia: A Theoretical Study. *The Journal of Physical Chemistry C*, 114(17):8014–8025, may 2010.

[72] P. W. Peacock and J. Robertson. Behavior of hydrogen in high dielectric constant oxide gate insulators. *Applied Physics Letters*, 83(10):2025, 2003.

[73] K. Xiong, J. Robertson, and S. J. Clark. Behavior of hydrogen in wide band gap oxides. *Journal of Applied Physics*, 102(8):083710, 2007.

[74] Mostafa Youssef and Bilge Yildiz. Hydrogen defects in tetragonal ZrO_2 studied using density functional theory. *Phys. Chem. Chem. Phys.*, 16(4):1354–1365, 2014.

[75] Xinyuan Zhao and David Vanderbilt. Phonons and lattice dielectric properties of zirconia. *Physical Review B*, 65(7):1–10, jan 2002.

[76] A. X. S. Bruker. *TOPAS V4: General Profile and Structure Analysis Software for Powder Diffraction Data, User's Manual.* Karlsruhe, Germany, 2008.

[77] F. L Pratt. WIMDA: a muon data analysis program for the Windows PC. *Physica B: Condensed Matter*, 289-290:710–714, 2000.

[78] R C Vilão. Estudo das interacções do hidrogénio com defeitos estruturais em semicondutores do tipo calcopirite utilizando técnicas de muões. Master's thesis, Faculdade de Ciências e Tecnologia - Universidade de Coimbra, 2002.

[79] V Corregidor, D. Martín y Marero, J. M Gil, and E Diéguez. Dependence of the hydrogen spin dynamics on the conductivity type in CdTe as evidenced by its muonium analogue. *Europhysics Letters (EPL)*, 67(2):247–253, jul 2004.

[80] E. A. Davis, S. F. J. Cox, R. L. Lichti, and C. G. Van de Walle. Shallow donor state of hydrogen in indium nitride. *Applied Physics Letters*, 82(4):592, 2003.

[81] H. V. Alberto, R. C. Vilão, J. Piroto Duarte, J. M. Gil, N. Ayres de Campos, R. L. Lichti, E. A. Davis, S. P. Cottrell, and S. F. J. Cox. Powder Pattern Hyperfine Spectroscopy of Shallow- Donor Muonium Centres. *Hyperfine Interactions*, 136/137:471–477, 2001.

[82] J. Piroto Duarte. *Study of hydrogen in phthalocyanine semiconductors using μSR technique.* Phd thesis in physics, University of Coimbra, 2006.

[83] N. R. Lomb. Least-squares frequency analysis of unequally spaced data. *Astrophysics and Space Science*, 39(2):447–462, feb 1976.

[84] C.B. Azzoni and A. Paleari. EPR study of electron trays in x-ray-irradiated yttria-stabilized zirconia. *Physical Review B*, 40:6518, 1989.

[85] V. M. Orera, R. I. Merino, Y. Chen, R. Cases, and P. J. Alonso. Intrinsic electron and hole defects in stabilized zirconia single crystals. *Physical Review B*, 42(16):9782–9789, dec 1990.

[86] C Azzoni. Paramagnetic-defect kinetics in yttria-stabilized zirconia. *Solid State Ionics*, 44(3-4):267–273, feb 1991.

[87] Figen Bekisli, W. Beall Fowler, and Michael Stavola. Small polaron characteristics of an OD center in TiO_2 studied by infrared spectroscopy. *Physical Review B*, 86(15):155208, oct 2012.

[88] C Azzoni and A Paleari. Annihilation of paramagnetic centers in yttria-stabilized zirconia. *Solid State Ionics*, 46(3-4):259–263, jul 1991.

[89] James A. Dawson, Hungru Chen, and Isao Tanaka. Protonic defects in yttria stabilized zirconia: incorporation, trapping and migration. *Physical Chemistry Chemical Physics*, 16(10):4814, 2014.

[90] R B L Vieira, R C Vilão, P M Gordo, a G Marinopoulos, H V Alberto, J. Piroto Duarte, J M Gil, A Weidinger, and J S Lord. Muon-Spin-Rotation study of yttria-stabilized zirconia (ZrO_2:Y): Evidence for muon and electron separate traps. *Journal of Physics: Conference Series*, 551:012050, 2014.

[91] H. V. Alberto, A. Weidinger, R. C. Vilão, J. Piroto Duarte, J. M. Gil, J. S. Lord, and S. F. J. Cox. Mechanisms of electron polarization of shallow muonium in CdTe and CdS. *Physical Review B*, 81(24):245205, jun 2010.

[92] H. V. Alberto, R. C. Vilão, J. Piroto Duarte, J. M. Gil, A. Weidinger, J. S. Lord, and S. F. J. Cox. Electron Polarization and Formation Probability of Bound Muonium in CdS and Si. *Physical Review B*, 86:035203, Jul 2012.

[93] Jean-Marc Costantini and François Beuneu. Point defects induced in yttria-stabilized zirconia by electron and swift heavy ion irradiations. *Journal of Physics: Condensed Matter*, 23(11):115902, 2011.

[94] R B L Vieira, R C Vilão, H V Alberto, J M Gil, A Weidinger, B B Baker, P W Mengyan, and R L Lichti. High-field study of muonium states in HfO_2 and ZrO_2. *Journal of Physics: Conference Series*, 551:012048, 2014.

[95] B. Eisenstein, R. Prepost, and A. M. Sachs. Depolarization of Positive Muons in Solids. *Physical Review*, 142(1):217–227, feb 1966.

[96] F. L. Pratt. Repolarization of anisotropic muonium in orientationally disordered solids. *Philosophical Magazine Letters*, 75(6):371–380, jun 1997.

[97] A. J. Houtepen, J .M. Gil, J. S. Lord, P. Liljeroth, D. Vanmaekelbergh, H. V. Alberto, R. C. Vilão, J. Piroto Duarte, N. Ayres de Campos, J. L. Gavartin, and S. F. J. Cox. Muonium in nano-crystalline II–VI semiconductors. *Physica B: Condensed Matter*, 404(5-7):837–840, apr 2009.

[98] Gustavo M. Dalpian and James R. Chelikowsky. Self-Purification in Semiconductor Nanocrystals. *Physical Review Letters*, 96(22):226802, jun 2006.

[99] T.-L. Chan, Murilo L. Tiago, Efthimios Kaxiras, and James R. Chelikowsky. Size Limits on Doping Phosphorus into Silicon Nanocrystals. *Nano Letters*, 8(2):596–600, feb 2008.

[100] R. C. Vilão, H. V. Alberto, J. Piroto Duarte, J. M. Gil, A. Weidinger, N. Ayres de Campos, R. L. Lichti, K. H. Chow, and S. F. J. Cox. Muonium Spectroscopy in ZnSe: Metastability and Conversion. *Physical Review B*, 72:235203, Dec 2005.

[101] Rui Wu, Bo Zhou, Qian Li, ZhenYi Jiang, WenBo Wang, WenYan Ma, and XiaoDong Zhang. Elastic and vibrational properties of monoclinic hfo 2 from first-principles study. *Journal of Physics D: Applied Physics*, 45(12):125304, 2012.

[102] Giuseppe Fadda, Giovanni Zanzotto, and Luciano Colombo. First-principles study of the effect of pressure on the five zirconia polymorphs. i. structural, vibrational, and thermoelastic properties. *Phys. Rev. B*, 82:064105, Aug 2010.

[103] R. C. Vilão, J. M. Gil, A. Weidinger, H. V. Alberto, J. Piroto Duarte, N. Ayres de Campos, R. L. Lichti, K. H. Chow, S. P. Cottrell, and S. F. J. Cox. Acceptor Level of Interstitial Muonium in ZnSe and ZnS. *Physical Review B*, 77:235212, Jun 2008.

[104] J. M. Gil, P. J. Mendes, L. P. Ferreira, H. V. Alberto, R. C. Vilão, N. Ayres de Campos, A. Weidinger, Y. Tomm, Ch. Niedermayer, M. V. Yakushev, R. D. Tomlinson, S. P. Cottrell, and S. F. J. Cox. Modeling

hydrogen in $CuInSe_2$ and $CuInS_2$ solar cell materials using implanted muons. *Phys. Rev. B*, 59:1912–1916, Jan 1999.

[105] R.C. Vilão, J.M. Gil, H.V. Alberto, J.Piroto Duarte, N.Ayres de Campos, A. Weidinger, M.V. Yakushev, and S.F.J. Cox. Muon diffusion and trapping in chalcopyrite semiconductors. *Physica B: Condensed Matter*, 326(1–4):181 – 184, 2003.

[106] Jakub Čížek, Oksana Melikhova, Ivan Procházka, Jan Kuriplach, Radomír Kužel, Gerhard Brauer, Wolfgang Anwand, Tatyana E. Konstantinova, and Igor A. Danilenko. Defect studies of nanocrystalline zirconia powders and sintered ceramics. *Phys. Rev. B*, 81:024116, Jan 2010.

[107] O. J. Dura, R. Boada, M. A. López de la Torre, G. Aquilanti, A. Rivera-Calzada, C. Leon, and J. Chaboy. Xanes and exafs study of the local order in nanocrystalline yttria-stabilized zirconia. *Phys. Rev. B*, 87:174109, May 2013.

[108] R. Hempelmann, M. Soetratmo, O. Hartmann, and R. Wäppling. Muon diffusion and trapping in proton conducting oxides. *Solid State Ionics*, 107(3–4):269 – 280, 1998.

[109] R. F. Kiefl, W. Odermatt, Hp. Baumeler, J. Felber, H. Keller, W. Kündig, P. F. Meier, B. D. Patterson, J. W. Schneider, K. W. Blazey, T. L. Estle, and C. Schwab. Muonium centers in the cuprous halides. *Phys. Rev. B*, 34:1474, 1986.

[110] Akio Ikesue and Yan Lin Aung. Ceramic laser materials. *Nat Photon*, 2(12):721–727, 12 2008.

[111] U. Griebner, V. Petrov, K. Petermann, and V. Peters. Passively mode-locked yb:lu2o3 laser. *Opt. Express*, 12(14):3125–3130, Jul 2004.

[112] E Zych, D Hreniak, W Strek, L Kepinski, and K Domagala. Sintering properties of urea-derived lu2o3-based phosphors. *Journal of Alloys and Compounds*, 341(1–2):391 – 394, 2002. Proceedings of the 5th International Conference on Excited States of Transition Elements.

[113] G. Scarel, E. Bonera, C. Wiemer, G. Tallarida, S. Spiga, M. Fanciulli, I. L. Fedushkin, H. Schumann, Yu. Lebedinskii, and A. Zenkevich. Atomic-layer deposition of lu2o3. *Applied Physics Letters*, 85(4):630–632, 2004.

[114] Malgorzata Guzik, Jan Pejchal, Akira Yoshikawa, Akihiko Ito, Takashi Goto, Milosz Siczek, Tadeusz Lis, and Georges Boulon. Structural investigations of lu2o3 as single crystal and polycrystalline transparent ceramic. *Crystal Growth & Design*, 14(7):3327, 2014.

[115] Justyna Zeler, Lucjan B. Jerzykiewicz, and Eugeniusz Zych. Flux-aided synthesis of lu2o3 and lu2o3:eu—single crystal structure, morphology control and radioluminescence efficiency. *Materials*, 7(10):7059, 2014.

[116] L. Ning, Y. Zhang, and Z. Cui. Structural and Electronic Properties of Lutecia from First Principles. *Journal of Physics: Condensed Matter*, 21:455601, 2009.

[117] Koichi Momma and Fujio Izumi. *VESTA3* for three-dimensional visualization of crystal, volumetric and morphology data. *Journal of Applied Crystallography*, 44(6):1272, 2011.

[118] P. W. Peacock and J. Robertson. Band Offsets and Schottky Barrier Heights of High Dielectric Constant Oxides. *Journal of Applied Physics*, 92:4712, 2002.

[119] R. Alvero, A. Bernal, I. Carrizosa, J. A. Odriozola, and J. M. Trillo. Lanthanide Oxides: Lu_2O_3 Hydration. *Journal of the Less Common Metals*, 110(1–2):425, 1985.

[120] J. M. Flitcroft, M. Molinari, N. A. Brincat, M. T. Storrb, and S. C. Parker. Hydride Ion Formation in Stoichiometric UO_2. *Chemical Communications*, 51:16209, 2015.

[121] J. H. Yum, T. Akyol, M. Lei, T. Hudnall, G. Bersuker, M. Downer, C. W. Bielawski, J. C. Lee, and S. K. Banerjee. Atomic layer deposited beryllium oxide: Effective passivation layer for iii-v

metal/oxide/semiconductor devices. *Journal of Applied Physics*, 109(6):064101, 2011.

[122] Ming Lei, J. H. Yum, J. Price, Todd W. Hudnall, C. W. Bielawski, S. K. Banerjee, P. S. Lysaght, G. Bersuker, and M. C. Downer. Spectroscopic evaluation of band alignment of atomic layer deposited beo on si(100). *Applied Physics Letters*, 100(12):122906, 2012.

[123] H. S. Craft, R. Collazo, M. D. Losego, Z. Sitar, and J.-P. Maria. Surface water reactivity of polycrystalline mgo and cao films investigated using x-ray photoelectron spectroscopy. *Journal of Vacuum Science & Technology A: Vacuum, Surfaces, and Films*, 26(6):1507–1510, 2008.

[124] Derek W. Johnson, Jung Hwan Yum, Todd W. Hudnall, Ryan M. Mushinski, Christopher W. Bielawski, John C. Roberts, Wei-E Wang, Sanjay K. Banerjee, and H. Rusty Harris. Characterization of ald beryllium oxide as a potential high-k gate dielectric for low-leakage algan/gan moshemts. *Journal of Electronic Materials*, 43(1):151–154, 2014.

[125] André O. Menezes, Michelly T. Rodrigues, Adriana Zimmaro, Luiz E.P. Borges, and Marco A. Fraga. Production of renewable hydrogen from aqueous-phase reforming of glycerol over pt catalysts supported on different oxides. *Renewable Energy*, 36(2):595 – 599, 2011.

[126] B. T. Jeffries, R. Gonzalez, Y. Chen, and G. P. Summers. Luminescence in thermochemically reduced mgo: The role of hydrogen. *Phys. Rev. B*, 25:2077–2080, Feb 1982.

[127] M. Kodu, M. Aints, T. Avarmaa, V. Denks, E. Feldbach, R. Jaaniso, M. Kirm, A. Maaroos, and J. Raud. Hydrogen doping of mgo thin films prepared by pulsed laser deposition. *Applied Surface Science*, 257(12):5328–5331, 4 2011.

[128] M. S. Khalil, M. J. A. Stoutimore, S. Gladchenko, A. M. Holder, C. B. Musgrave, A. C. Kozen, G. Rubloff, Y. Q. Liu, R. G. Gordon, J. H. Yum, S. K. Banerjee, C. J. Lobb, and K. D. Osborn. Evidence for

hydrogen two-level systems in atomic layer deposition oxides. *Applied Physics Letters*, 103(16):162601, 2013.

[129] A. G. Marinopoulos, R. C. Vilão, R. B. L. Vieira, H. V. Alberto, J. M. Gil, M. V. Yakushev, R. Scheuermann, and T. Goko. Defect levels and hyperfine constants of hydrogen in beryllium oxide from hybrid-functional calculations and muonium spectroscopy. *Philosophical Magazine*, 97(24):2108, 2017.

[130] V. A. Maslov, G. M. Bylov, B. G. Mazurenko, A. V. Kruzhalov, and Shulgin B. V. *Proc. 6th Int. Conference on Crystal Growth*, 3:268–269, 1980.

[131] R. C. Vilão, R. B. L. Vieira, H. V. Alberto, J. M. Gil, and A. Weidinger. The role of the transition state in muon implantation. *Physical Review B*, Submited, 2017.